Automatic Detection of High Frequency Oscillations of Neural Signals in Epileptic Patients

Roshanak Yazdanpour-Naeini

A Thesis
in
The Department
of
Electrical and Computer Engineering

Presented in Partial Fulfillment of the Requirements
for the Degree of Master of Applied Science (Electrical Engineering) at
Concordia University
Montreal, Quebec, Canada

November 2012

CONCORDIA UNIVERSITY
School of Graduate Studies

This is to certify that the thesis prepared

By: Roshanak Yazdanpour-Naeini

Entitled: Automatic Detection of High Frequency Oscillations of Neural Signals in Epileptic Patients

and submitted in partial fulfillment of the requirements for the degree of

Master of Applied Science

Signed by the final Examining Committee:

__________________________ Chair
Dr. C. Wang
__________________________ Examiner
Dr. T. Fancott
__________________________ Examiner
Dr. M. O.Ahmad
__________________________ Thesis Supervisor
Dr. M. N. S. Swamy
__________________________ Thesis Supervisor
Dr. R. Agarwal

Approved by ____

____________ 2012 ________________________________

Abstract

Epilepsy is one the most common neurological disorders. For patients suffering from epilepsy who are medically intractable, in certain cases surgical resection of pathologic brain tissue is one remaining possibility. Prior to surgery, intracranial Electroencephalography (IEEG) study is conducted to localize seizure-generating zones. IEEG typically consists of studying epileptiform spikes and seizure discharges; however some researchers have observed short bursts of high frequency oscillations (HFOs), mostly in the range of 100-500 Hz in the seizure generating areas. A retrospective correlation analysis between the post-surgical outcome and HFO generating tissue supports the idea that HFO events may play a fundamental role in epilepsy and epileptogenesis. Recently, HFO events have been scored visually by clinicians. Typically, it is necessary to record IEEG for several days or weeks to collect sufficient epileptiform activities for precise evaluation. Needless to say, manual review of the data makes visual scoring an extremely tiresome process in which subjectivity is inevitable. Due to the recent explosion of HFO research, the development of algorithms for automatic detection of HFO events poses a great benefit to researchers and clinicians. In the literature, two methods have been widely used for automatic detection of HFO events based on the energy of the signal in the 100-500 Hz frequency band. In this thesis, we present three new methods for automatic detection of HFO events based on the sharpness property of the IEEG signals. By using simulated and real-data signals, the performance of the proposed methods are compared to the existing energy-based approaches using sensitivity and specificity metrics. Additionally, we present the clinical implication of the HFO event detections for four epileptic patients. The results indicate that the performance of the proposed detectors are robust and stable and do not deteriorate in the presence of the noise and artifacts.

Acknowledgments

I would like to sincerely thank both of my supervisors, Dr. M. N. Swamy and Dr. Rajeev Agarwal for providing continuous support, encouragement, and supervision while accomplishing this work.

Special gratitude goes to Dr. Swamy for giving me the opportunity to attend graduate studies as well as for his generous assistance both academically and financially. I am very grateful for his tireless support and patience throughout my research.

I would like to express my deepest appreciation to Dr. Rajeev Agarwal for kindling my interest in my area of research and sharing his vast knowledge and experience with me during past two years. Without his support, this work would have not been completed.

Last but not least, I am grateful to all my family, friends, and colleagues whose invaluable moral support and companionship helped me greatly in accomplishing this task.

Roshanak Yazdanpour-Naeini

I dedicate this thesis to my lovely parents who have always believed in me and given me their full unconditional and constant help.

Table of Contents

List of Figures

List of Tables

List of Acronyms

AD	Anterior Depth
AP	Action Potential
AR	Auto-Regressive
AT	Anterior Temporal
AWGN	Additive White Gaussian Noise
BG	Background Signal
BPF	Band-Pass Filter
CNS	Central Nervous System
CT	Computed Tomography
dB	Decibel
DG	Dentate Gyrus
EC	Entorhinal Cortex
ECDF	Empirical Cumulative Density Function
ECG	Electrocardiography
ECoG	Electrocorticography
EEG	Electroencephalography
EEGer	Electroencephalographer
EMG	Electromyography
EOG	Electro-Occulography
EPSP	Excitatory Post-Synaptic Potential
EZ	Epileptic Zone
FIR	Finite Impulse Response
FN	False Negative
FP	False Positive

FP	Frontal/Parietal
FR	Fast Ripple
HEI	High Energy Interference
HFO	High Frequency Oscillation
Hip	Hippocampus
HPF	High-Pass Filter
HW	Half-Wave
IED	Interictal Epileptiform Discharge
IEEG	Intracranial Electroencephalography
IFSECN	International Federation of Societies for Electroencephalography and Clinical Neurophysiology
IPSP	Inhibitory Post-Synaptic Potential
LAD	Left Anterior Depth Electrode
LMD	Left Mesial Depth
LPD	Left Posterior Depth
MNI	Montreal Neurological Institute
MRI	Magnetic Resonance Imaging
MT	Mesial Temporal
MTLE	Mesial Temporal Lobe Epilepsy
NE	Neocortical Epilepsy
NN	Neural Network
NREM	Non Rapid Eye Movement
PD	Posterior Depth
PET	Positron Emission Tomography
PSD	Power Spectral Density
PSO	Particle Swarm Optimization
PT	Posterior Temporal

RAD	Right Anterior Depth Electrode
REM	Rapid Eye Movement
RMS	Root Mean Square
ROC	Receiver Operating Characteristic
RPD	Right Posterior Depth
RPT	Right Posterior Temporal
SEEG	Stereotactic Electroencephalography
SF	Sub Frontal
SHW	Sharpness of Half-Wave
SN	Sensitivity
SNR	Signal to Noise ratio
SOZ	Seizure Onset Zone
SP	Specificity
SPECT	Single-Photon Emission Computed Tomography
SSZ	Seizure Spread Zone
STFT	Short-Time Fourier Transform
STLL	Short-Time Line Length
TLE	Temporal Lobe Epilepsy
TO	Temporal Occipital
TP	True Positive
WE	Wavelet Entropy

Chapter 1 . Introduction

A remarkable breakthrough in understanding the physiology of the brain appeared when techniques were developed to record its electrical activities. Traditionally, most clinical systems for the acquisition of the brain's electrical activity, known as electroencephalograms, have been designed to record signals from surface of the scalp. Such a recording is referred to as electroencephalography (EEG). EEG has been used for many purposes such as early diagnosis and localization of brain tumors, coma assessment in intensive care units, study of sleep stages, and most importantly, diagnosis of epilepsy.

Epilepsy is one the most common neurological disorders. The primary therapy recommended for epilepsy is antiepileptic drugs. However, thirty to forty percent of patients with focal epilepsy are medically intractable. For these patients, surgical removal of epileptogenic areas is the most promising treatment [1]. However, result of the surgery depends upon accurate identification of epileptic brain tissues and benefits of this treatment apply to those patients in whom the seizures are well localized. Various approaches including characteristics of initial behavioural ictal events, scalp EEG, structural imaging studies (MRI, X-CT, SPECT or PET), and interictal epileptiform discharges (spikes, sharp waves) are used for locating epileptic zone (EZ is defined as the minimum amount of cortex that needs to be resected [2]).

In many patients, the epileptiform activity may be located in areas of the brain that may be not accessible via conventional scalp EEG recording. In such cases, intracranial electrodes are used for long-term EEG recording in order to locate seizure onset zone (SOZ is defined as the area from which clinical seizures start at the time of pre-surgical evaluation [2]) and assess various characteristics of epilepsy.

It has been 10 years since EEG activity above 70 Hz attracted specific attention. The first research on high frequency oscillations (≥ 100 Hz) was carried out in 1992 [3]. Soon after, wide-band EEG recording (≥ 1000 Hz) was used by many researchers in patients suffering from different kinds of epilepsies. High frequency oscillations have been classified into two bands: ripples (100-250 Hz) and fast ripples (250-500 Hz). Correlation between fast ripples and regions of seizure initiation supports the idea that fast ripples may reflect pathological hypersynchronous events that could be related to seizure genesis. In addition, both types of HFOs have been discovered in the dentate gyrus of kianic acid-treated epileptic rats [4]; while they are not found in that structure of normal brain. Therefore it is hypothesized that HFOs could be biomarkers for epileptogenecity. Researches have shown that HFOs seem to be a more reliable indicator of the SOZ than epileptic spikes [5-7]. Moreover, they can also indicate epileptogenic areas outside the SOZ. Identifying such high frequency oscillations (HFOs), either visually or automatically, could help researchers to study details about these events and their relation to seizure generation.

Recently, various methods have been developed for HFO detection. A summary of those studies are presented in 0. In this thesis we will implement two of the existing methods from the literature, modify one of these detectors in two versions, and introduce three new methods for HFO detection.

In the remainder of this chapter, some basic principal about electroencephalography, seizures and high frequency oscillation that we will refer to throughout the thesis are described.

1.1 Basic Principles

Detailed description of the brain is far beyond the scope of this thesis, but we will provide here an overview of some of the basic anatomical and physiological facts about the brain and will present the most essential terms that have been used throughout this work to facilitate the presentation of the material in the following chapters.

1.1.1 Brain structures

From the anatomical point of view, central nervous system (CNS) is composed of the brain and the spinal cord. The brain itself has multiple subdivisions and is composed of the cerebrum, the cerebellum, and the brainstem. The cerebrum is divided into two halves: left and right hemisphere. Each cerebral hemisphere consists of several lobes: frontal lobe, occipital lobe, parietal lobe, temporal lobe, and limbic lobe (see Figure 1.1A). Excluding limbic lobe, these lobes can be said to contain the motor areas, visual areas, somatosensory areas, auditory areas [8].

Neocortex is the top thin layer of the cerebral hemispheres (not indicated in Figure 1.1) which is involved in various functions such as sensory perception, generation of motor commands, spatial reasoning, and conscious thought. Structure of the limbic system such as olfactory cortex, amygdala, and hippocampus are located within the temporal lobe (See Figure 1.1B).

Temporal lobe plays an important role in organizing sensory input, auditory perception, language production as well as memory formation [9]. The main interface between hippocampus and neocortex is called entorhinal cortex (EC). It is located in the mesial temporal lobe (inner regions of temporal lobe) and functions in a widespread network for memory and navigation.

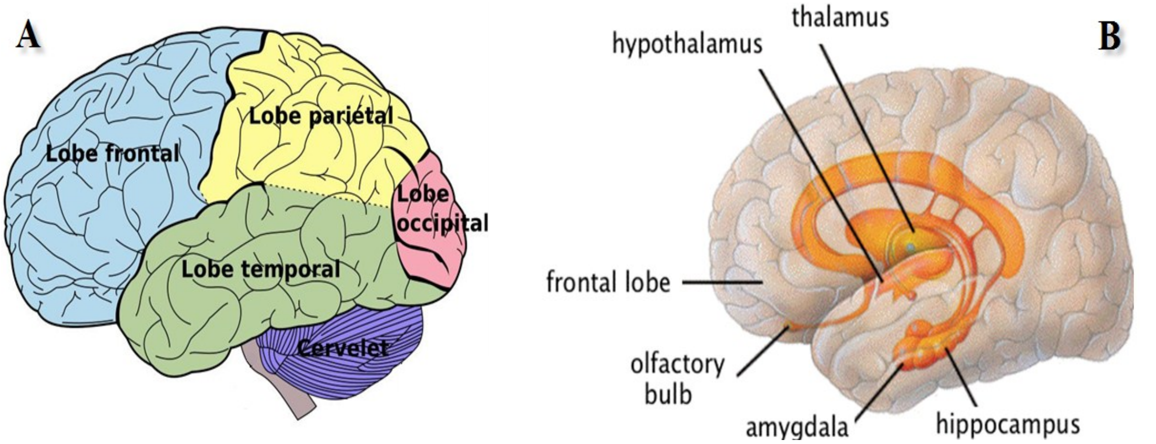

Figure 1.1 Brain anatomy. (A) Outside of brain viewed from the side show the major lobes. (B) Limbic system.
References:http://gleesonpsych.pbworks.com/w/page/7540417/Introduction%20to%20Brain%20and%20Behaviour#TheLimbicSystem, http://webspace.ship.edu/cgboer/limb

1.1.2 Neural activities

Neurons or nerve cells are the basic processing units in the neurophysiological system that process and transmit information by electrical and chemical signaling. Although there are many types of neurons with respect to shape, size and physiological properties, their basic structure can be discussed generally.

A Neuron is basically made of a soma (cell body), several dendrites that receive information and one axon (long cylinder) that sends information through other neurons. The sending neurons contact the receiving neuron via a junction known as synapses. The activities in the central nervous system are mainly related to synaptic currents transferred between synapses. Figure 1.2 illustrates a schematic of the structure of neurons.

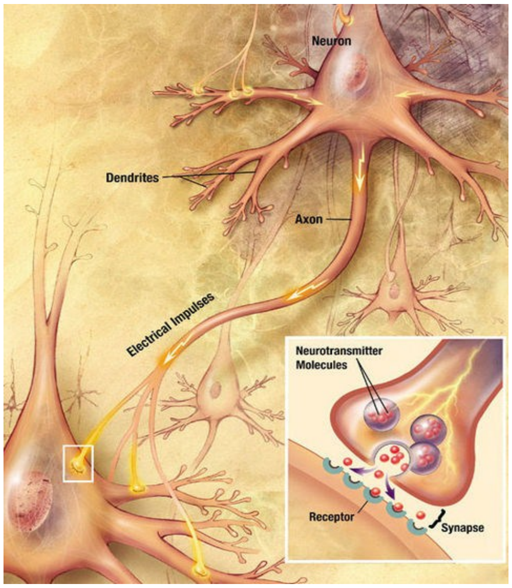

Figure 1.2 Neurons and synapses, Reference:http://en.wikipedia.org/wiki/File:Chemical_synapse_schema_cropped.jpg

The information transmitted by a nerve is called action potential (AP). AP is a temporary change in the membrane potential that is transmitted along the axon and it is caused by exchange of ions (Na^+,K^+,Ca^{++},Cl^-) across neuron membrane. If action potential (AP) is traveling along a fiber which ends at excitatory synapses, then the excitatory post synaptic potential (EPSP) will be passed on to the following neuron. In contrast, if action potential travels towards the inhibitory synapse, then hyper-polarization occurs which indicates the inhibitory post synaptic potential (IPSP).

APs are triggered by various types of stimuli such as chemical, light, electricity, pressure, touch and stretching. Figure 1.3 demonstrates all the steps in generating action potential. The generation of action potential can be divided into four stages. In the first stage, when a dendrite receives the stimulus the Na^+ channels open, if interior potential of the cell increases from -70 mV to -55 mV, the membrane potential depolarizes and generates a rising edge to approximately +30 mV. Later in the second stage (falling edge), the Na^+ channels close and K^+ channels open and the membrane begins to repolarize back to its rest potential. The repolarization typically undershoots the rest potential to a level of approximately -90 mV. It is called hyper-polarization and would seem to be counterproductive, but it is important in the transmission of data. During hyper-polarization, the neuron cannot receive another stimulus. In the final stage, Na^+ and K^+ channels close and bring the membrane back to its resting state of -70 mV. The action potential in most nerves lasts from 5 to 10 milliseconds [10].

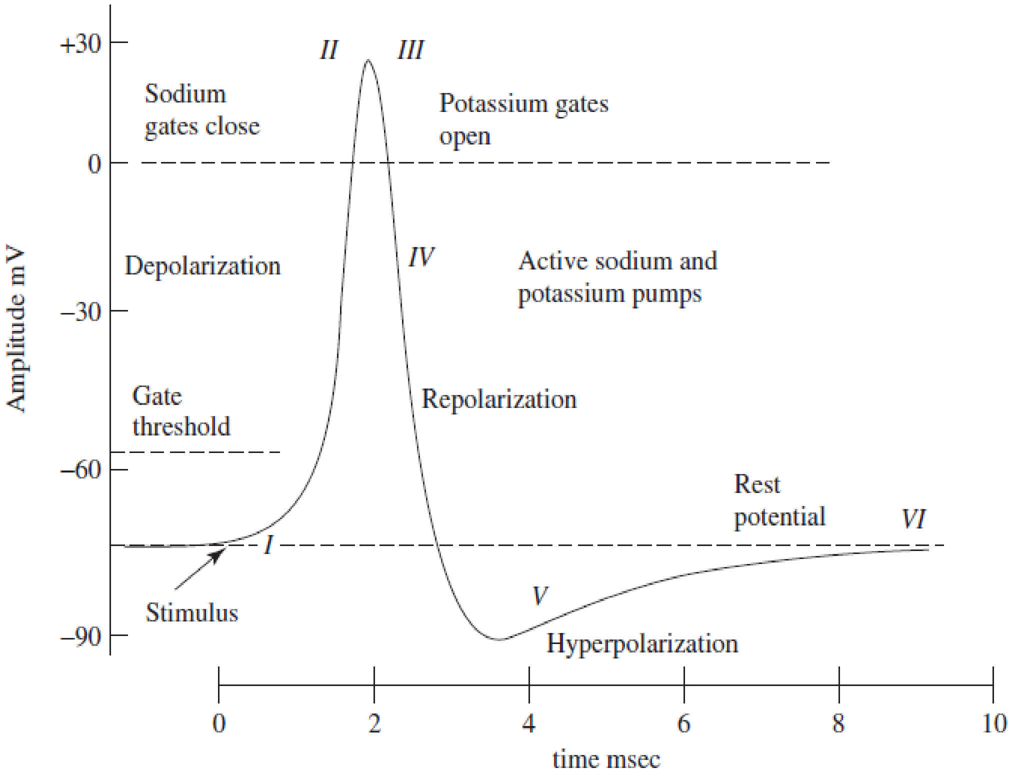

Figure 1.3 An action potential. A transient change in the voltage across the cell membrane, Reference: [10]

1.2 EEG History

Using a galvanometer, electrical signals from muscle nerves were first measured by Carlo Matteucci and Emil Du Bois-Raymond, establishing the concept of neurophysiology [11]. Richard Caton, a physician, published reports on his detection of electrical activity in animal brains [12]. In 1875 he was probably the first to use the galvanometer over the human scalp to record brain activity in the form of electrical signals. Since then, the concept of electro-(electrical activity) encephalo-(signals emitting from the head) and gram or graphy (drawing or writing) combined together established the *"electroencephalogram"* which was henceforth used to denote the neuronal electrical activity of brain. In 1912, Russian physiologist, Vladimir Vladimirovich Prevdich-Neminkey published the first EEG and evoked potentials of mammals (dog) [13]. In 1914, Napoleon Cybulski and Jelenska-Macieszyna photographed EEG–recordings of experimentally induced seizures [14].

German physiologist and psychiatrist, *Hans Berger* began his studies of human EEG in 1920. Hans Berger's discovery that the brain generates a low-level subaudio-frequency electrical activity has led to the establishment of a neurophysiological speciality known as electroencephalography. It was between 1926 and 1929 when Berger first obtained good recording of the alpha waves (8-13 Hz) [15-17]. He also introduced beta activity (14 – 26 Hz). In 1964, W.Grey Walter, British scientist discovered delta waves (0.1 - 3.5 Hz), and theta activity (4 -7.5 Hz) which initiated enormous clinical interest in the diagnosis of brain abnormalities [18].

The importance of multi-channel recordings and using multiple electrodes to cover a wider brain region was recognized by Kornmüller [19]. The first EEG work focusing on epilepsy manifestation and the first demonstration of epileptic spikes were presented by Fischer and Löwenbach [11].

The history of EEG however has been a continuous process, which started in the early 1300s and has brought daily development of clinical, experimental and computational studies for discovery, recognition, diagnosis and treatment of a vast number of neurological disorders. In the modern era, EEGs are recorded invasively as well as noninvasively using fully computerized systems. Throughout the 1950s the work on EEGs expanded in various areas including automatic analysis. However, EEG, by its nature, is too complex to be fully interpreted automatically [10, 11].

1.3 Electroencephalography (EEG)

Brain is made of billions of brain cells called neurons, which use electricity to communicate with each other. Changing electrical currents across the neuron membrane generates electric and magnetic fields that can be recorded from the surface of the scalp. The potentials between different electrodes located on the scalp are then amplified and recorded as the electroencephalogram (EEG) which is used in the detection of various abnormalities in the brain.

EEG amplitude is typically described as peak to peak voltage. The EEG signal originating in the cerebral cortex has to cross different layers including pia mater, CSF, duramater, bone, galea and scalp before it is recorded by surface scalp electrode. The amplitude of scalp EEG is therefore markedly attenuated and ranges between 10 and 100 μV [10, 20].

EEG is routinely used to assess patients with neurological disorders such as headaches, behavioural disturbances, attention disorders, learning problems, language delay, developmental delay, and fainting spells. But the most common application of EEG is for epilepsy evaluation.

EEG signals can be obtained either invasively from inside the brain (intracranial) or non-invasively from specific locations over the scalp using multiple electrode EEG machines. In some cases such as epileptic studies, scalp EEG doesn't provide sufficient information to locate where seizures originate. Invasive intracranial EEG (IEEG) can be helpful for such cases.

1.4 Intracranial EEG (IEEG)

Most common methods to record IEEG are the stereotactic-EEG (SEEG) and electrocorticography (ECoG) in which depth electrodes and subdural grid electrodes are used to record the EEG directly from the brain. These techniques are used when seizure activity cannot be localized by non-invasive methods and when functional cortical mapping is required during pre-surgical evaluation. The electrodes are surgically implanted and left in place to record EEG for several days to weeks, depending on the time required to collect sufficient epileptiform activity for adequate evaluation. Intracranial EEG recording techniques are more sensitive for the detection of epileptogenic activity because of their greater proximity to the epileptogenic zone and because of their intracranial locations which reduces the electrical resistance between the source and recording electrodes [21]. EEG recorded from inside the brain possesses higher amplitude than that of scalp EEG and ranges between 500 and 1500 μV [20].

1.5 Electrode Positions

A committee of International Federation of Societies for Electroencephalography and

Clinical Neurophysiology (IFSECN) recommended a specific system of scalp electrode placement for use in all laboratories which is now known as International 10-20 system. It was first introduced by Jasper [22]. In this system each electrode is located at standardized location on the head. As can be seen in Figure 1.4, this system is based on the measurements from four standard points on the head: the nasion (intersection of the frontal nasal bones), the inion (the most prominent point at the back of the head) and the left and right of pre-auricular points. Each electrode is labeled with a letter and a number. The letter refers to the area of brain underlying the electrodes (ex. F: Frontal lobe, T: Temporal lobe, C: Central lobe, P: Parietal lobe, O: Occipital lobe), odd numbers refer to left side of brain while even numbers denote to right side of brain. Electrode with letter "A" is usually placed on the ear which is often used as the reference electrode.

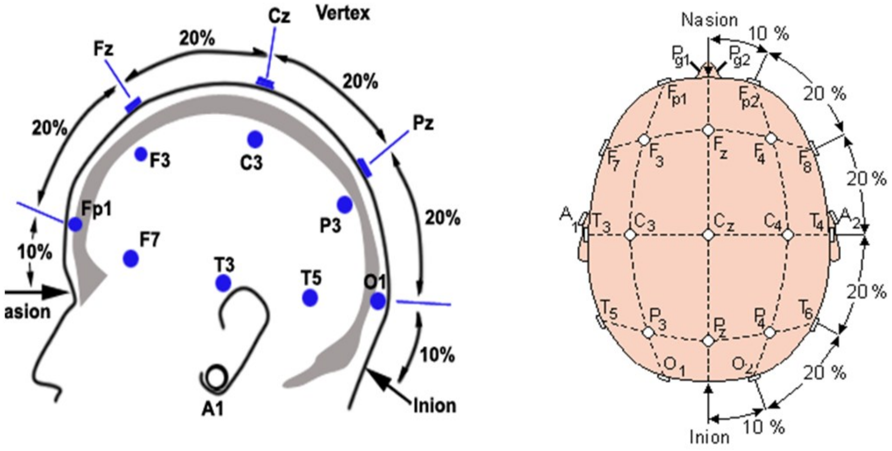

Figure 1.4 Scalp electrodes located in the international 10-20 system.

The potential difference between two electrodes is referred to as channel in EEG. These channels can be arranged in various patterns. A collection of channels in specific configurations is called a montage. Usually for long term duration of EEG recording, multiple montages are used by reconfiguring electrode differences in the software. The two most common montage types used in recording EEG are called referential and bipolar.

In the referential montage, all the electrodes over the scalp use one common reference electrode which is usually one or both of the earlobes. Reference electrode is placed to minimize the possibility of picking up potentials from the brain. In bipolar montage each channel represents a difference between a pair of electrodes. Specifically, the bipolar montage links serial pairs of electrodes in straight longitudinal (front to back) or coronal lines (left to right). In bipolar montage, the possibility of contaminated reference is eliminated as it is common to both electrodes in the pair [20].

Figure 1.5 illustrates an example of EEG montage to show how scalp electrodes are connected to amplifiers in both reference and bipolar montage.

1.6 EEG Electrode Types

Various types of electrodes are used to record EEG activity. The choice of the electrodes depends on the purpose of recording and the location of the recording site (on the scalp or within the brain). EEG electrodes can be placed on the brain either invasively or non-invasively. Non-invasive electrodes are placed on the scalp without surgery while invasive electrodes must be implanted by drilling holes in the skull or craniotomy operation.

1.7 Scalp Electrodes

The scalp electrodes can be attached to the skin in various ways. For optimal recording, electrodes should be in proper contact with the skin. Different types of scalp electrodes can be used to record EEG from the scalp. They are generally comprised of a lead (for conduction of electrical current), a metal electrode, and electrode-conducting paste or gel. Disposable electrodes are found in two types: gel-less or pre-gelled. They are the quickest and simplest way to record EEG. Properly affixed electrodes of this type can provide a secure connection for many hours of undisturbed recording.

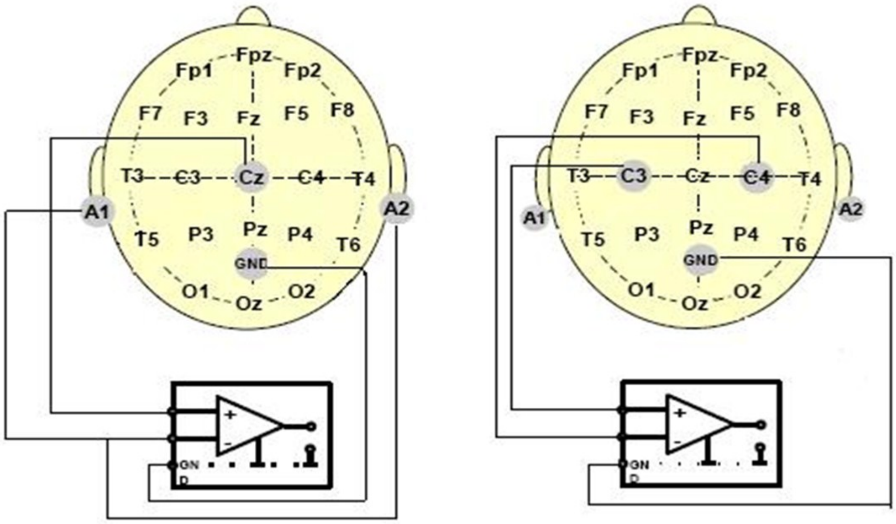

Figure 1.5 EEG Montage Types. Left: Reference montage (C_Z-A_{12}), Right: Bipolar montage (C_3-C_4)

Reusable electrodes made of tin, silver, gold, or stainless steel are placed directly on the scalp, even in a region with hair because they are small (See Figure 1.6,Left). Headbands and electrode caps are used in multichannel recordings with a large number of electrodes, they commonly consist of Ag-AgCl disks, less than 3 mm in diameter, with long flexible leads that are plugged into an amplifier (See Figure 1.6, Middle).

Needle electrodes are another type of electrodes which are implanted under the skull with minimal invasive operations. Needles are available with permanently attached wire leads [10] (See Figure 1.6, Right).

Nasopharyngeal electrode is 10-15 cm long, flexible insulated wire with uninsulated tip (2 mm) that is used for recording inferior temporal or frontal lobe discharges. Sphenoidal electrodes are used to record EEG from anterior tip of the temporal lobe.

Figure 1.6 Scalp Electrodes. Left: reusable single disk electrodes. Middle: Cap electrode, Right: Needle electrodes. References: http://www.emgequipment.com/eeg-electrodes.html, http://www.cbru.helsinki.fi/participation/

1.7.1 Implanted Electrodes (Intracranial Electrodes)

Scalp electrodes, while non-invasive, have significant limitations in the EEG that can be recorded. It appears that EEG activity recorded by scalp electrodes represents only a fraction of the brain activity. The development and use of implanted electrodes started around 1980 and has established its place in epilepsy surgery ever since. Different type of implanted electrodes including subdural, depth, and epidural electrodes are used to record EEG from the brain. These electrodes must be placed by neurosurgeons. They are often used to map or to identify the areas of the brain where seizures start (SOZ). The most common regions of the brain to be studied with intracranial electrodes are temporal and frontal lobes. In chronic epileptic patients, electrodes may remain implanted in the brain for duration of one to three weeks. The number of electrodes implanted depends upon the investigation or treatment being conducted. It is not uncommon to have 40 or more electrodes in the brain tissue. Depending on the type of seizures, its location, and purpose of recording, different electrodes are used for recording prolonged EEG [14].

Subdural electrodes consist of a series of discs fabricated from stainless steel or platinum-iridium embedded in thin transparent silastic that is placed on the surface of the cortex under the dura (Figure 1.7A). Electrode contacts are of different diameters varying between 2 to 5 mm. Subdural electrodes can be grouped in grids and strips. Subdural grids and strips are inserted via craniotomy procedure and are placed on the area of the brain suspected as being pathological or seizure generating. Subdural strips can also be placed through a burr hole located over the convexity of the hemisphere.

Another type of intracranial electrodes are depth electrodes that are made of thin, stainless steel, platinum or gold wire with metal contact points spread out along their length (Figure 1.7B). Depth electrodes are stereotactically implanted and classified into micro and macro electrodes. Unlike subdural grids, depth electrodes are inserted directly into the brain (through burr holes) and they do not require a large opening to be made in the skull. They provide the best recordings of seizures arising from areas deep in the brain.

Epidural electrodes exist as single or double row strips, which are less invasive than subdural grids and can be placed with burr hole (Figure 1.7C). Epidural electrodes are categorized into three groups; epidural screw electrodes, epidural peg electrodes, and epidural strip electrodes. The disadvantage of this type of electrode is its small coverage for recording EEG which may miss the seizure focus [11, 20].

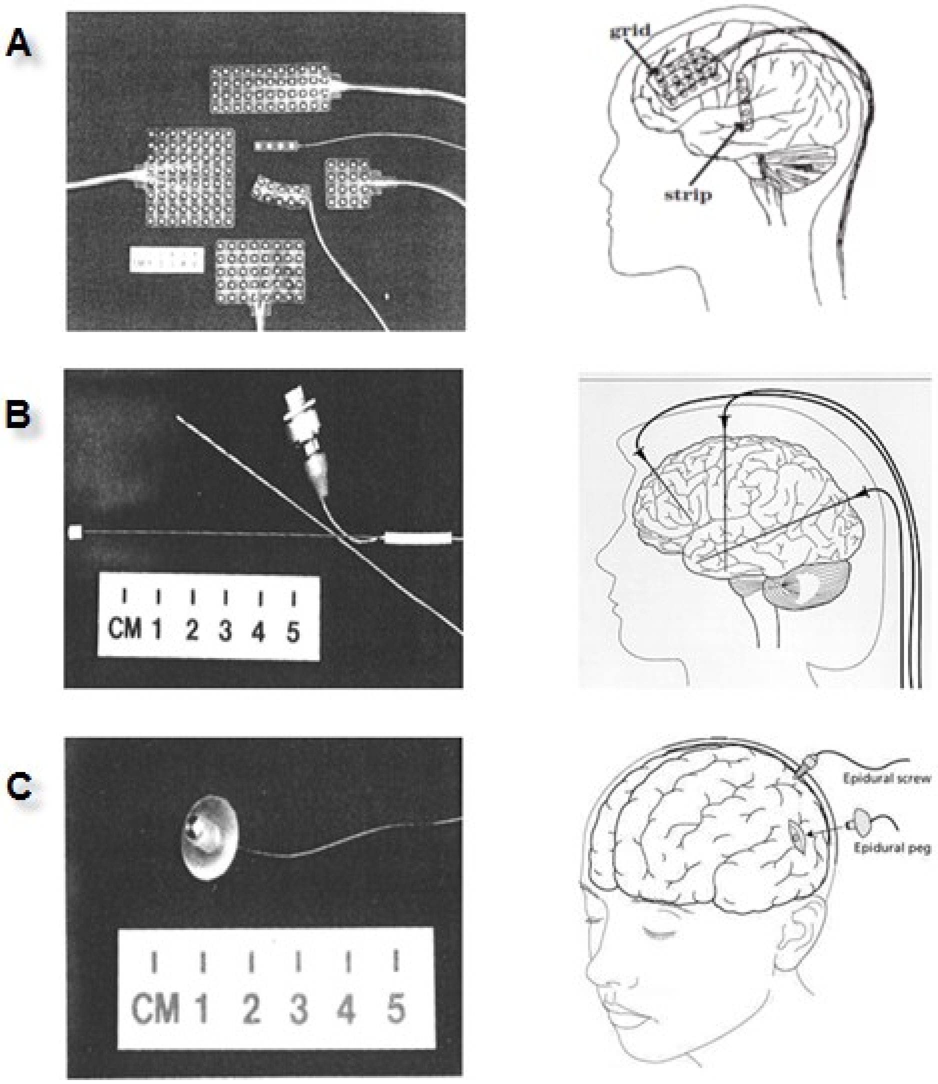

Figure 1.7 Intracranial electrodes. **(A)** Different sizes and shapes of subdural electrodes. **(B)** Depth electrodes. **(C)** Epidural peg electrodes, References: http://smj.sma.org.sg/3302/3302a2.pdf, University of Wisconsin Hospitals and Clinics Authority

1.8 EEG Rhythms

Electroencephalogram consists of a fairly wide frequency spectrum. The normal EEG waves are influenced by age, state of alertness and many other physiological variables. Although frequency response of clinical EEG mostly concentrates in the frequencies lower than 100 Hz, it can reach much higher frequencies (>5000 Hz) if EEG is recorded with an adequate sampling frequency. Wider frequency spectrum is usually more striking when EEG is recorded from intracranial electrodes.

The frequency range of conventional scalp EEG (recorded at 200 Hz sampling rate) is between 0.1 Hz and 100 Hz and, in a more restricted sense, between 0.3 and 70 Hz. Although, higher frequencies (> 100 Hz) are presented when adequate sampling rates are used, their low amplitude in the presence of noise and artifacts limits their usefulness. Scalp EEG is traditionally classified into five spectral bands (Table 1.1).

Table 1.1 Spectral bands of scalp EEG

	Band name	**Spectral band**
1	Delta(Δ)	0.1 - 3.5 Hz
2	Theta(θ)	4 – 7.5 Hz
3	Alpha(α)	8 – 13 Hz
4	Beta(β)	14 – 30 Hz
5	Gamma(γ)	Above 30 Hz

Delta waves are the slowest in frequency but with the highest amplitude that occur during the deep sleep stages. Theta waves play an important role in infancy and childhood, as well as in states of deep relaxation, stress relief, dreaming and rapid eye movement (REM) sleep stages in adults. They are known to be important for spatial mapping and may provide a binding mechanism that contributes to the formation of memory in general. Alpha brainwaves known as the classical EEG occur with eyes open during wakeful period over the posterior regions of head and represent a state of relaxed mental awareness. Beta rhythm indicates the on-going brain activity encountered mainly over the frontal and central regions which is correlated with a state of alertness and focused concentration; however, large amounts of beta rhythm with high amplitude could be a signature of abnormality. The fastest group of scalp EEG that is a very rare state of brain activity is defined as gamma rhythm. Gamma band is linked to peak concentration and the brain's optimal frequency for cognitive functioning [10, 14, 20].

Spikes and sharp waves are the two most common specific waveforms (characteristic shapes) which are closely related phenomena and both are suggestive of epilepsy (Figure 1.8). According to IFSECN in 1974, spike is defined as *"a transient, clearly distinguished from the background activity, with duration between 20 and 70 ms and variable amplitude"*. In most cases, spikes are different from background due to their high amplitudes; however there are some spikes with amplitudes not distinguishable from background activity. Interictal (period between seizures) spikes are thought to be markers of epileptogenic tissue, but their involvement in seizure generation is still unclear [23]. Sharp waves are similar to spikes, but sharp waves are longer (70-200 ms) in duration. Some sharp waves can exceed the length of 200 ms duration [14, 20]. Both spikes and sharp waves are referred to as interictal epileptiform discharges (IED).

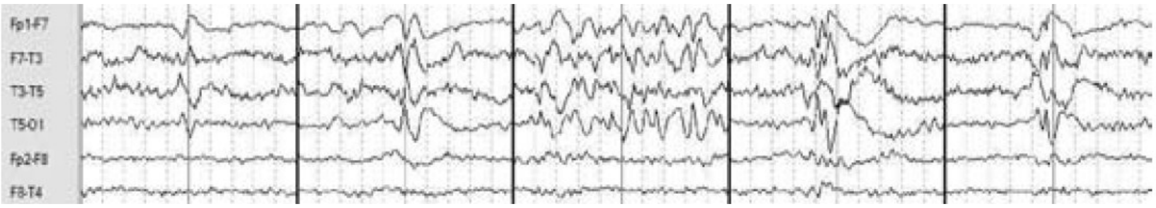

Figure 1.8 Different morphologies include sharpwaves(seen during seconds 1 and 2, spikes and sharp waves (second 3), polyspike-and –slow waves (second 4), and spike-and-wave discharges(in the last second of the figure)

1.9 Epilepsy

The term "epilepsy" is derived from the Greek word ***"epilambanein",*** which means "to seize upon" or "to attack". Epilepsy is not a disease but a "*chronic recurrence of sudden* *abnormal reactions of the brain as epileptic seizures which are caused by large number of brain disorders and facilitated by the presence of a genetic predisposition*” [11]. Epilepsies represent a distinctive group of waveforms that are characteristically different from those in normal EEG (Figure 1.9).

Epilepsy is a neurological condition that makes people more susceptible to having seizures. Depending on the extent of involvement of the various brain regions, epileptic seizures are classified into two main groups; focal seizures, and generalized seizures. Focal seizures, also called partial seizures, occur in a localized area of the brain, while generalized seizures are seen in the whole brain. Electrical stimulation of specific brain regions demonstrated that some epileptic seizures could be classified and named according to anatomical substrates. As an example, temporal lobe epilepsy refers to seizures originating in temporal lobe (the most epileptogenic region of the brain) [1, 3].

Most seizures include rhythmic discharge of large amplitude. The paroxysm includes the increase in the amplitude or increase in the frequency contents of EEG signal. Seizure activity may be rhythmic in the frequency range of 3-29 Hz lasting from several seconds to several minutes.

Spikes and sharp-waves are the most significant biomarkers which clinically are used for epileptic condition; however, recent studies on high frequency oscillations ($\geq$ 100 Hz) have suggested that the HFO events can be a more reliable indicator to the SOZ than epileptic spikes. Nevertheless the research is in infancy and ongoing.

1.10 High Frequency Oscillations (HFOs)

High frequency oscillations are field potentials that reflect short-term synchronization of neural activity and they generally occur during non-rapid eye movement (NREM) state.

HFOs are broadly classified into ripples and fast ripples (FR) and range between 100-250 Hz (see Figure 1.10B) and 250-500 Hz (see Figure 1.10A) respectively. They are believed to play important roles in both the normal and pathological brain.

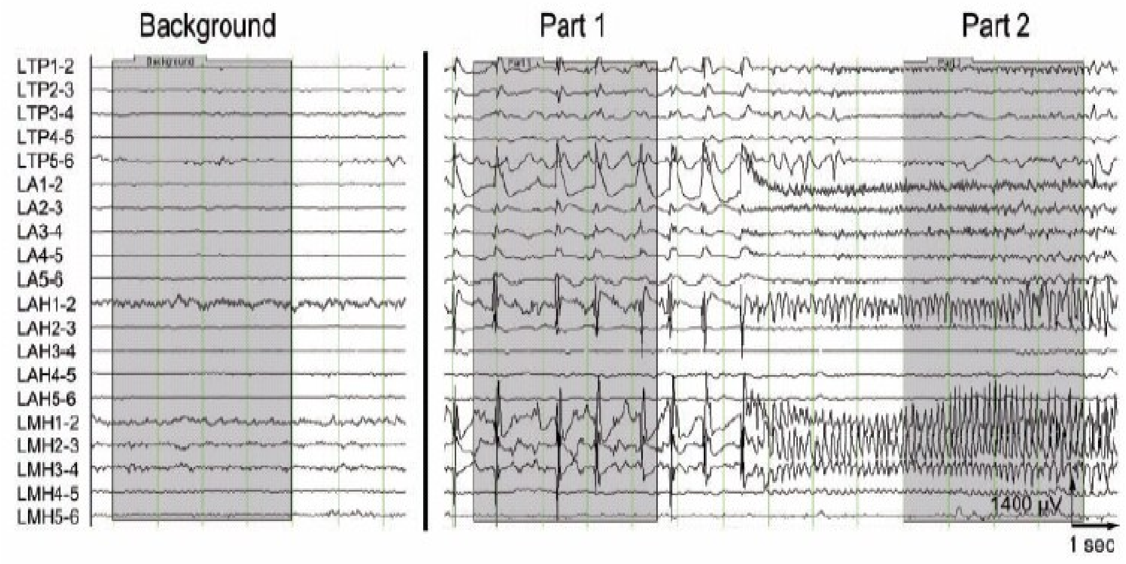

Figure 1.9 An example of background EEG and seizure EEG recorded by intracranial electrodes. Left side shows the background EEG without any clinical abnormalities. Part1 and Part2 are two different stages of a seizure. Reference: Jirsch 2006 [24]

Ripples were initially found in hippocampus (Hip) and entorhinal cortex (EC) areas of freely behaving rats [3, 3, 25, 26]. Discovery of ripples in normal animal brains invoked interest in exploring whether HFOs are also found in pathological tissue or not. Subsequently, attempts at discovering HFOs in rats and humans with epilepsy started and revealed that ripple activities can indeed be found in the hippocampus and EC of both humans and rats with epilepsy [26, 27]. In the first study done on epileptic brains, oscillations faster than ripples in the range of 250-500 Hz were reported. These oscillation were called fast ripples (FRs) and were recorded during the interictal state (period between seizures) from areas adjacent to lesions in the hippocampus of kianic acid treated rats and in the epileptogenic areas of patients with epilepsy [27].

Soon after the first work on humans, further studies were done to understand the relationship between epileptic tissue and HFOs. Large numbers of implanted electrode of varying types were applied in various locations of the brain to record high frequency oscillations before and during seizures. Using micro electrodes (20-40 µm in diameter) in human brain with mesial temporal lobe epilepsy (MTLE) and neocortical epilepsy, HFOs were recorded in hippocampus and neocortical regions [26-30]. Subdural electrodes were used to record ictal and interictal HFOs in neocortical zones [31-33]. HFOs were also recorded by macroelectrodes (surface: 0.8 mm^2, ~1000 times > microelectrodes) in patients with focal seizures in both mesial temporal and neocortical structures [23, 24, 34-43]. Although earlier works were limited to a single type of electrode, combination of different electrodes have been applied in later studies; micro and macro electrode [42], depth and subdural electrode [44, 45].

Depending on the electrodes types and location of recording, a large variety of HFO events with respect to amplitudes, durations and rate of occurrences have been recorded. Table 1.2 summarizes some of the characteristics of HFO from various researches.

Results from various researches have shown that HFOs are associated with regions capable of generating spontaneous seizures [26, 37, 46] and they are found in pre-ictal [38], ictal [24] and interictal [26, 34] periods. Nevertheless, the rate of fast ripples is higher during interictal periods in the SOZ than in other areas [27, 34]. Studies on human brain have also shown that there is a good correlation between resection of the brain region containing fast ripples and surgical outcome [23, 32, 38, 47]. Moreover finding HFOs in the dentate gyrus structure of kianic acid-treated epileptic rats suggests that ripples may be pathologic as well, since there is little evidence that ripples occur in this structure of normal brain. All the clinical evidences seem to suggest that HFOs might be specific surrogate markers of the seizure onset zone.

Table 1.2 Comparison of HFO characteristics in different researches. Note that the rate of occurrence is given for SOZ.

	Author	Year	HFOs Duration(ms)		HFOs Amplitude(µv)		Rate of occurences	
			Ripples	Fast Ripples	Ripples	Fast Ripples	Ripples	Fast Ripples
1	Bragin	1999	50 - 120	15 - 100	100 - 600	100 - 500	0.1 - 20 / min	0.5 - 6 / min
2	Staba	2002	26.1 - 40.2	12.7 - 19.1			2.66 ± 1.2 / 10 min	3.33 ± 0.63 / 10 min
3	Jirsh	2006	10 - 50		40 - 200	5 - 30		
4	Urrestarazu	2007	mean 80	mean 40			0.4 - 80/ min	0 -118/ min
5	Jacob	2008	96.2 ± 45.5	40.6 ± 26.7			12.9 ± 11.2/ min	9.9 ± 22.2/ min
6	Jacob	2009	88 ± 42	36 ± 24			12 ± 17/ min	7 ± 18/ min
7	Schevon	2009					4.6 - 22.46/ min	
8	Zijlmans	2009					13.7 ± 35 / min	2.8 ± 22 / min
9	Crepon	2010	22 ± 11		12 ± 7		1.6 / min	
10	Usui	2010	7- 35		9 - 271			
11	Jacob	2010					24.8/min	0.3/min
12	Andrade-Valenca	2011					43.4 ± 32.7 / min	10.20 ± 11.01 / min
13	Chatillon	2011	74.8 ± 12.6	23.9 ± 5.1	0.8 ± 0.8	1.3 ± 0.8	73.1 ± 31.2	9.8 ± 12.3

In spite of the fact that neuronal networks responsible for HFO generation are not yet well understood, various hypotheses have been proposed for the mechanism underlying these high frequency events.

Ripple mechanism

Ripples are found in hippocampus and parahippocampal structures of rodents [3, 25, 48, 49], non-human primate [50] and humans [6, 26, 28, 51]. "*They are thought to* *synchronize neuronal activity over the long distance to consolidate the synaptic plasticity",* and they seem to be important for episodic memory [52]. In normal brain, it is hypothesized that ripples could be part of mechanisms of memory consolidation and behavioural performance [36] and they are believed to reflect inhibitory field potentials which facilitate information transfer by synchronizing neuronal activity over long distances.

In pathological condition, ripples occur in dentate gyrus. It is believed that they play a role in seizure generation [28] and they may reflect summated synchronous IPSPs generated by subsets of interneurons that regulate the discharges of principal cells [53].

Fast ripple mechanism

In normal condition, fast ripples have been recorded in neocortex (somatosensory cortex), but not in normal hippocampus and parahippocampal structures. In rodents, it is hypothesized that fast ripples may reflect rapid temporal integration of tactile sensory information [54].

In pathological condition it is thought that fast ripples are the basic neuronal events causing epileptogenecity. One hypothesis relates fast ripples to IPSPs of pyramidal cells (long axon cells of the cerebral cortex) that are generated during simultaneous depolarization of these cells by the bursting activity of (CA3) neurons [27, 48, 54]. Similarity in shape of fast ripples and spike population leads to the conclusion that fast ripples might be generated as a result of synchronous firing of principal cells [27, 28, 54]. Abnormal gap junction formation may also contribute to the appearance of fast ripples [55, 56]. Neuronal reorganization underlying epileptogenesis in human mesial temporal lobe epilepsy was suggested as another possibility [28]. On the other hand, it seems likely that fast ripples reflect groups of synchronously firing neurons whose oscillations are out of phase of other groups [57].

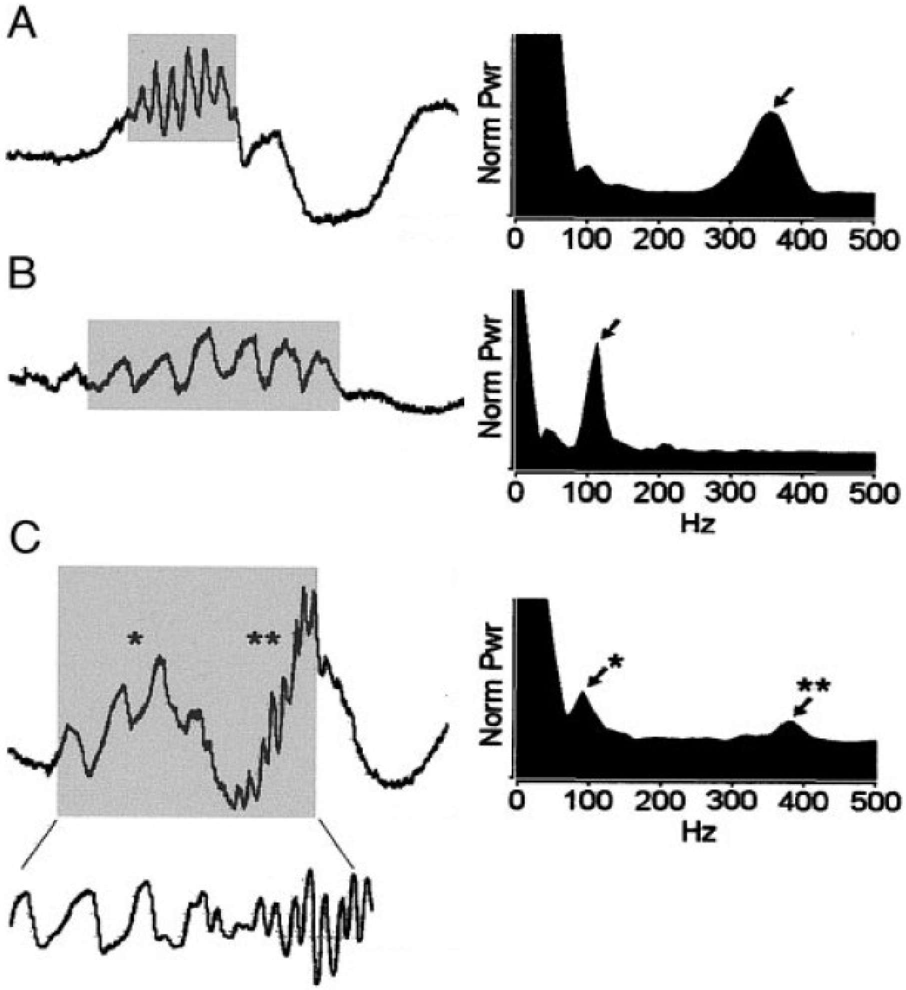

Figure 1.10 HFOs and power spectral analysis. Left: Wideband EEG. Right: Power spectral density histogram. Gray samples show the HFOs. **(A)** Fast ripple, power spectral density shows a peak in the range between 300-400 Hz. **(B)** Ripple. The peak in the PSD is located between 100 and 250 Hz. **(C)** Ripple and Fast ripple (one peak in 100 Hz (*), the other in 400 Hz (**)). Band pass filtered of gray samples is shown in the figure. Reference: [26]

1.11 Motivation and Problem definition

EEG is one the most important assessment tool for neurological disorders. It is used in different clinical practice and pre-surgical evaluation. Among the various disorders of the brain, epilepsy has drawn the most attention because this disorder can affect the quality of life of a person. Traditionally, only low frequency EEG (up to 70 Hz) was considered of clinical relevance to epilepsy disorder. Spikes and sharp waves have been used as two classical biomarkers of epilepsy. Nevertheless, advances in digital EEG recording techniques, such as higher sampling rate (5 times greater or more), have opened new insights into EEG analysis. By recording EEG at higher sampling rate with the aid of intracranial electrodes, waves in frequencies much higher than normal activity range of EEG (100-500 Hz) have been discovered. A large number of experiments and studies have shown that these so-called high frequency oscillations (HFOs) may have a fundamental role in the generation and spread of seizures and they might be EEG biomarkers for epileptogenicity. More importantly, a postsurgical study showed a correlation between surgical outcome and removal of tissue corresponding to channels with high HFO rates [23] emphasizing the fact that HFOs might be considered as biomarkers of epileptogenic brain tissue that help to localize the seizure onset zones (SOZ). Identifying and characterizing HFOs plays a vital role in using them to understand fundamental mechanisms underlying these events that occur under normal and pathological conditions such as epileptogenesis and epileptogenecity.

One of the difficulties in HFO research is the identification of such events in EEG signals. In practice, HFOs are defined as spontaneous oscillations that repeat for at least 4 cycles with frequencies ranging between 80 to 500 Hz which can be distinguished from background EEG. The total duration of these events is a small fraction of the entire length of EEG background. Particularly important is the small amplitude of these events (in the order of µV). Consequently, visual reviewing of large amount of data takes many hours (e.g. marking 10 channels of 10 minutes IEEG can take several hours) which makes the HFOs scoring inevitably highly subjective.

Moreover, despite such de facto definition for HFO events, there is no precise mathematical definition available for HFOs, which makes it challenging for automatic detection algorithms to be implemented.

Although different types of automated methods have been introduced for seizures, spikes and sharp wave detections, to date, the identification of HFOs in IEEG is relatively new and is mostly done by visual review of the IEEG. Development of a robust automated detector is expected to play a vital role in studying HFOs and their relationship to epileptogenesis. Recently a handful of automated HFO detectors have been introduced in the literature. The detectors are based on energy, wavelet functions and neural networks.

In this study, we implement some of the existing methods [26, 55]. To improve the performance of one of these detectors [26], we also develop two versions of this detector to further improve the detection performance. We propose several new methods based on the sharpness of EEG signal. In these methods, the signal is broken into waves and half waves, and the sharpness value of each half wave is compared with those of the neighborhood, allowing the detection strategy to be more compatible with the way a neurologist may identify HFOs.

The rest of the thesis is organized as follows: Chapter 2 provides a review of the existing methods in the literature. The energy-based detectors as well as the sharpness-based detectors will be described in detail in Chapter 3. In Chapter 4, simulated HFO events are used to test the performance of the detectors considered in Chapter 3 and the corresponding results are discussed. Chapter 5 deals with the performance and a discussion of all the proposed detectors using real IEEG data from five patients. Chapter 6 contains the conclusions and some discussion for future work.

Chapter 2 . Literature Review

As discussed in chapter one, high frequency oscillations (HFOs) are postulated to be biomarkers of epileptogenic tissue. Therefore it is anticipated that they can be used in the identification of epileptic regions in the brain. Accurate detection of HFOs can play a vital role in the localization of seizure onset zones.

High frequency oscillations are defined as EEG activity in the range of 80 and 500 Hz with at least four oscillations that can be clearly delineated from the background EEG. Depending on the sampling frequency, recording electrodes, location of the electrodes, and the seizure type, HFOs are characterized by varying durations (10-100 ms) and amplitudes (few to several hundred micro volts).

Recently, identification and analysis of HFOs has been a matter of concern for many electroencephalographers. Limited understanding along with the lack of clear definition of what constitutes an HFO event has made their identification very difficult.

Generally, IEEG is recorded for up to two to three weeks. One of the difficulties in HFO research is the identification of such transients in the prolonged EEG signal. The total duration of HFOs is extremely small (10-100 ms) compared to the entire length of EEG recorded days to weeks. The sparse distribution of these events ((12 ± 17)/min for ripples and (7 ± 18)/min for fast ripples [38]) presents a significant challenge for a reviewer to visually identify these events. Electroencephalographers must spend a great amount of time to score HFO events. For example, it takes more than 10 hours for an electroencephalographer to visually score 10 channels of 10-minute EEG recordings. Manually reviewing data makes visual scoring an extremely tiresome process requiring a great deal of concentration. Fatigue or distraction during visual scoring may easily lead to errors - such as false positive or false negative detection - by electroencephalographers. Moreover, the “Gold standard” definition of what is an HFO event is not yet available and reviewers are not always unanimous in identifying HFO events. Consequently, whenever visual methods are applied subjective interpretations are inevitable.

This problem can be partially addressed by an automatic detector that could be developed to detect these events. Robust and reliable HFOs automatic detectors that are objective and consistent will allow meaningful comparison of different HFO studies in a relatively short time compared to the subjective manual scoring.

In practice, performance of the automatic detection methods is compared to the HFO events that have been visually identified by an EEGer. So an understanding of both the automated and visual scoring techniques is crucial. In this chapter, we will provide more details on visual scoring of HFO events [24, 34, 55] as well as the current state of the literature for computer-aided techniques [4, 7, 26, 32, 33, 42-45, 55, 58-62] used for the detections of HFOs.

2.1 Visual scoring

2.1.1 EEG readings

EEG reading is a process in which electroencephalographers review the prolonged IEEG signals to identify abnormal EEG patterns (spikes, sharp waves, seizures and etc). IEEG is typically reviewed page by page (window of 10-20 seconds) on a computer screen with channels in a specific montage. Each page consists of various channels of EEG that are viewed with desirable time resolution. The rate of data acquisition (sampling rate) and the length of a page determine the time (horizontal) resolution. In digital recordings of EEG, montage, filter, and gain settings can be changed. Depending on the aim of study, the data are displayed with different time resolutions varying between 1s/page to 120s/page. Moreover, to achieve the best visual presentation for interpretation of brain activity, the display gain (sensitivity) needs to be adjusted. Figure 2.1 shows 6 channels of EEG signal displayed in 10 s/page resolutions.

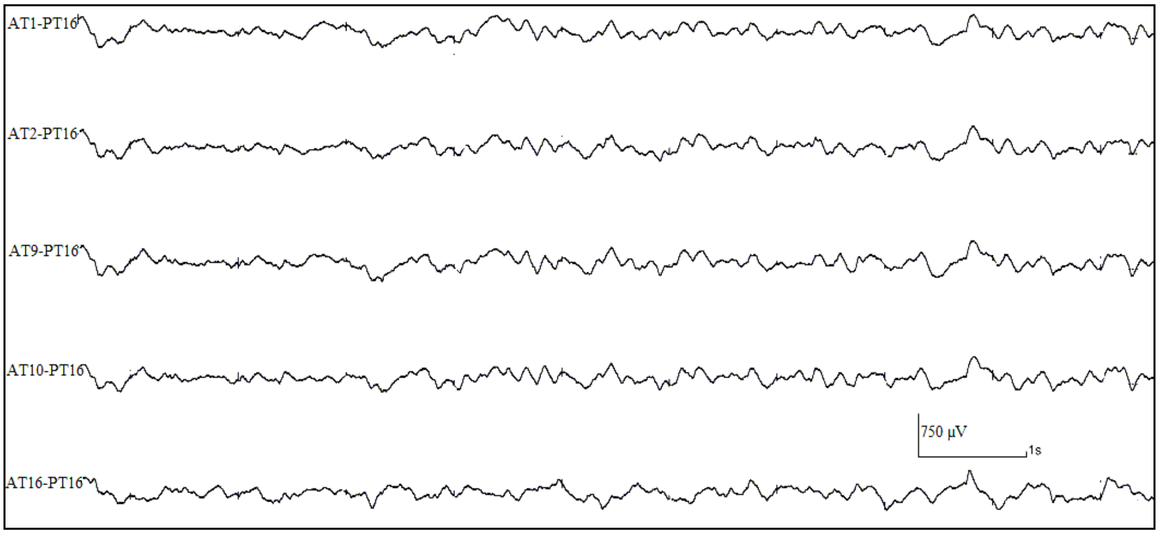

Figure 2.1 Ten seconds of 6 channels of EEG in a computer screen (Bipolar Montage).

2.1.2 Visual Scoring of Seizures

As stated earlier, EEG recording is a test commonly used in clinical evaluation of patients with epilepsy. In epileptic patients, electroencephalographers visually review the IEEG data to distinguish the type and location of seizures. Although there is no stereotypical pattern that characterizes all types of seizures, most seizures include evolution (increase or decrease) in the amplitudes and frequency contents of the EEG signal. Figure 2.2 illustrates 10 seconds of 8 channels of EEG with an average reference montage in an epileptic patient. It can be seen that the amplitude and the frequency contents change at the onset of seizure as marked by the downward arrow.

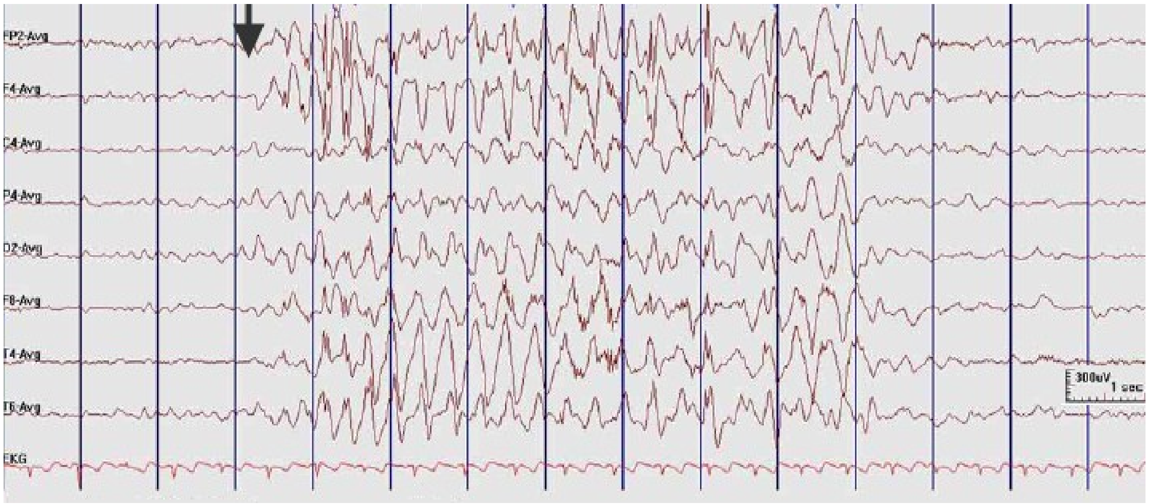

Figure 2.2 An example of ictal EEG signal. Three Hz generalized spike-and-slow wave activities are seen in this patients. The arrow shows the seizure onset time. Reference: [63]

2.1.3 Visual Scoring of HFOs

There is no standard rule or method for visual scoring of HFOs. Electroencephalographers typically apply their own experience and knowledge to mark these events [7, 23, 24, 34, 41, 55, 64]. There are, however, a few studies in the literature that attempt to describe some procedures for visual HFO scoring [23, 24, 34, 41, 55, 64] that have been adopted. The following provides techniques used by two different groups [24, 64] in the literature for visually scoring HFO events.

Usui *et al* [64] applied visual scoring of both the high frequency events and the very high frequency activities (1000-2500 Hz). In the first step, the EEG signal is band-pass filtered in the range of 160 Hz and 3 KHz. To visualize high frequency activities, the time and amplitude axes of the EEG screen are expanded. From the resulting filtered signal, the frequency, amplitude and duration of HFO events are measured with cursors on a computer screen (Figure 2.3). The authors have not provided any information about the criteria that have been applied for the detection of these events.

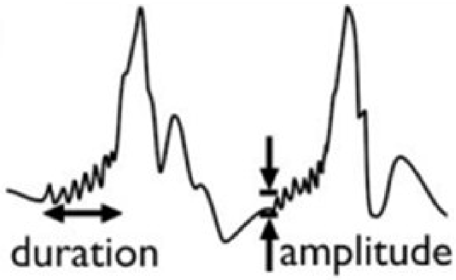

Figure 2.3 Visual Scoring applied by Usui et al. Reference: [21]

Another visual scoring method, which has been applied by many researchers, was introduced by Jirsch *et al* [24, 64]. The following paragraphs provide detailed information on the method that they applied for the visual scoring of HFO events.

The first step in their method is expanding the IEEG channels to the maximum resolution. The reason for the expansion is that HFO events have very small duration (few milliseconds); hence to visualize events better, the EEG channels under review need to be expanded to 1 s/page (maximum resolution) on the computer screen. As can be seen in Figure 2.4, an expanded time-scale of EEG (Figure 2.4B) facilitates visualization of higher frequency components compared to the normal EEG review resolutions (Figure 2.4A).

Later, they use high-pass filters to reject the low frequency contents of the EEG signal. The reason for filtering is that the energy of the raw IEEG signal is inversely proportional to the frequency content. That is, low frequency EEG (in the classical EEG spectral bandwidth < 70 Hz) has higher energy than the higher frequencies (100-500 Hz). The higher frequency components are generally not observable in the presence of low frequency EEG. Therefore to visualize HFOs, IEEG signal must be filtered to highlight the relevant bands. However, Fast ripples (250-500 Hz) have less energy than ripple oscillations (100-250 Hz). Hence to discern these two types of events (ripples and fast ripples), it is necessary to apply two high-pass filters, one with a cut-off at 80 Hz for ripple band and the other at 250 Hz for fast ripple band. In their research, they utilize two different finite impulse response filters (FIR), one with cut-off frequency of 80 Hz and the other with cut-off frequency of 250 Hz.

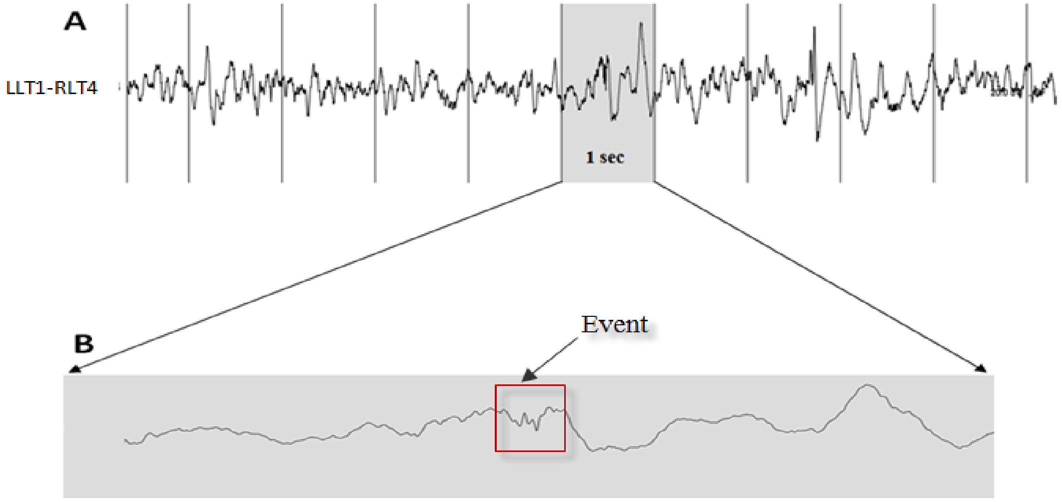

Figure 2.4 **(A)** EEG activity in one channel is shown at 10 second/page. **(B)** Highlighted samples shown at an expanded time-scale with improved visualization of higher frequency components.

Figure 2.5B-C gives an illustration of the IEEG signal after high pass filtering. As can be seen, the high-pass filters remove the high energy of lower frequency components of the signal to help locate HFOs more easily.

In the next step, the computer screen is vertically split into two distinct screens and IEEG signal is expanded for each of the two filter settings. Since HFOs have significantly lower amplitudes than the background EEG (< 70 Hz), the gain must be adjusted to visualize the HFOs.

Finally, the Electroencephalographer examines the expanded EEG in two screens simultaneously. A ripple is marked if an event is clearly visible on the 80 Hz filtered screen and not observed on the 250 Hz filtered screen. An event is scored as fast ripple if it is only visible in the 250 Hz and not in the 80 Hz filtered data [37].

Each event should be easily identifiable as bursts relative to the neighbourhood background in the appropriate band and must contain at least 4 consecutive oscillations (cycles). Once a segment of EEG meets the above criteria, it is marked by the reviewer with the start time (HFO start position) and the end time (HFO end position). Events separated by 8 ms and more are considered to be different events [34].

2.2 Automatic HFO detection

In contrast to visual scoring, automated detection is the application of a set of mathematical rules by a computer algorithm to detect or identify events of interest in the EEG. Automated detection techniques have been most commonly employed in the detection of spikes and seizures. The detection of HFOs has been mostly relegated to visual scoring. More recently, as the interest in HFO has increased, so has the interest in automatic detectors; specifically the investigation of automatic HFO detectors has been of increasing interest since 2002. Though the automatic HFO detection literature is in its infancy, to date, several automated methods have been reported. Some of these methods operate in the time domain [7, 26, 43, 55, 58, 61], while others use time-frequency ideas for their detection [32, 33, 40, 44, 45, 65]. There exists one study that has applied neural network techniques for detection of HFOs [60].

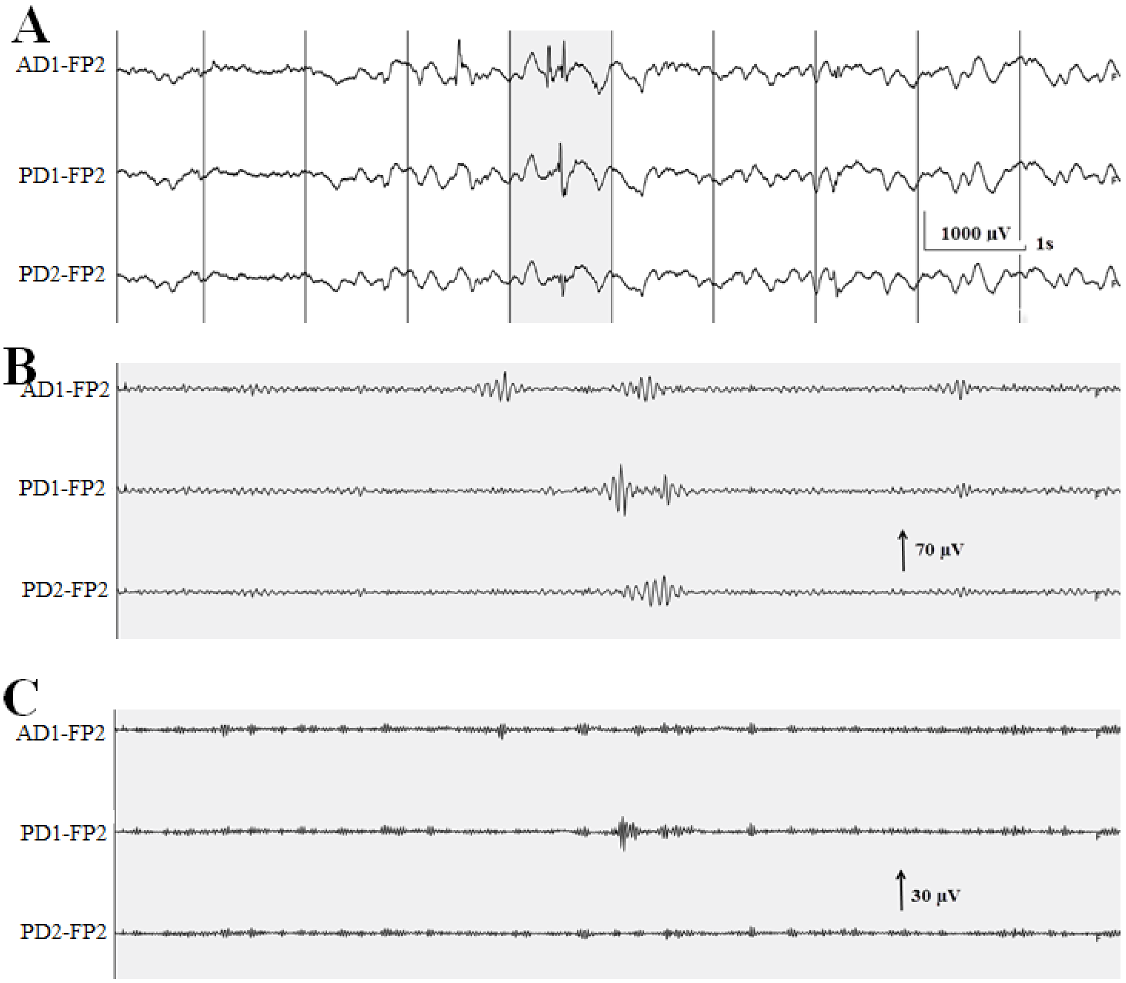

Figure 2.5 High frequency events are visualized with expanded time scale and high pass filtering. **(A)** EEG activity in three channels is shown at the standard time-scale (10s/page). **(B)** Highlighted sample displayed in expanded time scale (1sec/page) with 80 high pass filter**.** **(C)** Highlighted sample displayed in expanded time scale (1sec/page) with 250 high pass filter**.** Note the adjustment of the amplitudes for filtered data.

The time domain detectors are mostly based on the change in the energy of the EEG relative to the background data. The main difference between these detectors is the manner in which the energy is defined and computed. Four of the more common methods used in the literature are based on root mean square energy [26], running average energy [7], short-time line-length energy [55], and teager's energy [58]. The following describe some of these more commonly used methods in detail.

The earliest automated HFO detector was introduced by Staba *et al* in 2002 [26]. This method is based on the moving average of the root mean square of the signal. Ten minutes of non-rapid eye movements (NREM) sleep-staged epoch of wideband EEG (sampled at 10 KHz) was used in their database. Small segment of the wideband EEG is shown in the Figure 2.6A. The highlighted samples in this figure show a HFO event. Each channel of EEG is digitally band-pass filtered using an FIR filter with cut-off frequencies between 100 and 500 Hz. Figure 2.6B illustrates the band-pass filtered data of the small segment shown in the Figure 2.6A.

The resulting filtered signals are processed in 3 ms window to calculate the root mean square amplitude.

$$E(t) = \sqrt{\frac{1}{N} \sum_{k=t-N+1}^{t} x^2(k)} \tag{2.1}$$

where $E(t)$ is the RMS value of signal, N is number of samples in the 3 ms running window and x(t) is the band pass filtered EEG signal (Figure 2.6B).

As can be clearly seen in Figure 2.6, the RMS energy during the HFO events is higher compared to the surrounding background EEG. Hence, using a threshold to identify an increase in the RMS values may reveal the presence of HFO event. In this method, the threshold was developed by using RMS energy of the entire EEG signal [26] and defined by following equation:

$$\delta_{RMS} = 5\,\sigma + \mu \tag{2.2}$$

where δ_{RMS} is the threshold value, σ is the standard deviation of $E(t)$ and μ is the mean of $E(t)$ of the entire EEG, as shown in Figure 2.6C by the red dashed line.

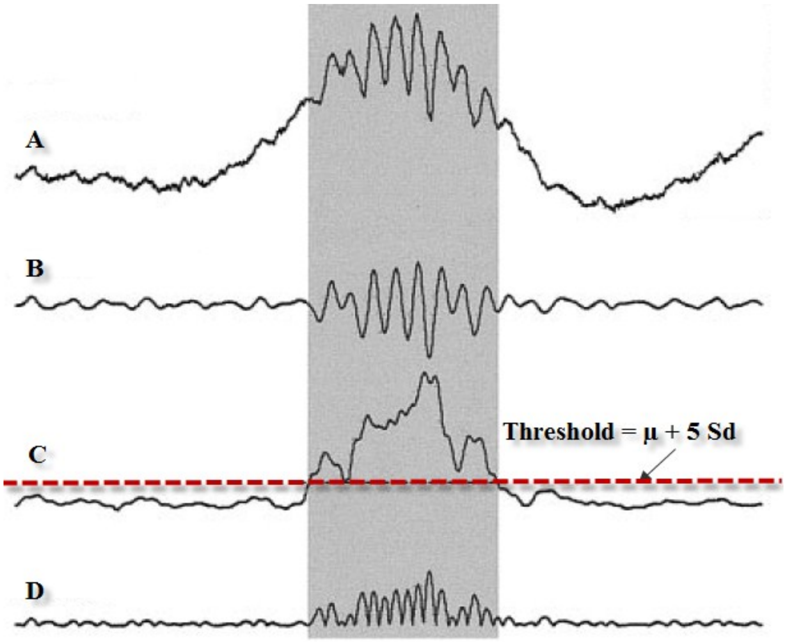

Figure 2.6 HFO detection method proposed by *Staba* in 2002. Highlighted segment shows a HFO event. (A) Wideband EEG. (B) EEG signal is band pass filtered between 100 and 500 Hz. (C) root mean square of the band pass filtered data, dashed red line shows the threshold value which is selected as5 standard deviation above the mean of the entire length of RMS values. **(D)** Post processing stage: band pass filtered signal (B) is rectified above zero. 6 peaks greater than 3 SD above the mean of the rectified signal is needed so that a segment is considered as HFO event. Note that the threshold for post processing is not shown in this figure. Reference: [26]

RMS energy of the EEG segments that are greater than δ_{RMS} for minimum duration of 6 ms are considered as candidate HFO events as highlighted by the gray section shown in Figure 2.6C.

Post processing is applied on the candidate HFOs to minimize false positive events. In post processing stage, number of peaks in the rectified band-pass filtered signal (above 0 μV, Figure 2.6D) of the candidate events are counted. Each candidate event must have at least six peaks with amplitude greater than 3 SD from the mean baseline signal to be retained as a valid HFO event; otherwise it is rejected. Figure 2.6 shows the signal at each step of this method.

Based on the author's report, this technique is capable of detecting more than 84% of events which had been marked visually (sensitivity), however there was no report related to the specificity of this method [26]. Besides, the criterion for manually scoring these events was not reported.

The main drawback of this method is the threshold that is selected over the entire EEG signal. This affects the detection's sensitivity by the presence of artifacts and powerful HFOs. Existing noise and strong events increase the threshold value; as a result, valid events with low amplitudes will not be detected. Based on the threshold computation which is defined for the entire EEG signal, such methods are considered as batch processing methods. That is, all the data must be available before any processing. Moreover, for long duration data, as is the case for epileptic patients, where EEG is recorded for days to weeks, such approaches are not suitable.

Smart [58] proposed a method for HFO detection which is based on the nonlinear energy value and curve length. Figure 2.7 shows the flowchart of the method. In this method, the EEG signal is sampled at 200 Hz and HFO frequency range is defined between 60 and 100 Hz. IEEG signal is first divided into consecutive 1-minute epochs for processing. To improve signal to noise ratio between the background activity and the HFO events, the data is high-pass filtered at 62 Hz with a Chebychev filter. Nonlinear energy (Teager) and curve length are computed from the high-pass filtered data:

$$NE(n) = x^2(n) - x(n-1)x(n+1) \tag{2.3}$$

where x is the high pass filtered data and NE is the non-linear energy, and

$$CL(n) = \sum_{k=n}^{n+N} |x(n-1) - x(n)| \tag{2.4}$$

where CL is the curve length as a function of time and N is the number of samples in an epoch.

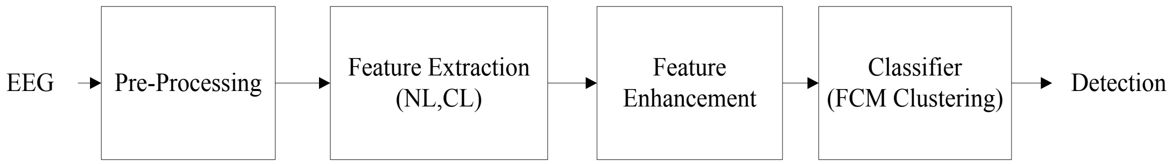

Figure 2.7 Flowchart of the automatic HFO detection method proposed by Smart et al.

A threshold is applied to each feature series. In this method, fuzzy c-mean (FCM) clustering algorithm is used as a classifier. Nonlinear energy and curve length values of the filtered signal are used as input to the classifier. Classification via FCM clustering produces a binary sequence denoting HFO presence (1) or HFO absence (0). The results obtained by this method are compared with the HFO events marked by two neurologists. The average sensitivity was reported as 87%. Based on the authors' report, this algorithm differentiates between HFOs and non-HFO EEG well, but triggered very often resulting in many false positive events. They, however, did not describe what constitutes an HFO event, i.e., the definition of HFO employed by them.

Another automated HFO detector was presented by Khalilov *et al* [65]. This method was based on the wavelet transform (Complex Morlet wavelet). In this method, duration of the window of analysis depends on the frequency band (the higher the central frequency, the shorter the window duration). In the first step, the EEG signal is convolved with the complex Morlet's wavelet:

$$S(t) = w(t, f_0) \ * x(t) \tag{2.5}$$

where $x(t)$ is the EEG signal, $' * '$ indicates the convolution operation, and $w(t, f_0)$ is the complex Morelet's wavelet with a Gaussian shape both in the time domain and the frequency domain, around the central frequency f_0 and described by the equation:

$$w(t, f_0) = A \, e^{\frac{t^2}{2(SD_t)^2}} \times e^{2\pi f_0 t} \tag{2.6}$$

SD_t being the standard deviation of $w(t, f_0)$ in the time domain. The standard deviation of $w(t, f_0)$ in the frequency domain is defined as $SD_f = \frac{1}{2\pi(SD_t)}$.

The wavelet family was chosen such that the ratio of the central frequency to the bandwidth (SD_f) is equal to 5 ($\frac{f_0}{SD_f} = 5$), with f_0 sampled logarithmically from 10 to 200 Hz. In the next step, the time-varying energy ($E(t, f_0)$) of the signal in a frequency band around (f_0) is obtained by the following equation:

$$E(t, f_0) = |S(t)|^2 \tag{2.7}$$

Energy value is compared to a threshold to decide whether there is an event or not. Threshold is defined using Equation (2.2) from the $E(t, f_0)$ of the baseline EEG signal located far away from the events. If the local maximum of the energy value exceeds the threshold (δ_{th}) lasting longer than duration threshold (δ_D), the segment is considered as an HFO event. Note that δ_D is a function of frequency and is computed as follows:

$$\delta_D(f) = \frac{k}{f} \tag{2.8}$$

where k is the number of wave-cycle (5 in their work), and f is the related frequency band. This method was designed to specifically minimize the number of false positive detections. Although the performance of this method was not reported by the authors, the sensitivity and specificity reported for this method implemented by another group [59] were 70.8 % and 13 %, respectively.

Gardner *et al* [55] described an HFO detection method based on short-time line-length (STLL) energy. This method is basically similar to the method proposed by Staba *et al* [26] but with a few modifications. The EEG used in this research was recorded by a combination of subdural grids and depth electrodes and sampled at 200 Hz. Using an IIR filter (4^{th} order Butterworth), data are band-pass filtered in the frequency ranges of 30 and 100 Hz. Signal is then divided into consecutive three minute epochs. Energy value of the signal is computed with STLL energy function which is given by the following equation:

$$\hat{E}(t) = \sum_{k=t-N+2}^{t} |x(k) - x(k-1)| \tag{2.9}$$

where N is the number of samples in an epoch, and x is the high pass filtered EEG signal. Non-parametric threshold was selected by examining the empirical cumulative distribution function (ECDF) of line-length values ($\hat{E}(t)$) from a small training set, which in this study was heuristically chosen as 97.5 % and applied to each epoch (3 min length) during processing. Segments with amplitudes higher than the threshold lasting at least 85 ms were detected as HFOs. Sensitivity and specificity of this technique were reported to be 75% and 88% respectively [55].

Another type of HFO detection method is based on the artificial neural network. Firpi *et al* [60] used neural network (NN) and particle swarm optimization (PSO) to detect HFOs. EEG signal was sampled at 200 Hz and HFO frequency range was defined between 60 and 100 Hz. In the pre-processing stage, band pass filter (Butterworth, F_{c1} = 30 Hz, F_{c2} = 96 Hz) and notch filter (60 Hz) are applied on the EEG signal. The data is then divided into segments of length 0.1 s (L) with 40% overlaps(O). Artificial feature of the band-pass filtered data is calculated by following equation:

$$y[k] = \frac{1}{L} \sum_{i=1+(k-1)D}^{D(k-1)+L} \emptyset([x_i \; x_{i-1} \; \cdots x_{i-(m-1)}]) \tag{2.10}$$

where $\emptyset(.)$ is the neural-artificial feature function optimized by the PSO algorithm, x is band pass filtered IEEG signal, L is the length of segment, D is the segment that doesn't overlap with the previous segment $(O = L - D)$. The neural network applied in this method has 4 layers with 6 nodes in first hidden layer, 8 nodes in second hidden layer and 107 weights. PSO-NN is a supervised hybrid algorithm that detects underlying patterns to separate HFOs and background activity. The classifiers used in this method are threshold and k-nearest neighbor rule that make a decision as to whether HFO is present or not. Depending on the classifier type, two detectors were developed by the authors that were referred as to M3 (classifier: threshold) and M4 (classifier: k-nearest neighbor rule). It has been reported by the author that M4 has a better performance with identical sensitivity and specificity of 75%. This method was designed as a patient-specific detector that requires a large number of sample patterns for training including HFOs and background (*a priori* knowledge).

Khosravani *et al* [45] presented an algorithm based on short-time Fourier transform (STFT) analysis. In this work, after preprocessing stage (involving detrending and removal of DC baseline shift), EEG is segmented with a running window of 2 sec with 50% overlap. These segments are then analyzed by the STFT algorithm with a temporal resolution of 500 ms and 50% overlaps. Three-dimensional data (time vs. frequency vs. power) is then summed in the frequency dimension within five different frequency bands (0-100 Hz, 100-200 Hz, 200-300 Hz, 300-400 Hz and 400-500 Hz). When the power of the segment increases in higher frequency bands, the HFO event is detected.

Crepon *et al* [44] proposed a semi- automatic algorithm which was based on the Hilbert transform. In this detector, the envelope of the band-pass filtered signal (180-400 Hz) is computed using Hilbert transform. Threshold is defined equal to 5 SD for the entire length of the envelope. Using this threshold, local maxima are automatically detected. Finally all the detected events were visually reviewed for post validation. Sensitivity and specificity were reported as 100% and 90.5% respectively.

Recently, another method has been presented by Zelmann *et al* [61] from Montreal Neurological Institute (MNI, McGill University) that is a combination of the two methods in terms of the energy function [26] and the threshold value [55]. The data in this study was recorded by depth macro-electrode and were sampled at 2000 Hz. This proposed algorithm consists of three detectors; a baseline detector and two HFO detectors. Baseline detector is based on wavelet entropy introduced by Chander in 2007 [59]. To detect the EEG baseline (the segments of EEG where there is no oscillatory activity of any kind), the EEG is divided into segments of 125 ms with 50 % overlaps. Normalized wavelet (Complex Morlet wavelet) power of autocorrelation is computed for each segment and wavelet entropy (WE) is calculated. The maximum value for WE, WE_{max}, is reached for white noise. Subsequently, the threshold is selected as a percentage of WE_{max} ($\delta_{th} = 0.67WE_{max}$, in their work). If minimum value of WE of a segment exceeds the threshold (δ_{th}), background is detected. Using the above, the length of baseline for each channel is computed. The channels with at least 5sec baseline are defined as channels with sufficient baseline, while others are referred to as channels with continuous high frequency activities. For channels with adequate baseline, HFOs detection is based on RMS energy of the band-pass filtered signal (FIR filter, F_{c1}= 80 Hz, F_{c2} = 450 Hz) as in the method of Staba *et al* [26]. Threshold is defined as 99.9999 percentile of empirical CDF of 10 sec baseline's energy. Segments with energy greater than threshold and the length of at least 10 ms are considered as HFOs. In epochs (1 minute data) without sufficient baseline, the iterative approach is implemented. In these epochs threshold value is defined as 95 percentile of ECDF of each epoch. Segments with the RMS values greater than this threshold are defined as events. The detected events are removed from the segment and another threshold is set using the remaining data in the segment, and this procedure is repeated until no more events are detected. Average sensitivity and specificity reported for this method were 91.2 % and 55 %, respectively [66].

2.3 Summary

In this chapter, we have reviewed most of the published literature on HFO detection; visual scoring as well as automatic detection methods. Small contribution of HFO event durations compared to the background signal as well as their sparse distributions make visual HFO scoring a tiresome process in which subjectivity cannot be prevented. Automatic detection of such transient events would provide an objective measurement scheme. Results from the automatic detectors are compared with those scored visually. In the existing literature, most of the HFO automatic detectors are based on the energy of the signal. There are a few detectors that are based on wavelet transform and neural networks. However, the most popular detector used by various investigators is the method proposed by Staba *et al* [26] which applies the root mean square (RMS) as the energy function. Different performances have been reported for various methods. The sensitivity of detectors varies between 70% and 100%, whereas the specificity ranges between 13% and 90%. However, comparison between automated HFO detectors is not an easy task. Following reasons can be considered as difficulties in assessing or comparing the performances of automatic detection methods:

1) Varying IEEG recording techniques
2) Different electrode locations and pathologies across patients
3) Different definitions for HFOs (i.e. frequency bands)
4) Lack of gold standard for defining HFO events

Hence care must be taken when comparing the performance of the detectors.

Chapter 3 . Methods for HFO event detection

In the previous chapter, we reviewed some of the existing methods which are used for HFO detection. The methods proposed by Staba *et al* [26] and Gardner *et al* [55] are the two methods that have been implemented by various researchers [29, 42, 47, 67] in one form or another. We refer to the methods as the "RMS" and "STLL" methods, respectively. As a first step, in our work, we also implement these methods and then modify the RMS method into two ways, referred to as MS1 and MS2. Since in all of the above methods, energy of the signals is applied to detect the HFO events, we refer to them as the energy-based algorithms.

We also present three new algorithms for HFO detection that are based on the sharpness of the EEG signal and refer to them as sharpness-based algorithms.

Preprocessing of the EEG signal plays an important underlying role in the analysis of EEG signals. Due to the fact that preprocessing stage is identical to all the methods we will be presenting, we first provide a brief review of this concept, and describe the RMS and STLL methods in detail. We will then present the modified versions of the RMS method as well as the proposed sharpness-based techniques for detecting HFOs.

3.1 EEG Preprocessing

Raw EEG signal has amplitude in the order of μVolts with an energy that is inversely proportional to the frequency. Figure 3.1A shows 5 seconds of unfiltered EEG signal with its power spectral density shown in Figure 3.1B. It can be seen that the frequency spectra of the raw EEG displays a smooth quasi-exponential that decays at gamma frequencies (30 Hz < f <70 Hz, Figure 3.1B). Higher energies are present at very low frequencies (0.1-10 Hz) followed by progressively lower spectral power at higher frequencies (Figure 3.1B).

Removing the low frequency content of the signal would highlight the low-level power of the high frequency content and improve the ability to identify the sharp or fast components in the EEG. Therefore, in order to emphasize the effective information in the high frequency range, EEG signals must be high-pass filtered. Since the frequency contents of HFOs ranges between 100 and 500 Hz, a high pass filter with cut-off frequency of 100 Hz is applied to reject the low frequency content revealing the energy of the high frequency content (100-500 Hz, see Figure 3.2D).

To avoid phase distortion that can alter various temporal relationships in the EEG waveforms, filters with linear phase are desirable. Linear phase response is obtained with a finite impulse response filter, but the filter order must be high. In this research, we utilize a FIR filter, defined by:

$$H(z) = \frac{X(z)}{S(z)} = \sum_{k=0}^{N} b_k \, z^{-k} \tag{3.1}$$

where $S(z)$ and $X(z)$ are the Z transforms of the unfiltered and filtered EEG signals, $s(t)$ and $x(t)$, respectively. N is the order of the filter which in this study is set to 128. Figure 3.2 shows a raw and high-pass filtered EEG signal in both the time and frequency domains.

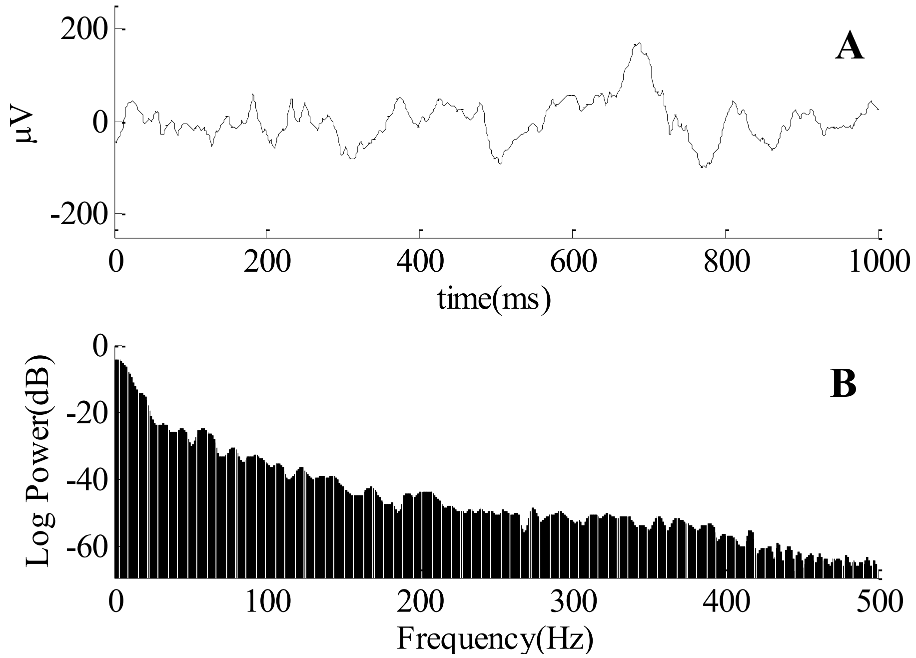

Figure 3.1 EEG signal and power spectral density. **(A)** 5 seconds of unfiltered signal. **(B)** Power spectral density (PSD) of the unfiltered signal. It can be seen that higher frequency contents of the EEG signal have significantly less energy values than those of the lower frequency

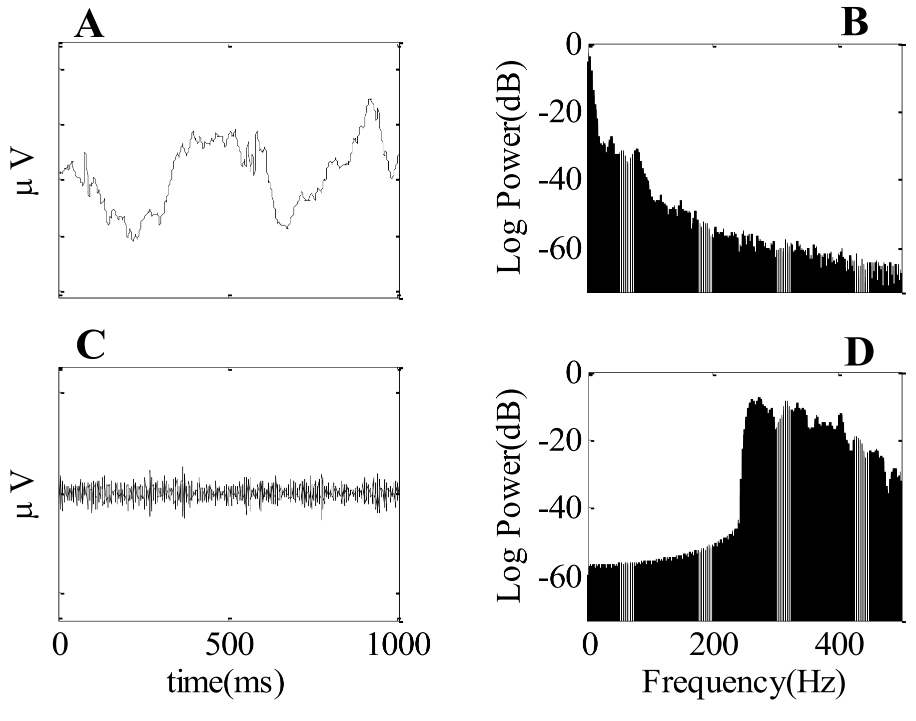

Figure 3.2 Power spectral analysis for a raw and filtered EEG signal. **(A)** Unfiltered EEG (5 seconds). **(B)** Power spectral density of the unfiltered signal. **(C)** High-pass filtered EEG. **(D)** Power spectral density of the high-pass filtered signal.

Since in this study, zero-phase is desired, forward-backward filter is applied to the input signal $s(t)$. That is, once $s(t)$ is filtered in the forward direction, the filtered sequence is reversed and is run through the filter again.

Other important factors that can affect the results of EEG analysis are artifacts. An artifact in electroencephalography is any recorded electrical potential, which is not of cerebral origin. The main artifacts can be divided into 2 categories: physiological (patient-related) and non-physiological (recording system) artifacts.

Physiological artifacts are much more challenging to handle than non-physiological ones. The patient-related artifacts are signals recorded from other sources such as eye blinks (EOG), electrocardiograph (ECG), and electromyograph (EMG).

EOG artifacts are generally high amplitude patterns in the brain signal caused by blinking of the eyes, or low frequency patterns caused by eye movements (such as rolling of the eyes) [68]. Eye movements are typically observed in almost all EEGs (see Figure 3.3). These artifacts are generally limited to electrodes in the frontal part of the head and are most useful in identifying the sleep stages. The eyeball acts as a dipole with a positive pole located in the cornea (anterior) and a negative pole located in the retina (posterior). When the globe rotates around its axis, it generates a large amplitude alternate current field which is detectable by any electrode near the eye.

ECG is the electrical activity which is recorded from the heart. ECG produces small spikes that are recurrent (See Figure 3.4, last channel (red)). ECG artifact is recognized by its rhythmicity/regularity and coincidence with the ECG tracing. Each "sharp wave" is considered as an artifact if it is synchronous with each QRS complex of the ECG channel, (see Figure 3.4).

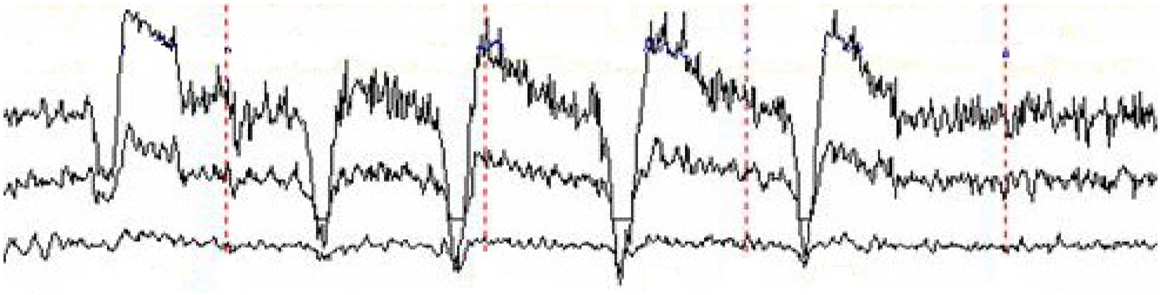

Figure 3.3 Artifact due to eye movements in an EEG signal. Eye movements cause a low frequency signal (< 4 Hz)

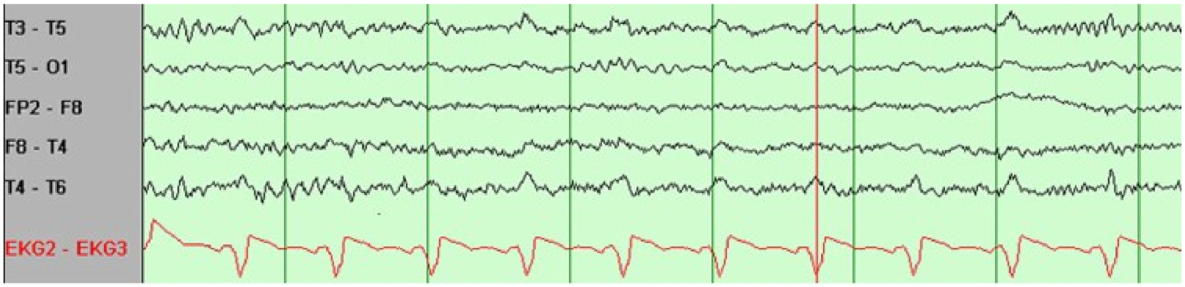

Figure 3.4 Regular (periodic) slow waves best observed at midtemporal and posterior temporal electrodes T4-T6 and T3-T5. These clearly are related to ECG. The duration and morphology are those of pulse artifact, but as demonstrated by the marker, no delay occurs. Reference: http://emedicine.medscape.com

An electromyograph (EMG) detects the electrical potential generated by muscle cells (in rest and contraction). EMG artifacts created during a seizure, muscle contraction, or during movements are due to increased muscle tone. EMG can also be produced by chewing, respiration and facial movement (i.e. tongue, forehead, jaw, eyelids, and muscle of scalps). These artifacts are most prominent in individuals who are tense during EEG. Similar to what was discussed for the eyes, tongue has its own dipole electric charge that can be often picked up by the EEG electrodes and can affect the recorded brain wave. Figure 3.5 illustrates an example of EMG artifact generated by the jaw movement of a patient.

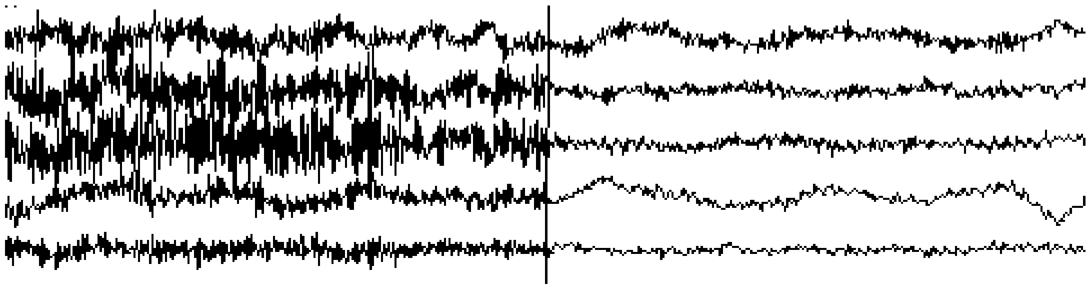

Figure 3.5 Muscular activity (EMG) generated by jaw movement. Reference: www.samuelboudet.com

Among the above physiological artifacts, ECG and EOG signals have frequency content lower than 100 Hz (ECG ranges between 0.5 and 40 Hz, and EOG frequency is mostly below 4 Hz) and they are easily rejected with a high pass filter (F_c = 100 Hz) which is used for the detection of HFO events. However, EMG activity has a wide frequency range, being maximal at frequencies higher than 30 Hz. They play an important role in signal distortion and care should be taken while analyzing the data. These events can be removed in the final visual review by the electroencephalographers.

The non-physiological (system) artifacts are 50/60 Hz power supply harmonics, cable defects, and electrode disconnection. Depending on the source of the problem, strong signals from A/C power supply can corrupt the data in some or all of the electrodes.

Since the power-line frequency of 50/60 Hz is well below the HFO range, it can be easily removed by a 100 Hz filter. However, harmonics of the power-line noise in the range of 120-480 Hz may still persist in the high-pass filtered EEG signal and distort the signal. Such noises can cause problems interpreting low amplitude waveforms. Moreover, these contaminations may impact the various thresholds in the detection algorithm and affect the performance of the detector.

To suppress the harmonics due to power lines, notch filters can be applied (Figure 3.9B).

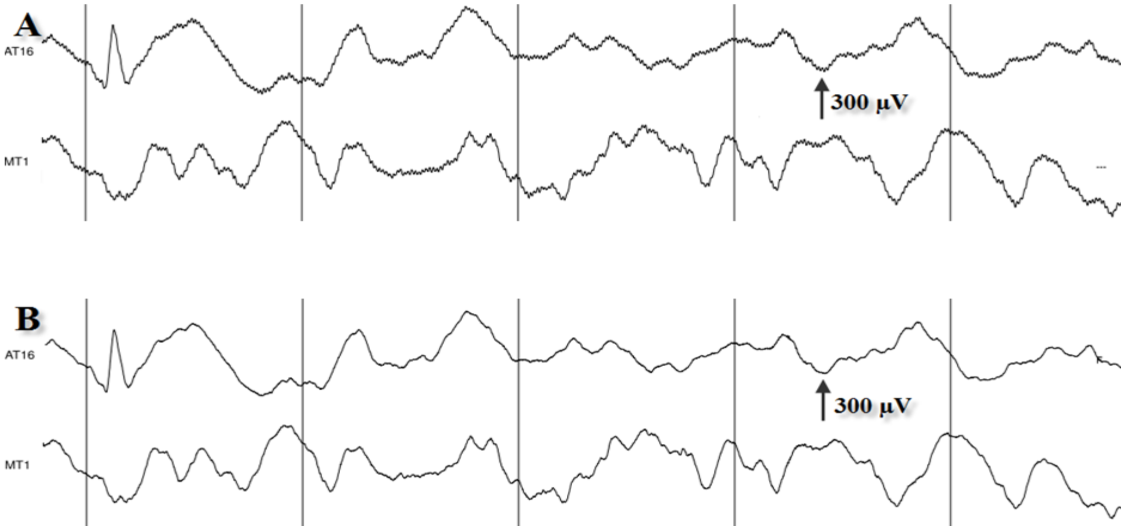

Figure 3.6 Affect of power line noise on EEG signal. **(A)** 5 seconds EEG signal corrupted with power line noise. **(B)** Notch filter was used to remove the power line artifact.

Central frequency of the notch filter is set to the frequencies of the harmonics of the power line in the range of 120 and 500 Hz (120,180,240,300,360,420,480 Hz). In this study, we use a second order infinite impulse response (IIR) notch filter defined by the following filter, which can effectively be applied to track a single sinusoidal signal [69, 70].

$$H(Z) = \frac{1}{2}\frac{(1 + a_2) - 2a_1 z^{-1} + (1 + a_2)z^{-2}}{1 - a_1 z^{-1} + a_2 z^{-2}} \tag{3.2}$$

The notch frequency ω_0 and 3-dB rejection bandwidth Ω are related to the filter coefficients a_1 and a_2 by the following equations:

$$a_1 = \frac{2\cos(\omega_0)}{1 + \tan(\frac{\Omega}{2})} \tag{3.3}$$

$$a_2 = \frac{1 - \tan(\frac{\Omega}{2})}{1 + \tan(\frac{\Omega}{2})} \tag{3.4}$$

The quality factor (Q) of the filter is fixed in such a way that the rejection bandwidth (Ω) of 4 Hz is obtained; for example, if ω_0 is set to 120 Hz, the frequencies in the range of 118-122 Hz define the rejection band. Figure 3.7 shows a magnitude response of a notch filter with the central frequency of 120 Hz.

Figure 3.9A shows a 1-second epoch of EEG signal that includes the background EEG and HFO event along with the power line contamination. As can be seen by the corresponding power spectral density (Figure 3.9B), this signal is contaminated by the power line harmonics (180,300 and 420 Hz). Figure 3.9C shows the resulting filtered signal where the power line noise is minimized. Figure 3.9D shows the corresponding PSD where the harmonics have been removed.

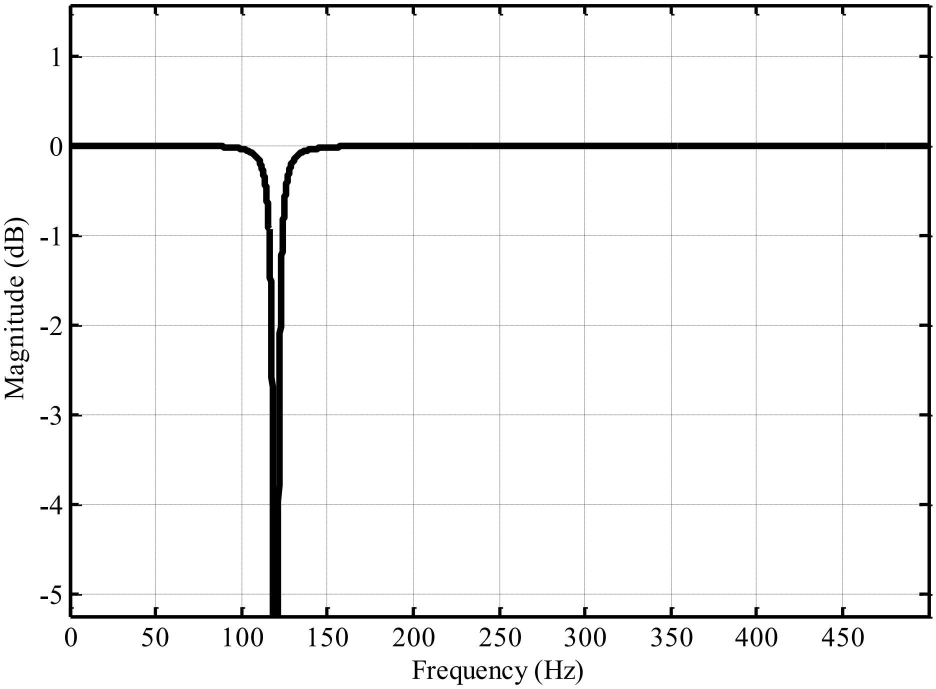

Figure 3.7 Magnitude response of notch filter. The central frequency is set at 120 Hz, and the frequency in the range of 118-122 (Δf = 4 Hz) is rejected.

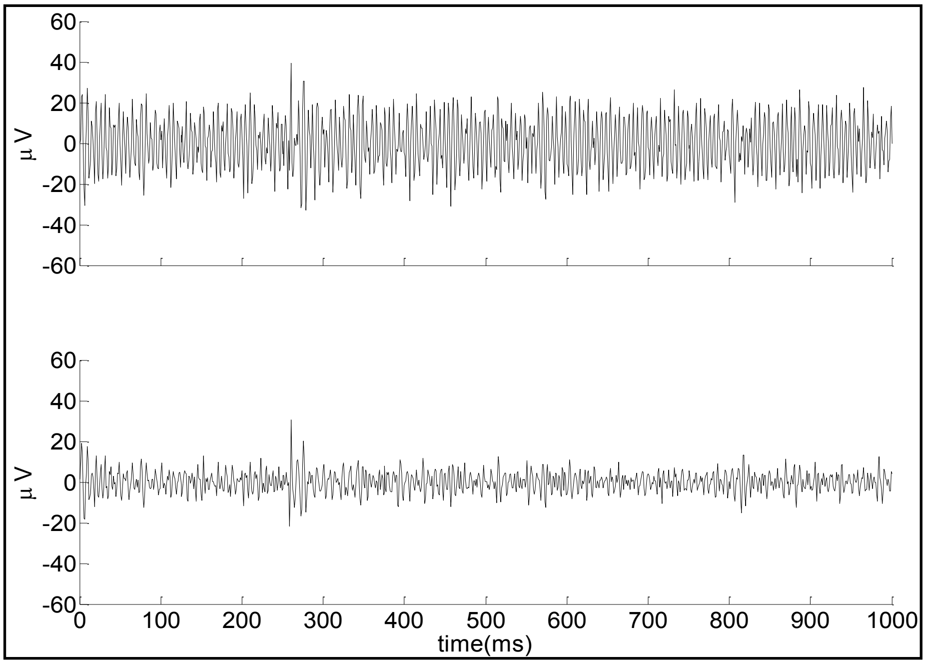

Figure 3.8 High pass filtered data. (Top) High pass filtered (>100 Hz) EEG signal. (Bottom) High pass filtered signal after applying notch filters and removing power line harmonics.

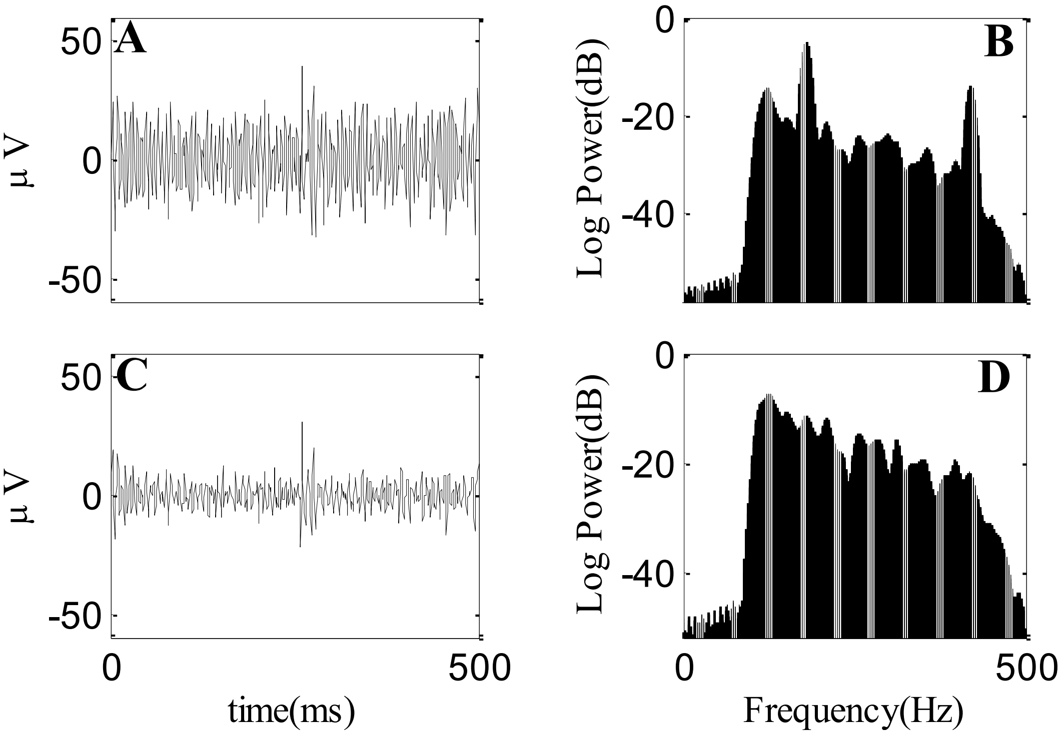

Figure 3.9 EEG signal (time and frequency domains). **(A)** High pass filtered data without using notch filter in time domain **(B)** and frequency domain. **(C)** Harmonics of power supply located at frequencies 180 and 420 Hz was removed by notch filters **(D)** Frequency representation of signal after notch filter.

3.2 Automatic detectors

3.2.1 STLL detector

In the original *STLL* method [55], the data was sampled at 200 Hz, and the high frequency oscillation events were defined in the range of 30 and 100 Hz. The high-pass filtered signal (≥ 30 Hz) was divided into 3 minutes consecutive epochs and the energy of the filtered signal was computed with the short-time line length energy function (3.5) for each epoch.

$$\hat{E}(t) = \sum_{k=t-N+2}^{t} |x(k) - x(k-1)| \tag{3.5}$$

The HFO detection threshold was selected as 97.5 % of the empirical cumulative distribution function (ECDF) of the energy value. Overall procedure applied in this method is shown in the block diagram of Figure 3.10.

The original method (STLL) was designed for data sampled at 200 Hz, limiting the detection to those events in the gamma band (30-100 Hz). However, in our research, the data is sampled at 1000 Hz and we aim to detect ripples and fast ripples in the 100-500 Hz band. Due to the differences of the sampling rates and HFO frequency ranges between our research and the original work, the direct implementation of this method is not possible. Consequently, we have introduced some small modifications in implementing the STLL method.

In the original work [55], the data is sampled at 200 Hz and the window length used to calculate the STLL energy is 17 samples (85 ms at the sampling rate of 200 Hz). However, the data in our research is sampled 5 times faster than that of the original work

[55]. Because of the differences in the frequency content of the duration of each cycle, the window length of 85 ms was replaced by the window length of 17 ms. The minimum duration for an event applied in the original research is defined as 16 samples (80 ms at the sampling rate of 200 Hz). For a comparative assessment of the performance of the detectors, we used the minimum length of events reported by Staba *et al* [26] for all detectors which is equal to 12 ms.

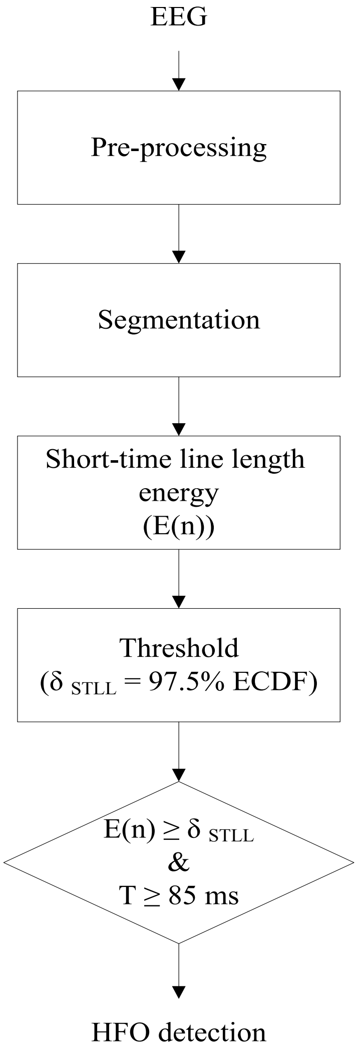

Figure 3.10 Block diagram for HFO detection method proposed by *Gardner* [2].

Due to the different bandwidths used to identify HFOs, the band-pass filter with cut-off frequency (30-85 Hz) in the original work [55] is replaced by a high-pass filter with a cut-off frequency of 100 Hz in our research.

Finally as the last alteration, we reduced the length of the epochs. The data in the original work [55] consist of fourteen 3-minute epochs selected from a single channel, whereas we selected ten 1-minute epochs for each channel. Our justification for this change is that the total duration of HFO events is a small fraction of the total epoch duration and hence, one minute epoch can still provide a reasonable estimate of the local background energy while addressing the evolving background EEG. Moreover, by segmenting our database (10 minute/channel) into 3-minute non-overlapping epochs, we cannot use the complete data for this method (10 minute EEG signal) and this results in poor detection performance for this detector compared to other detectors (RMS, MS1, MS2 and proposed methods).

Table 3.1 summarizes the relevant modification to the STLL detector.

Table 3.1 Parameters used for original short-time line length method and the modified version. Column two indicates the parameters used in the original short-time line length detector, the third column lists the parameters of the modified approach. The last column provides the rationale.

Parameters	**STLL (*Gardner*)**	**Modified STLL**	**Rationale**
STLL Window length	85 ms	17 ms	Differences in the frequency content of the duration of each cycle
Duration threshold	80 ms	12 ms	
Epoch length	3 minutes	1 minute	Different lengths of database (3 minutes vs. 10minutes)
filter (cut-off frequency)	Band pass (30 - 85 Hz)	High pass (100 Hz)	Distinct bandwidth for HFO events (30-100 Hz vs. 100-500 Hz)

In order to implement this method, as already mentioned, a finite impulse response filter (FIR) is required to reject the high-energy low-frequency contents of the EEG signal ($\leq 100\ Hz$). The filtered signal is divided into epochs of one minute length. The duration of the EEG signal in each channel used in our database is 10 minutes. Therefore, each channel of the signal is segmented into 10 non-overlapping one-minute epochs. Figure 3.11 illustrates examples of two 1-minute non-overlapping epochs.

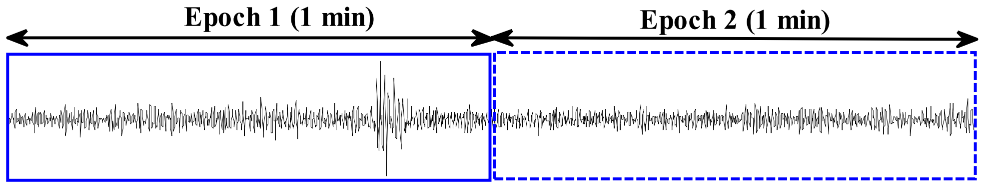

Figure 3.11 Two one-minute non-overlapping epoch.

Using Equation (3.5), the STLL energy is computed for each one-minute epoch. Figure 3.12 shows the 300 ms segment selected from one epoch (Figure 3.12A) and its counterpart for the STLL energy (Figure 3.12B).

Empirical cumulative distribution function (ECDF) of the line length values for each one minute epoch is computed and 97.5% of this value is selected as the threshold (δ_{STLL}) for the given epoch. As stated earlier, δ_{STLL} is selected for every one-minute epoch yielding epoch-specific detection threshold (δ_{STLL}). Figure 3.13 shows the ECDF of the STLL energy for one epoch. δ_{STLL} corresponds to the 97.5 percentile of the STLL energy of the epoch shown with the black arrow.

To detect HFO events, STLL energy of the epoch is compared to the epoch threshold (δ_{STLL}). Those segments with the energy greater than the threshold for at least consecutive 12 ms are selected as HFO events and marked by their start-time and end-time as shown in Figure 3.14.

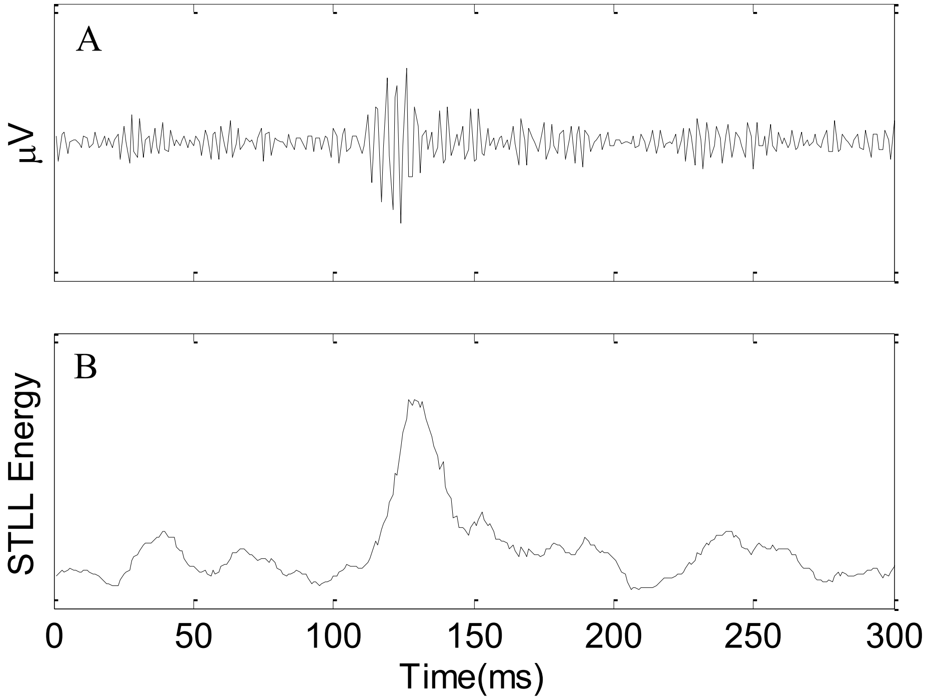

Figure 3.12 **(A)** 300 ms segment of one epoch **(B)** STLL energy of the segment

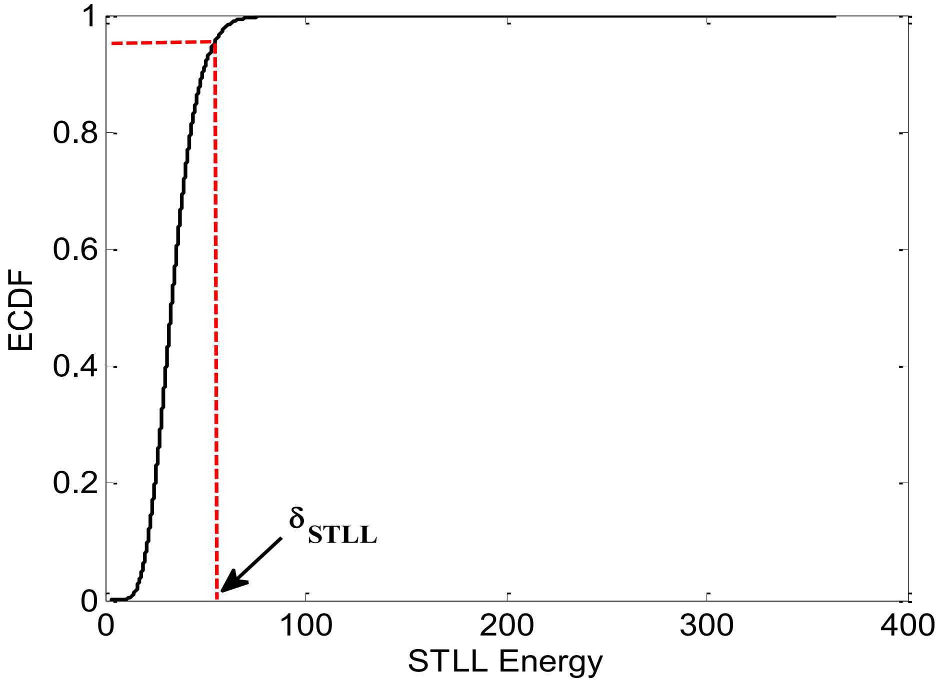

Figure 3.13 Empirical cumulative distribution function (ECDF) of STLL energy for one epoch. Dashed red line defines the threshold (δ_{STLL}) for the epoch which corresponds to 97.5 percentile of the STLL energy.

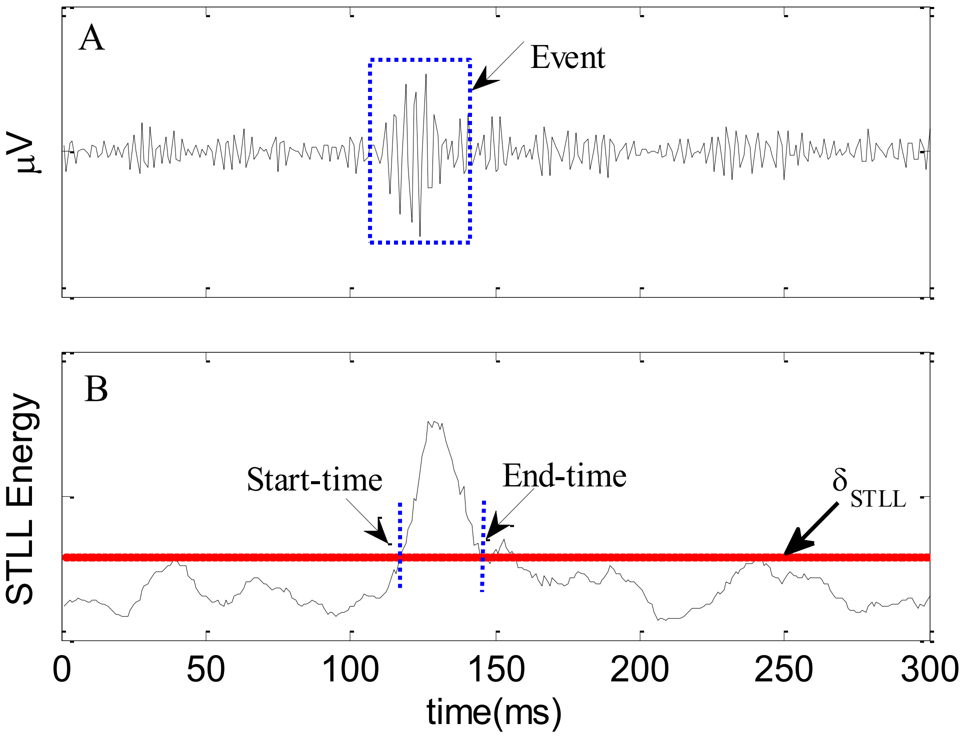

Figure 3.14 Detection of an event (HFO) with the STLL detector. **(A)** 300 ms segment of EEG signal, blue dashed box indicates the event. **(B)** Corresponding STLL energy of the segment. Red line identifies the δ_{STLL} , and blue dashed lines identify the short-time and end-time of the event.

3.2.2 RMS detector

RMS method is based on the moving average of the root mean square of the signal. In the work of Staba *et al* [26], the energy of the band-pass filtered signal (100-500 Hz) was computed over the entire length of the signal (10 minutes) and the threshold was defined by following equation:

$$\delta_{RMS} = \mu_{EEG} + 5\,\sigma_{EEG} \tag{3.6}$$

where δ_{RMS} is the detection threshold, σ_{EEG} is the standard deviation and μ_{EEG} is the mean of the RMS energy of the complete EEG (10 minutes in their research).

In the original RMS method, the data was sampled at 10 KHz, while the data in our work is sampled at 1 KHz. As for STLL method, the differences in the data collection strategies required some modifications to this method to be applicable for our data. First, instead of the band-pass filter (100-500 Hz) in the original work, here we use a high-pass filter with a cut-off frequency of 100 Hz. The reason for that is the difference between the sampling frequencies. As already pointed out, the data in our case is sampled at 1000 Hz, since we use the same bandwidth for the HFOs that has been used in the original work by Staba *et al* [26] (100-500 Hz), a high-pass filter with cut-off frequency 100 Hz is required to keep the frequencies in the range of 100 and 500 Hz (the data is already limited to 500 Hz). Second, Because of the differences in the frequency content of the duration of each cycle, the 3-ms sliding window in the original work is replaced by the 30 ms sliding window. Table 3.2 summarizes the required modifications to the original method.

Table 3.2 Parameters in original RMS method and modified RMS. Column two indicates the parameters values that are used in the original RMS detector and the third column lists the parameters modified to be able to implement in RMS method for our data.

Parameters	RMS (*Staba*)	Modified RMS	Rationale
Filter (cut-off frequency)	BPF ($100 < F_c < 500$ Hz)	HPF $F_c = 100$ Hz	Distinct sampling rate used in data acquisition (10 KHz vs. 1 KHz)
Sliding RMS window length	3 ms	30 ms	Differences in the frequency content of the duration of each cycle

To implement the modified RMS method, as in the case of the modified STLL detector, the EEG should be first high-pass filtered. Pre-processing stage is applied to remove the high-energy low-frequency contents of the signal. A sliding window of 30 ms with a step size of 1 ms (29 ms overlap) is used to process the filtered signal as shown in Figure 3.15.

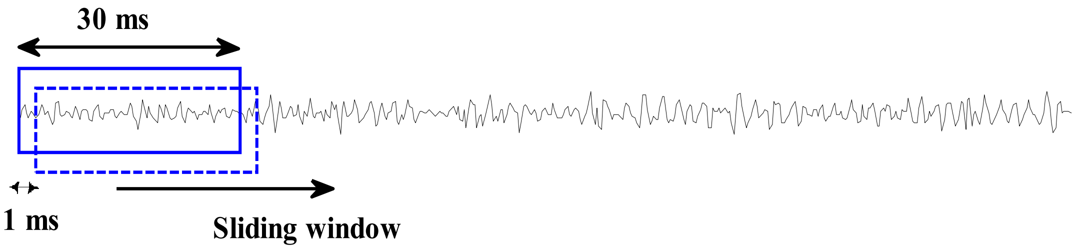

Figure 3.15 Sliding window with the length of 30 ms is used to calculate the RMS value.

The root mean square of the filtered signal is calculated for each window by the following equation:

$$E(t) = \sqrt{\frac{1}{N} \sum_{k=t-N+1}^{t} x^2(k)} \tag{3.7}$$

where $x(t)$ is the filtered signal and N is the number of samples in the sliding window that is set to 30. Figure 3.16 shows the RMS energy for a 300 ms segment of the signal.

Statistical parameters including the mean and standard deviation are computed from the energy function $E(t)$ for each window. In accordance, the detection threshold (δ_{RMS}) is selected (Equation (3.6)). The RMS energies of the signal are subsequently compared with the detection threshold and the segments with the RMS energy greater than δ_{RMS} are detected as HFO events and are marked by their start-time and end-time as shown in the Figure 3.17. Red line indicates the detection threshold computed from the RMS energy of the entire length of signal (10 minutes in this study) and dashed blue lines indicate the start-time and end-time of the detected event.

As stated in Chapter 2, the number of peaks in the rectified band-pass filtered signal (above 0 μV) of the candidate events are counted in the post-processing stage. Each candidate event must have at least six peaks with amplitude greater than 3 SD from the mean baseline signal to be retained as a valid HFO event; otherwise it is rejected. During the development of this technique, we found out that the performance of this detector drastically decreases if the post-processing step described in Chapter 2 is implemented. Therefore, in contrast to the original method, we do not implement any post processing. RMS method is a batch processing algorithm - that is, all the data must be available before this method can be applied.

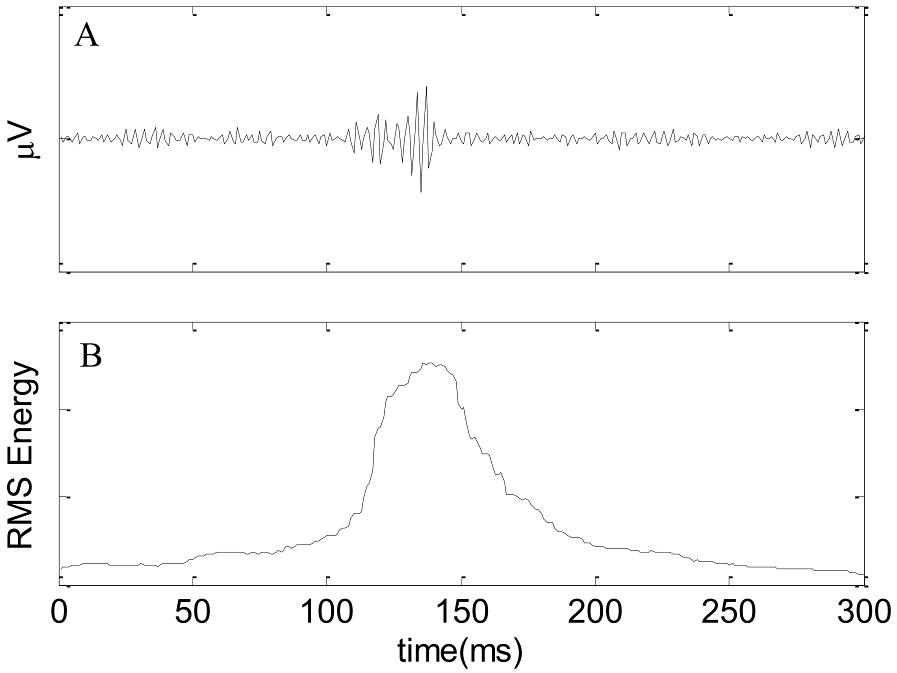

Figure 3.16 **(A)** 300 ms segment of one epoch **(B)** RMS energy of the segment.

As discussed in the previous chapters, in epileptic patients, electrodes remain implanted for a duration of two to three weeks and a large amount of data is recorded, so batch processing is not a suitable scheme for the event detection. Moreover the EEG is a non-stationary signal, i.e., the background changes constantly with the brain state changes. The signal may rapidly change its properties as a function of time. The presence of artifacts or strong events in some part of the data influences the background signal and affects the threshold which can accordingly decrease the performance of the detector.

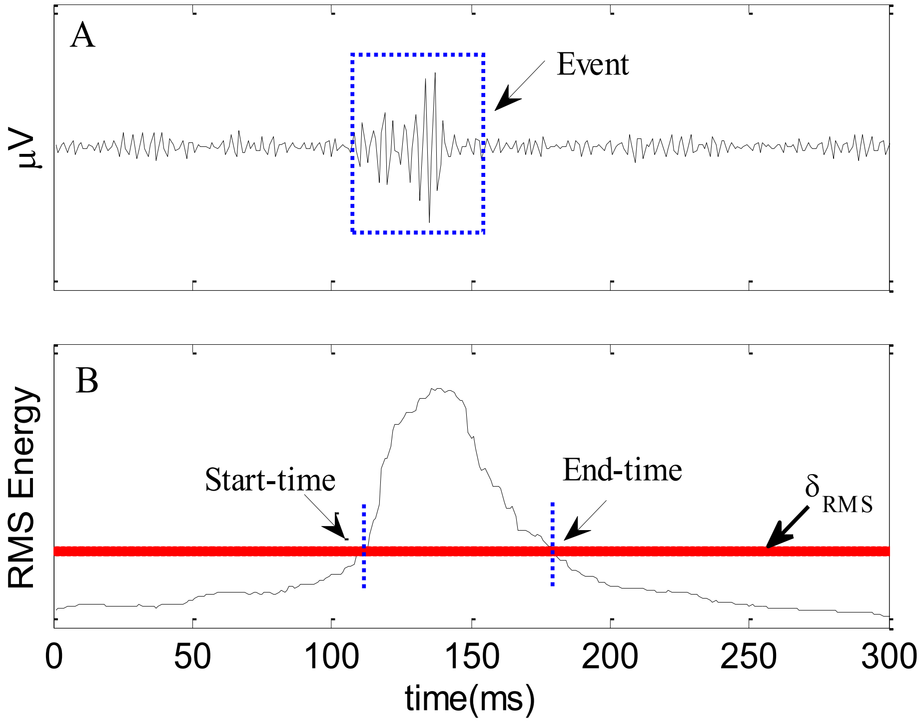

Figure 3.17 Detection of an event (HFO) with the RMS detector. **(A)** 300 ms segment of EEG signal, blue dashed box indicates the event. **(B)** Corresponding RMS energy of the segment. Red line identifies the δ_{STLL} , and blue dashed lines identify the short-time and end-time of event.

We experienced this problem while implementing the RMS method. In one of the datasets in our database, there was a strong transient artifact with an amplitude of almost 20 times greater than its surrounding background (See Figure 3.18). Although the duration of this artifact was limited to 300 ms, computing the detection threshold (δ_{RMS}) for the entire length of the signal resulted in an extremely high δ_{RMS}. Subsequently, large numbers of events could not be detected resulting in a poor performance of the detector. Figure 3.18 illustrates the impact of the spike-like noise on the detection. Although this is one example, such transient fluctuations or spikes occur to some degree throughout the recording.

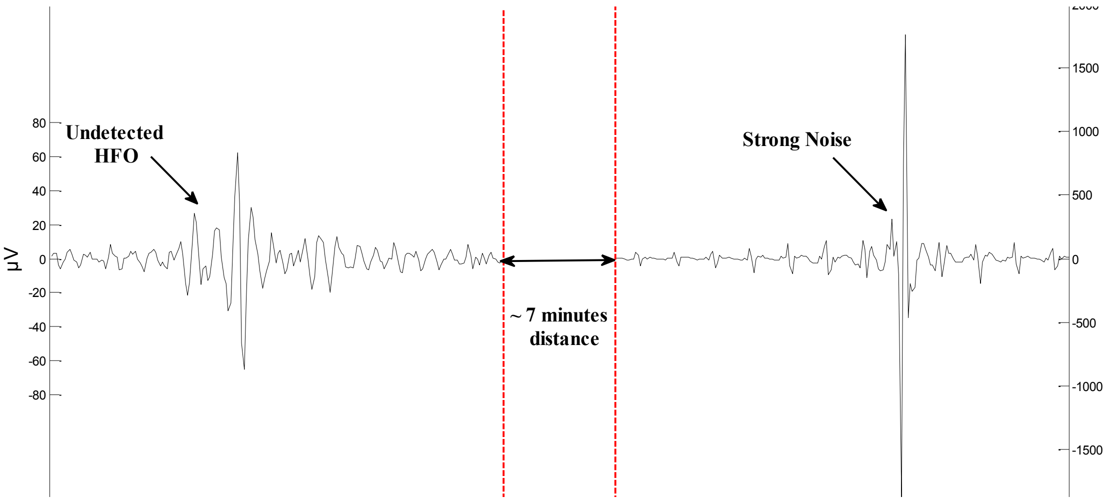

Figure 3.18 An event that wasn't detected with RMS detector. The strong noise (right) located in the signal increases the threshold value and affect on the detection of other events.

Hence with significant experimentation, we addressed such problems for real time detection of HFOs. This resulted in the introduction of two modified versions of the RMS method that we refer to as MS1 and MS2 methods, and these are described below.

3.3 Modified versions of RMS detector

3.3.1 MS1 detector

As described in Chapter 1, the duration of HFOs are limited to several milliseconds (12 – 120 ms) with the rate of occurrences of 0.4 to 80 per minute. Total duration of HFOs is still a small fraction of one minute epoch and the mostly background EEG in each one minute epoch should provide a reasonable estimate of the detection threshold for the considered epoch. Having this in mind, we decided to shorten the epoch length used in the original RMS method and define a modified version of the method that is referred to as MS1.

In the *MS1* method, after high-pass filtering, each channel is divided into distinct epochs of one minute. Root mean square of the high-pass filtered signal is computed. In developing this method, we experimented with various detection thresholds and compared the detection performances of this detector. We observed that reducing the detection threshold significantly improves the performance of the detector. Consequently, we modified the threshold as:

$$\delta_{epoch}(i) = \mu_{epoch}(i) + 3\,\sigma_{epoch}(i) \quad i = 1,2,\dots,K \tag{3.8}$$

where K corresponds to the number of epochs of EEG signal (10 for 10 minutes data), $\delta_{epoch}(i)$ is the detection threshold, $\sigma_{epoch}(i)$ is the standard deviation, and $\mu_{epoch}(i)$ is the mean of the RMS energy of ith epoch. Therefore, each epoch has a distinct threshold instead of a global threshold. Figure 3.19 shows the 10 different thresholds for a 10 minute EEG signal. It is seen that the detection threshold varies across whole length of signal. The detection threshold for each epoch is selected based on the EEG background activities and energy of the HFO events. That is, the epochs with less number of HFO events or without any noises or high energy interferences have smaller detection thresholds, whereas epochs with large amount of HFO events, artifacts, or strong interferences result in larger thresholds. For example, if the presence of high energy artifacts or interferences increases the detection threshold for one epoch, it does not affect the rest of epochs.

Consequently, in the final step, the RMS energy in the ith epoch is compared to the $\delta_{epoch}(i)$, and as in the RMS method, the segments of the signal with the RMS energy greater than δ_{epoch} for at least T ms (T=12 ms) are identified as HFO events.

Final HFO events are marked by their start-time and end-time. The flow chart given in Figure 3.21 provides the procedures used in this method. Figure 3.20 shows an example of an HFO event detected by MS1 detector that was not detected by the original RMS method.

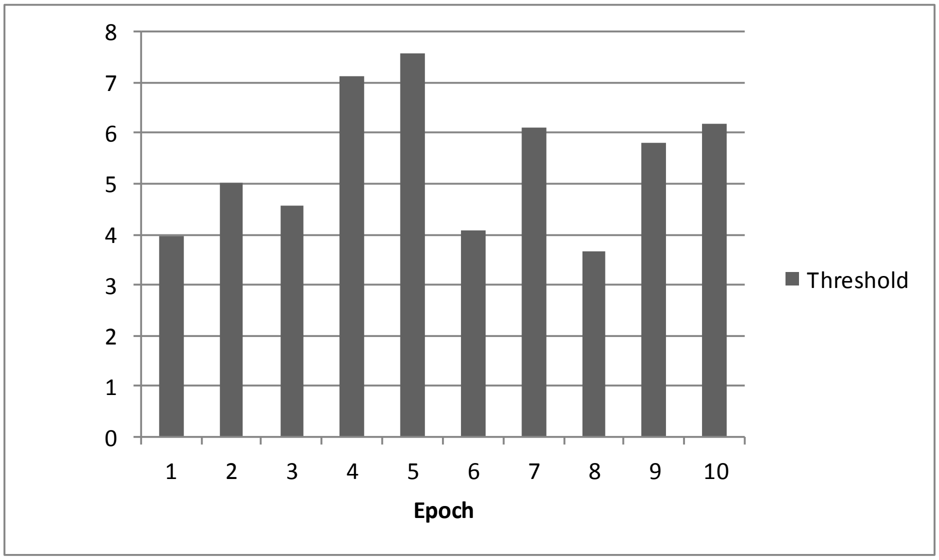

Figure 3.19 Different detection thresholds obtained for 10 non-overlapping epochs.

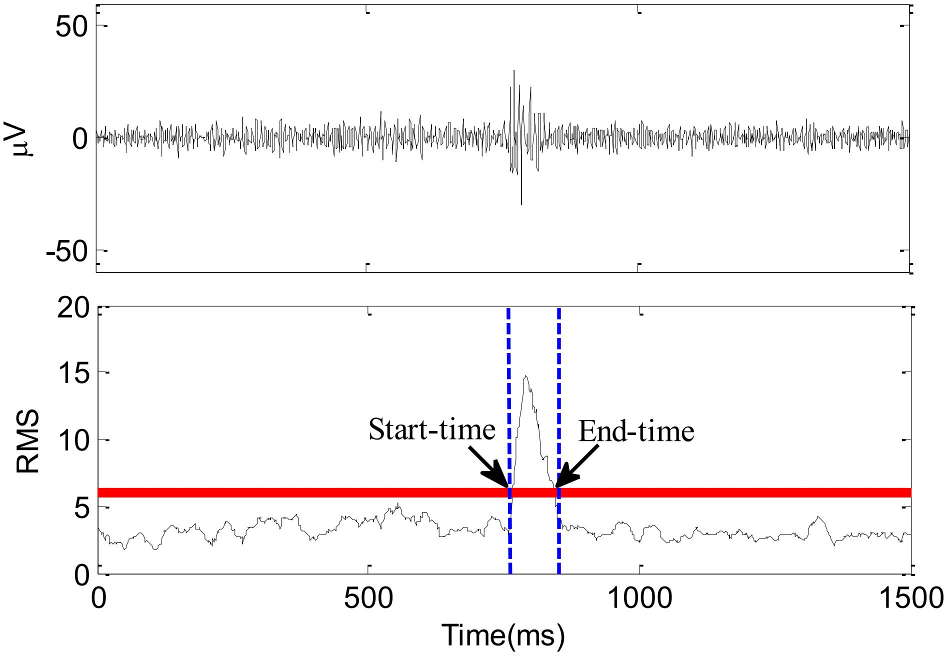

Figure 3.20 Detected event with MS1 detector. **(Top)** Small segment of EEG signal.**(Bottom)** Root mean square energy. Red line shows the detection threshold and dashed blue lines indicate the start-time and end-time of the event.

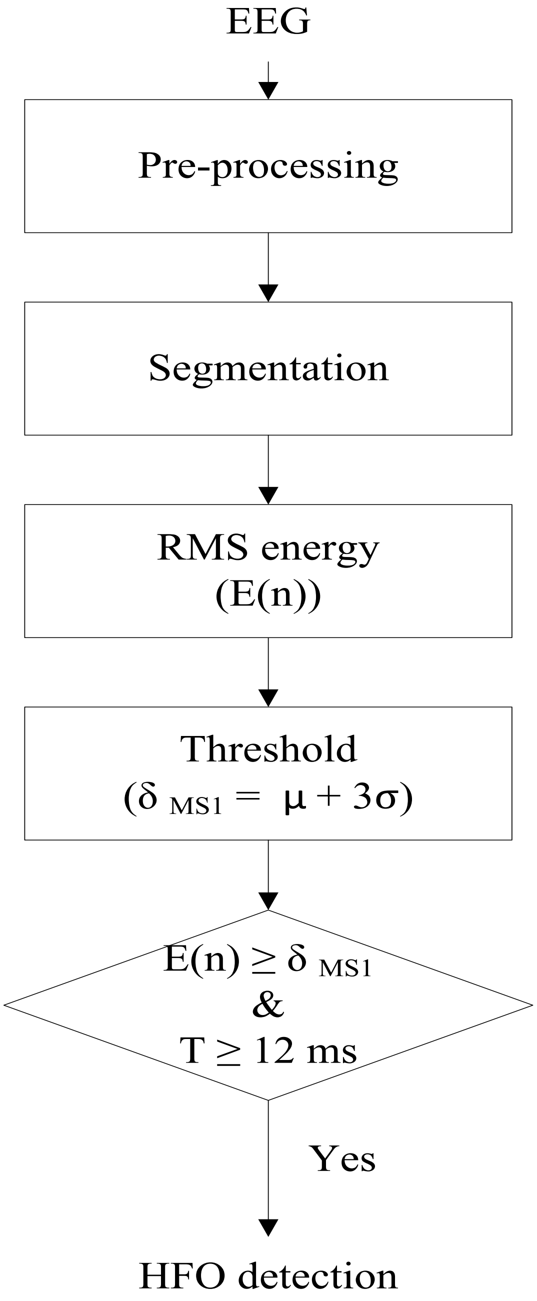

Figure 3.21 Diagram of the MS1 detector. E: root mean square value, T: minimum event duration.

3.3.2 MS2 detector

Although compared to the RMS detector, the data in MS1 method is segmented into smaller epochs, this detector can still be considered as a batch processing method. That is, one minute data must be available so that the MS1 can generate the detection threshold and discriminate between HFO and non-HFO segments. This can be considered as one of the disadvantages of the MS1 detector. To address this problem, we develop an HFO detector which processes the EEG data with a more real-time approach.

To accomplish this idea, we must update the detection threshold as the new data is recorded. However, the epoch length must be long enough so that the detection threshold adequately represents the current EEG background. Therefore, in this approach, the non-overlapping window of the MS1 detector is replaced by a sliding overlapping window for segmenting the EEG signal. The sliding window is characterized by the length of the window denoted by *L*, and the step size of the window denoted by *D*. The length *L* defines the number of samples that are used to compute the energy function before the window slides by *D*.

Figure 3.22 illustrates the sliding window used for MS2 detector.

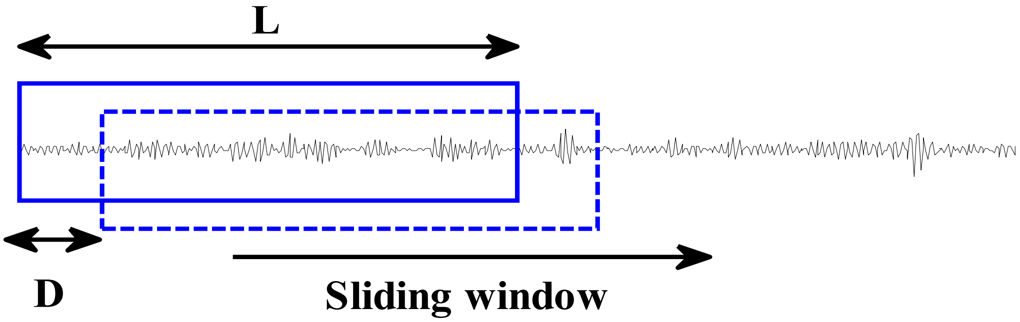

Figure 3.22 An example of selecting epochs in MS2 detector. D = 10 second, L = 10 minute.

The root mean square energy of each window is then computed using equation

$$E_{MS2}(k) = \sqrt{\frac{1}{L}\sum_{i=1+(k-1)D}^{D(k-1)+L} x^2(i)} \qquad , 1 \le k \le K \tag{3.9}$$

where E_{MS2} is the root mean square energy of the filtered EEG signal $x(t)$, i is the index that controls the displacement inside the sliding window, and k is the index that indicates the start of the next window.

The RMS energy of L samples in each window is computed and a detection threshold ($\delta_{MS2}(k)$) is computed. If the total length of signal contains N samples, then the total number of detection thresholds, δ_{MS2} , is defined by equation:

$$K = \frac{N-L}{D} + 1 \tag{3.10}$$

In this study, we use the same epoch length as that used for MS1 detector. So L is set to one minute or equivalently 60000 samples for a sampling rate of 1000 Hz. After considerable experimentation, we set the step size D to 10 seconds (10000 samples in this study). The reason for this selection is that 10 sec is short enough to be considered as a real-time approach and still long enough so that the detection thresholds adequately represent the background EEG. Setting L and D to 10 minutes and 10 seconds, respectively, K in this study equals 55. That is, 55 different windows with length L are used to compute the energy of the signal. Similar to MS1 detector, E_{MS2} of each epoch is compared to the detection threshold $\delta_{MS2}(k)$ for the given epoch, defined by Equation (3.8), and those segments exceeding the threshold for a minimum duration of time ($d_{min} = 12\ ms$) are considered as HFO events and marked by their start time and end time.

In both *MS1* and *MS2* methods, instead of using the complete length of the data, thresholds are computed in a per-epoch fashion which varies for each epoch. It means that although the presence of noise or any other artifacts may still increase the threshold in a given epoch, it will not affect the complete recording. As a result, the number of false negative detections is remarkably reduced in *MS1* and *MS2* methods compared to that of the original *RMS* method.

3.4 Proposed HFO detection schemes

As described earlier, HFOs are field potential rhythmic oscillations in the range of 100-500 Hz consisting at least four oscillations that can be distinguished from the background. In general, they are differentiable from background activity if they have high amplitude or they have low amplitude but rhythmic enough to be considered as HFOs (faster in frequency). High amplitude HFO events are easily detected by most of the automatic HFO detectors; however, these methods often fail to detect the short-duration low-amplitude HFO events. Moreover, these methods suffer from common pitfalls of failing to exclude many high-amplitude sharp spindles, such as spikes and sharp waves. To improve the detection performance of the automatic HFO detectors, this problem needs to be addressed.

In our initial investigation of various HFOs events, we discovered that these events present themselves with increased slope (m) of the half-waves (described later) which could be due to either higher amplitude or short duration waves (i.e. faster activities). The slopes of the half-waves can be used as a metric to describe the sharpness of the EEG during HFO events. Sharpness feature for EEG signal analysis has been already applied in spike detection [71-75]. Utilizing this sharpness characteristic of the EEG signal, we aim to design new automatic HFOs detectors.

In the following sections, a brief discussion on how HFOs affect the slope characteristic of a signal will be presented. The material presented in this section is used as a basic building block for the proposed automatic HFOs detectors to be discussed later in this section.

3.4.1 Basic Principles - Background

In this work, a "wave" is defined as a set of two half-waves that are adjacent and of opposite directions and can be simply modeled by a triangular waveform (2 half-waves, Figure 3.23). Half-wave (HW) is the section between two consecutive extrema (maximum and minimum) of signal amplitude. The slope of a half-wave is a function of the amplitude and duration and is given by

$$m \propto \frac{A}{d} \tag{3.11}$$

where m is the slope, A is the amplitude (changes in the vertical axis) and d is the duration (changes in the horizontal axis) between the two points on a straight line as described in Figure 3.23. As can be seen from Figure 3.23, the left side of the triangular wave (left half-wave) has a slope of m_1 which is quickly followed by another line with slope m_2 with an opposite sign.

To detect the extrema, every sample of signal is subtracted from the preceding sample – first order difference equation is applied to the EEG signal, $x(t)$:

$$\mathrm{x_{diff}(n) = x(n) - x(n-1)} \tag{3.12}$$

If the sign of $\mathrm{x_{diff}}$ changes from one polarity to the other, the sample (x(n)) is considered as an extremum (shown in green diamonds in Figure 3.24). Hence, a half-wave includes only the samples that are successively increasing or decreasing, i.e., slopes that are either positive or negative.

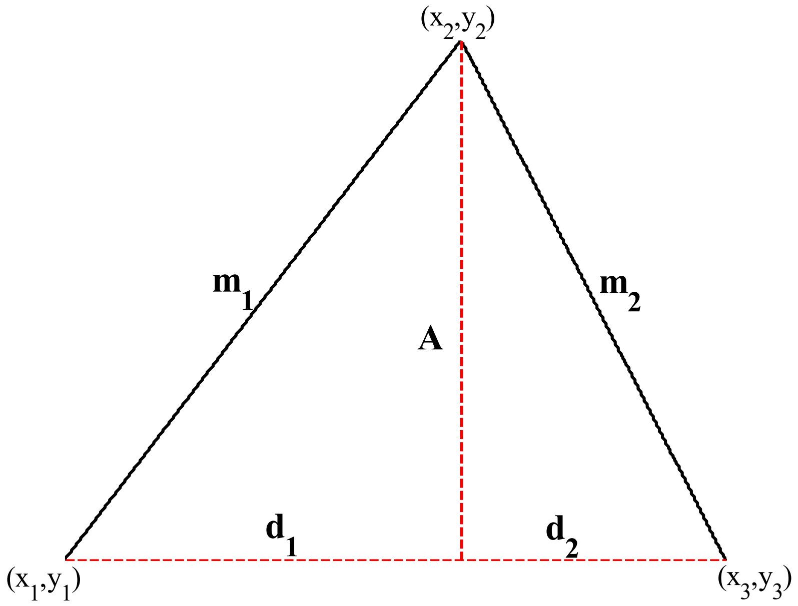

Figure 3.23 An example of a wave model, $m_2 \propto \frac{A}{d_2}$, $m_2 \propto \frac{A}{d_2}$

A given signal consists of waves. In the case of pure sinusoid, each cycle represents one wave that can be broken up into two half-waves (positive and negative directions). Figure 3.24 shows an example of two cycles of a sinusoid. Dashed blue lines illustrate the start and end of each of waves and the red lines are used to demonstrate the similarity between a triangle and a wave. The extrema are shown with green diamonds.

The goal is to estimate the slope of each half-wave. To do so, each half-wave is fitted to a linear regression model. We define the "*sharpness"* of half-wave (SHW) feature as a measure of the slope of the best fitted straight line to half-waves.

In this study, least square method is applied to fit a straight line to the data of each half-wave. An example of a model of a straight line with the slope value m and intercept b is given by the following equation:

$$f(x) = mx + b \tag{3.13}$$

Details of calculation of the intercept and sharpness are given in the Appendix.

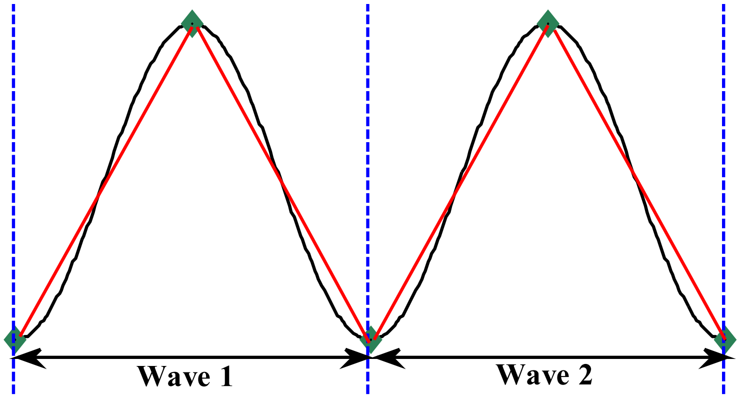

Figure 3.24 An example of wave. Blue dashed lines are used to show wave. Each red line is a HW of a triangle .Green diamonds show the extrema.

Figure 3.25 shows the best fitted straight lines for half-waves of a sinusoid as dashed blue lines.

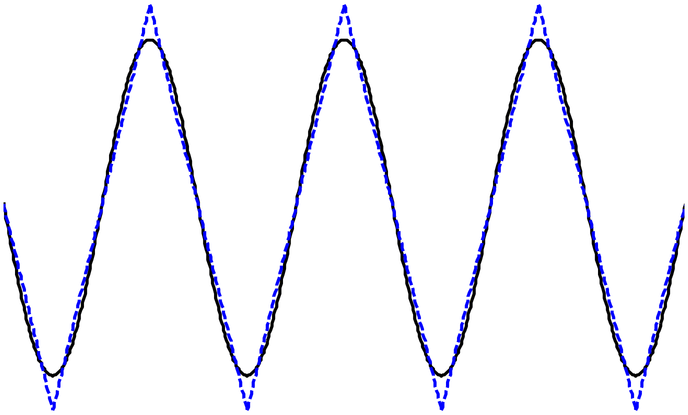

Figure 3.25 Linear regression model is used to model HWs of a sinusoid. Dashed blue lines show the modeled straight lines for HWs.

Figure 3.26 illustrates four oscillations of a simple rhythmic signal at 400 Hz. One oscillation (cycle) of the signal is shown between vertical dashed red lines. The dashed blue lines show the best fitted straight line for each half-wave. Note that in the simple rhythmic signal of Figure 3.26, all the waves are identical and the SHWs are almost equal (regardless of the upward or downward swing of the half-wave). However, in real data this is not typically the case and the sharpness is likely to be different for the two half-waves of each oscillation. Figure 3.27 provides examples of best fitted straight lines for HWs in real EEG data.

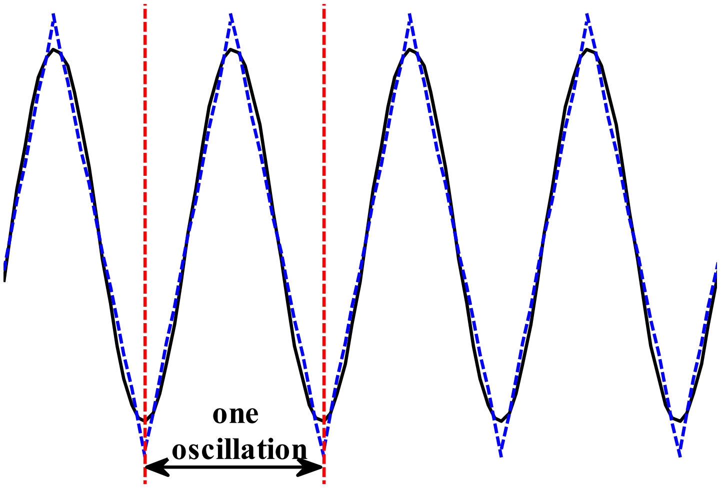

Figure 3.26 A simple rhythmic activity sinusoid simulating HFO with 4 oscillations. Red dashed lines indicate the boundaries of an oscillation (wave). Blue dashed line shows the best fitted line for HWs.

One of the difficulties in this work is to find proper HWs. The algorithms to do this have their inherent problems. In this study, since we are interested in detecting fast activities regardless of being short or high in amplitudes, we do not merge small fluctuations in the signals and consider each and every short segment as a half-wave if the polarity changes from being positive to negative or vice versa. Short HWs are seen in the magnified window in Figure 3.27.

One common property of all HFOs can be the increase in the SHWs. Figure 3.28 illustrates an example of how the SHWs increase in the presence of HFO. Dashed red box in the figure, indicates the boundaries of the event. It can be observed that the SHWs increase as the event starts and they gradually decrease when the event reaches its end-time.

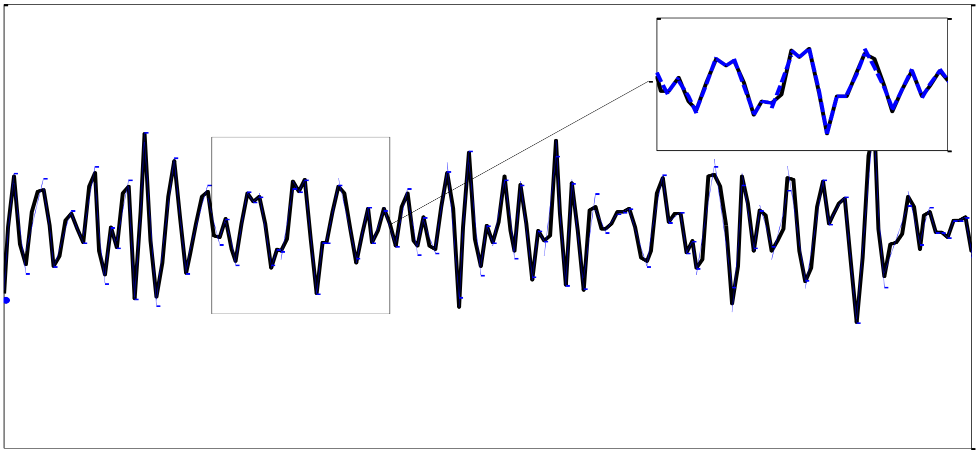

Figure 3.27 Real EEG data. HWs are modeled with least square method. Blue dashed lines indicate the best fitted straight lines for HWs.

As stated in previous chapters, each HFO event is composed of at least four oscillations (wave, in this study). That is, in each HFO, there are at least 8 HWs in a cluster with higher slopes compared to background EEG. As a result, if the sharpness of at least 8 adjacently located half-waves exceeds the detection threshold, HFO event can be said to be present in the data. Therefore, by quantifying one unique property of HW (sharpness), it may be possible to develop an automatic HFO event detector with potentially improved system performance over existing schemes.

Based on the above discussion, we utilize the sharpness of half-waves to develop automatic HFOs detectors. Following paragraphs provide details of three proposed detectors termed as *"Slope"*, *"Iterative Slope"*, and "*Slope-causal"*, which have been designed based on the SHW property of the EEG signals.

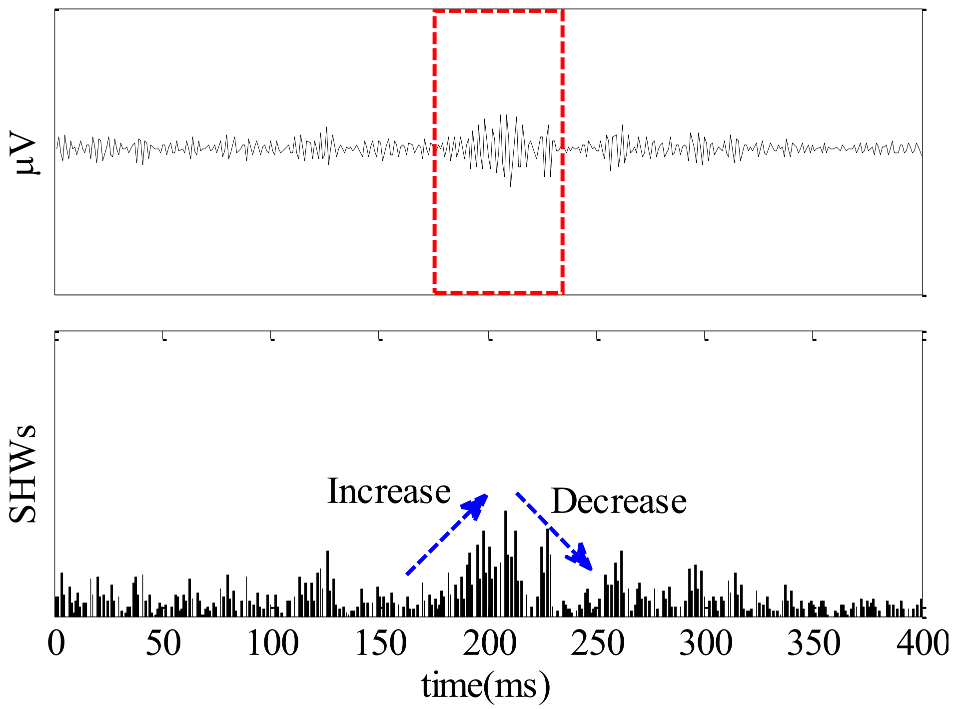

Figure 3.28 SHWs are increased once the HFO appears. **(Top)** High pass filtered signal. **(Bottom)** SHWs of the signal. Dashed red box indicates one HFO event.

3.4.2 Slope detector

Applying the sharpness of the half-waves in the EEG, we develop an automatic HFO event detector. The flowchart of the proposed method is shown in Figure 3.29.

The pre-processing block consists of a high-pass filter and an artifact rejection module. As mentioned in the pre-processing section, high-pass and notch filters are applied to remove the high-energy low frequency contents and power-line harmonics. Once the EEG is conditioned by the preprocessing step, the signal is segmented into short epochs. In the initial development of this method, we applied the same epoch length that was used for the MS1 method. Therefore, as for the MS1 detector, the 10 minute EEG signal was divided into ten distinct one minute non-overlapping epochs as shown in Figure 3.11. We refer to this method as the "*Slope*" method.

As described in the Section 3.4.1, to develop an automatic HFO detector based on the sharpness feature, EEG signal must be decomposed into a series of half-waves. By applying the procedures from that section, EEG signal of each epoch is divided into half-waves. Each half-wave is then modeled by a best-fit straight line in the least square sense to estimate the sharpness. Since the sign of the HW slopes does not play a role in identifying the sharpness feature, the absolute value of the slopes of HWs is computed as sub-segment steps. To identify the onset (start-time) and the offset (end-time) of an HFO event, the detection threshold (δ_{slope}) should be selected. Clearly, the proper choice of the threshold is the most important factor in the performance of the automatic HFO detector. Providing a reasonable estimate for the threshold in EEG signals increases the performance of the algorithm. As we know, various values have been reported for the amplitude of HFO events in the literature (See Table 1.2). Moreover, since the EEG signals are non-stationary, a fixed or given detection threshold may not be valid for all times or across all patients. Due to the above reasons, selection of a static threshold for EEG signals would result in poor detection sensitivity and specificity. Therefore, in the proposed methods, as for the STLL detector, the detection threshold is chosen as a percentage of the empirical cumulative distribution function (ECDF) of the sharpness of the HWs for each corresponding one-minute epoch. This selection allows us to have a detection threshold that dynamically changes along with the EEG signal properties of the epoch. That is, if one epoch includes continuous high frequency activities (without sufficient background), the detection threshold is higher compared to an epoch with sufficient background.

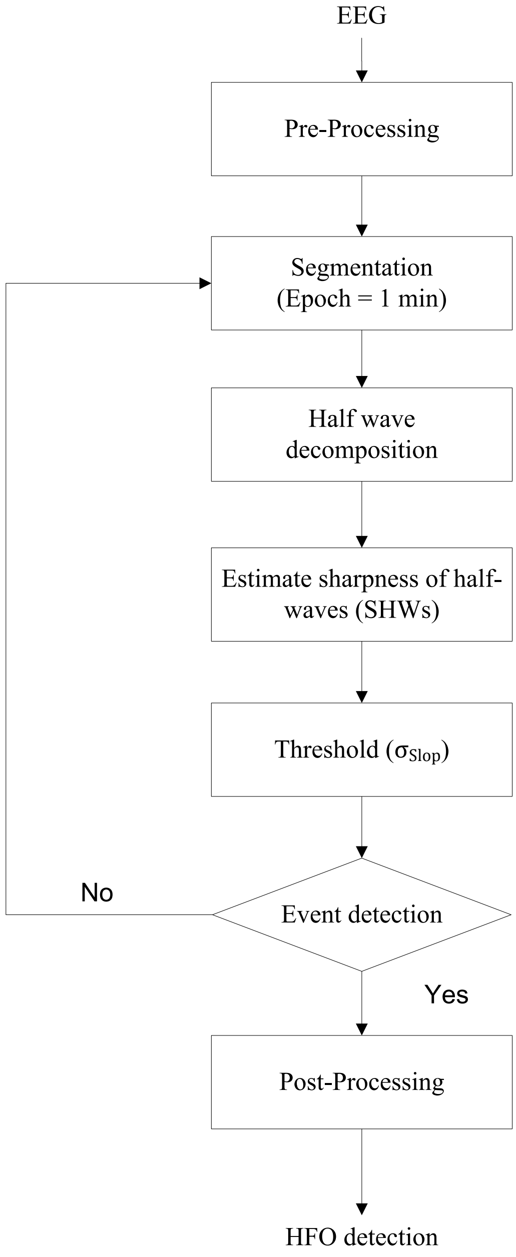

Figure 3.29 Block diagram of Slope method.

The optimal detection threshold (δ_{Slope}) is determined from the ROC analysis (discussed further in Chapter 4). The absolute values of the slopes of the half-waves are then compared with the epoch threshold δ_{Slope} and all half-waves with sharpness of less than $\delta_{Slope}(epoch)$ are rejected and not considered any further.

$$g(n) = \begin{cases} |SHW| & for\ |SHW| \geq \delta_{Slope}(epoch) \\ 0 & Otherwise \end{cases}$$

where $\delta_{Slope}(epoch)$ is the epoch threshold to identify the SHWs that may correspond to HFO events.

As discussed earlier, each HFO event includes at least 4 consecutive waves or equivalently 8 HWs, with sharpness higher than the background. Therefore, to detect an HFO event, at least 8 consecutive half-waves must have slopes or sharpness features greater than the corresponding $\delta_{Slope}(epoch)$.

In the final step, the detected event is examined to determine whether it satisfies the minimum duration (D_{TH}) criterion. If so, the valid HFO event is marked as an event. If not, it is rejected.

The Slope method is able to detect fast activities in the signal regardless of the amplitude; however, based on the studies in the literature, the HFO events should be discernible from the background. Therefore, to remove the probable low energy detected HFO events, post processing step is applied. In the post-processing step, relative energy of the detected events is compared to the energy of its 500 ms surrounding background (500 ms). If the relative energy of the events (Equation (3.14)) is at least 8 dB greater than that of surrounding background, the event is saved, otherwise, it is rejected. The relative energy of 8 dB was selected empirically based on the HFO events scored visually.

$$RE = 10 \times log_{10} \frac{E_{event}}{E_{Bg}} \tag{3.14}$$

where E_{event} and E_{Bg} correspond to energy of HFO event and energy of background respectively.

Figure 3.30 shows an example of an event detected by the Slope detector. As can be seen, after setting the threshold, SHWs less than $\delta_{Slope}(epoch)$ are discarded while those greater than $\delta_{Slope}(epoch)$ remain.

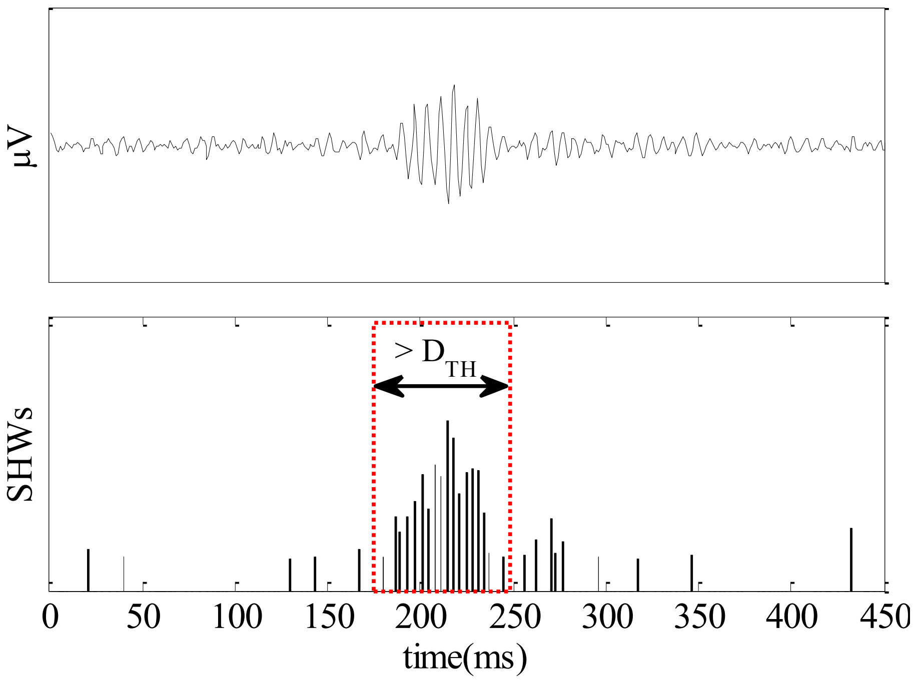

Figure 3.30 An HFO event detected by Slope method. Red dots shows the cluster of SHWs with the amplitude greater than threshold.

The red dotted box shows the cluster of SHWs that exceed the detection threshold. There are more than 8 consecutive SHWs greater than the threshold. Duration of the event is longer than the minimum duration (12 ms in this study). Since the relative energy of the event exceeds 8 dB, it is marked as an HFO event.

3.4.3 Iterative-Slope detector

In the Slope detector, the length of each epoch was set as one minute and different thresholds were computed for each channel and each epoch. One of the drawbacks of the Slope detector is that it fails to detect some events that occur in clusters. To address this, we tried to follow the method that a neurologist may apply for visual detection of HFOs. For visual detection of HFOs, events are compared to one or two seconds of the localized background EEG rather than a large one minute epoch. Hence, we shortened the length of the epoch used in Slope method and replaced one-minute constant length window by a two second running window with 50% overlap to segment IEEG, as illustrated in Figure 3.31.

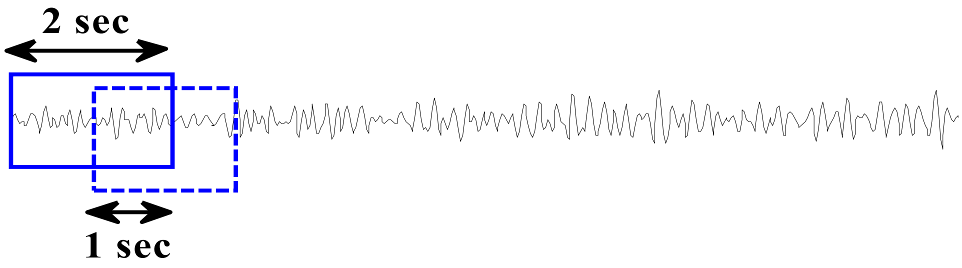

Figure 3.31 Sliding window used for Iterative Slope method.

Our justification for selecting shorter epochs is that they may provide a more reasonable estimate of the local background that might lead to an increase in the number of detected events (True positive events). We refer this method to as "*Iterative-Slope*" method. The flowchart of the "*Iterative-Slope*" method is shown in Figure 3.32.

While implementing this method, we discovered that due to the short length of the epoch, the presence of more than one event in each epoch increases the detection threshold. This scenario gets worse when neighboring events do not have identical SNR levels. In this case, the event with lower energy is generally not detected with a high threshold which ultimately affects the detection performance of the method. To handle this scenario, we attempted to develop an iterative threshold calculation. Detection scheme of this method is given as below.

The EEG in 2 second epochs is decomposed into half-waves. As in the case of the Slope method, the sharpness of each half-wave of the epoch is estimated with the least square model. To discriminate between the HFOs from the background, detection threshold is computed in each epoch. The sharpness of half-waves (SHWs) in the epoch are compared to the epoch threshold ($\delta_{Iterative}(epoch)$). The HWs with sharpness smaller than $\delta_{Iterative}(epoch)$ are rejected and those with higher values are retained for event detection. All segments with a cluster of at least 8 half-waves are considered to be valid HFO events and are marked by their onset and offset.

In the next step, the detected events in the epoch are removed and a new detection threshold is computed for the remaining data in the epoch – hence the term "iterative" approach. The detection procedure is repeated on the resulting new epoch to check whether HFO events persist. This procedure repeats until no more events can be detected in the epoch.

3.4.4 Slope-Causal detector

In the "*Slope*" and "*Iterative-Slope*" methods, thresholds are computed for each epoch which includes the background as well as the HFO events. In these two methods, the detection thresholds increase by the presence of events leading to missed HFO detection, thus affecting the performance of the detector.

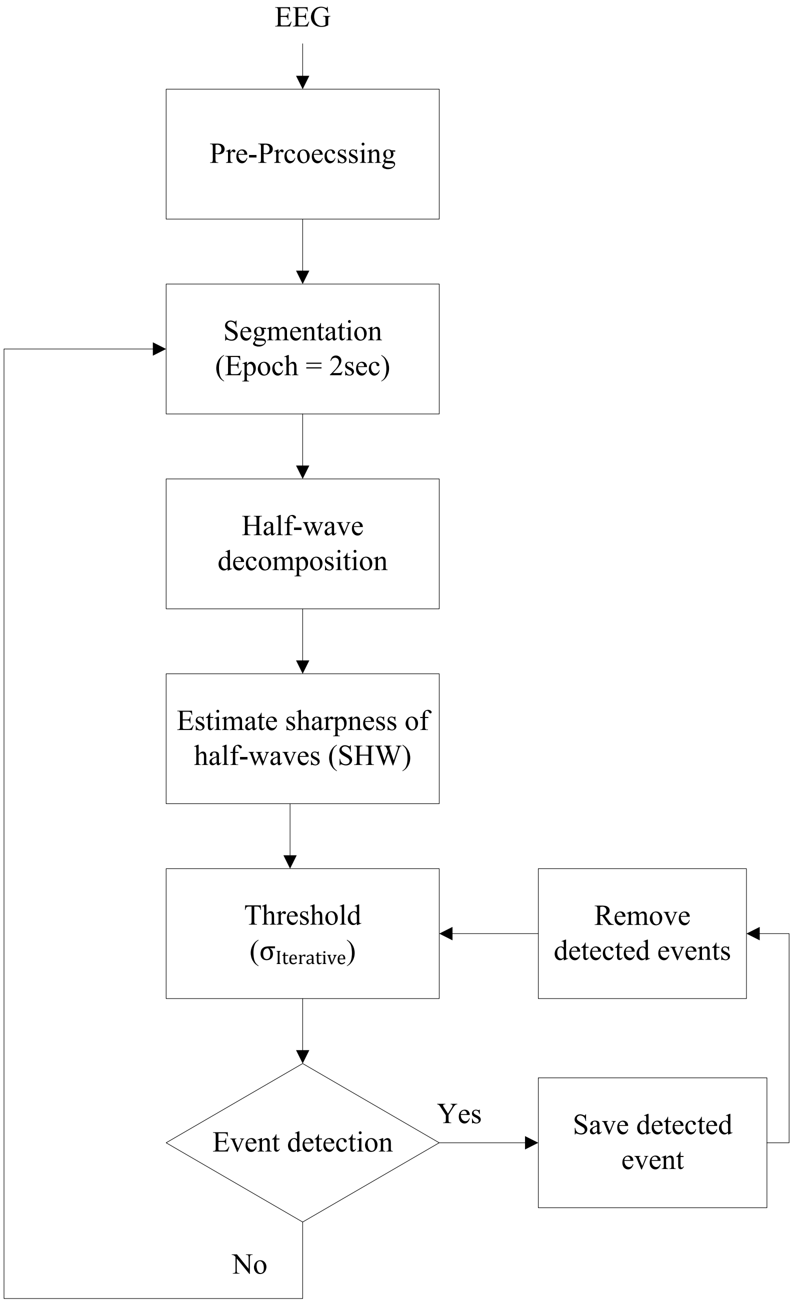

Figure 3.32 Block diagram of Iterative-Slope detector.

Therefore, we decided to implement another method in which the detection threshold is selected only for the background segment (excluding HFOs events). We refer to this method as *Slope-Causal* detector. The term "*causal*" was selected due to the fact that in this method, data is only compared to the previous samples and not to the future ones.

In this case, as shown in Figure 3.33, two different sliding windows are applied: background window and test window. The background window is used to compute the detection threshold, whereas, the test window is applied to detect the HFO events.

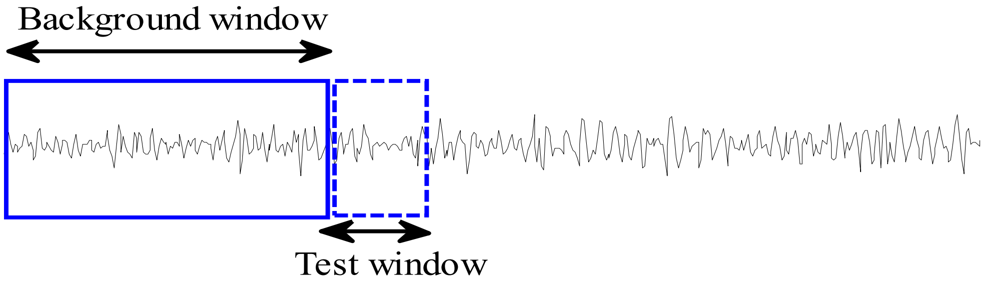

Figure 3.33 Two sliding window for Slop-Causal detector. Solid blue box shows the background window (2 sec), and dashed blue window indicates the test window that is used for HFO detection.

The flowchart of the *Slope-Causal* detector is divided into two parts: Background selection and HFO detection, as shown in Figure 3.34 and Figure 3.35, respectively. Following paragraphs present the details of the procedures corresponding to these two parts.

Background Selection

One of the main difficulties in the *Slope-Causal* method is to find the background window. We must find an approach to differentiate the baseline activities from HFO events. In this context, a baseline activity is defined as EEG segments that are free of HFO events. To find a background segment, we use the results of the *Iterative-Slope* detector. That is, we assume that the *Iterative-Slope* method is capable of discriminating between HFO events and the background signal. Hence, if the *Iterative-Slope* method did not detect an HFO event in an epoch, then the epoch can be considered as a background segment.

The EEG in the epoch is decomposed into a series of half-waves and the sharpness feature and detection threshold are obtained by procedures utilized in the previous sharpness-based detectors. If no HFO events are detected in the epoch, then the epoch is considered as a background window; otherwise, the detected event is saved and the background window moves forward (2 second) to select another epoch. These procedures are repeated until a background epoch is selected (See Figure 3.34). Once the background epoch is chosen, the detection threshold of this epoch (background epoch) is selected as the threshold (δ_{Causal}) which is further used for the test window to detect HFO events.

HFO Detection

Once the background epoch has been selected, the test window is applied to identify HFOs. The test window, as illustrated in Figure 3.35, is a fixed length window that is used to detect HFO events in the EEG signal. This window is used to create an epoch (500 ms in this study) starting from the last sample of the background epoch. Our justification for selecting 500 ms for test window is as follows: based on the literature, we know that the duration of HFO event is limited to 8 – 200 ms (See Table 1.2); therefore, 500 ms provide a sufficient length for locating an HFO event.

To detect HFO events in the test window, following procedures are applied. The data in the test window is broken down into half-waves and sharpness features of half-waves are extracted. The sharpness of half-waves (SHWs) of this epoch is compared to the detection threshold (δ^{i}_{Causal}) that has been computed from the background window at the instant i.

Consequently, the SHWs with smaller value than δ^{i}_{Causal} are removed from further considerations. Similar to the "*Slope*" and "*Iterative-Slope*" detectors, if at least 8 consecutive SHWs in the test window cross the δ_{Causal} , an event is detected. After saving the detected HFO event, the event is removed from the test window and the background window moves forward (500 ms) to update the background and test windows.

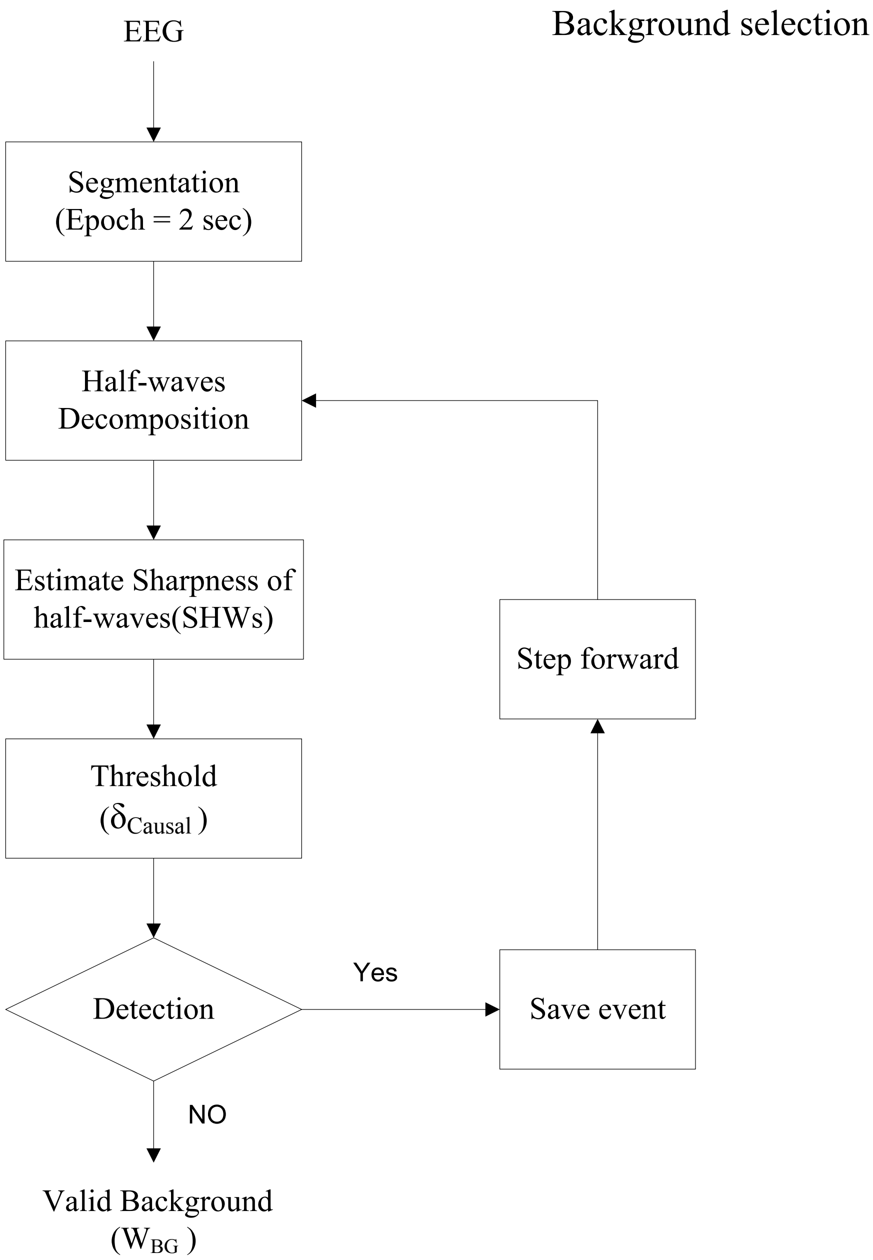

Figure 3.34 Block diagram of the Background selection part of Slope-Causal detector.

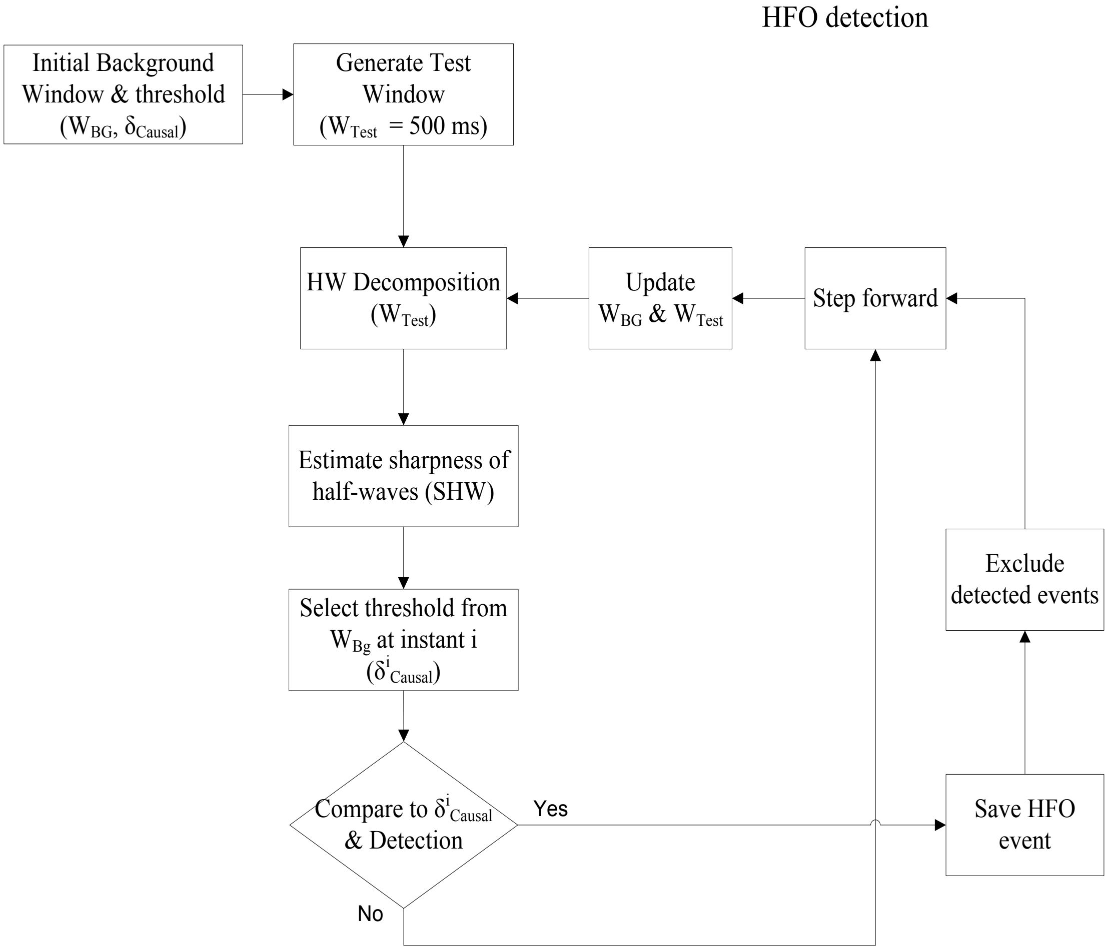

Figure 3.35 Block diagram of the HFO detection part of Slope-Causal detector.

3.5 Summary

In this chapter, we have implemented RMS and STLL detectors. We have also introduced 2 modified versions of RMS method (MS1, MS2). Moreover, we have proposed three new algorithms, namely, "*Slope*", "*Iterative-Slope*" and "Slope-*Causal*", for HFO detection. In the above detectors, RMS, STLL, MS1 and MS2 are based on the energy functions of the EEG signals, while "*Slope*", "*Iterative-Slope*" and "Slope-*Causal*" detectors are based on the sharpness feature of the EEG signals.

The RMS, MS1, and MS2 detectors use the root mean square energy of the signal; however, the segmentation varies from one to another. STLL detector uses the short time line length energy function for HFO detection. All the proposed algorithms track the existence of HFOs with the estimated slopes of the best fitted line of the half-waves termed as sharpness. However, different methods for segmentation were applied.

In the next chapter, we will use simulated EEG data to compare the performance of all the above methods.

Chapter 4 . Performance of the Detectors Using Simulated Signals

In Chapter 3, we proposed three new methods for detecting high frequency oscillations using the sharpness feature as the basic building block. Additionally, we implemented two of the existing methods from the literature, the RMS detector [26] and the STLL detector [55], which are based on the energy function. Moreover, to improve the performance of the RMS detector, we proposed two modified versions, and referred to these as the MS1 and the MS2 detectors.

To assess the detection performance of an automatic HFO detector, its results must be compared with those of visual marking. As discussed earlier, the EEGers are not always unanimous in identifying HFO events and the visual scoring of these events is generally highly subjective. Subsequently, in the real-world setting, it is difficult to assess the performance of a method by simply comparing them with the visually scored events. To objectively assess the performance, we simulated the EEG signals including the background and HFO events to compare the performance of all of the HFO detection methods presented in Chapter 3, independent of human reviewers.

In this chapter, we will describe the simulated EEG background and HFO events and present the performance results of the detection methods described in chapter 3 using this simulated EEG data.

4.1 Simulation

The goal of this study is to compare the performance of the automatic HFO detectors with simulated EEG (background and HFO events). By using the simulated data, we aim to compare the performance of the detectors and to find the detector that gives the best result. The performance of a detector is defined as the ability to identify the simulated HFOs from the background EEG. The performance metrics used to define the performance of the detectors will be defined later (See Section 4.2.1).

An EEG may be regarded as a statistical process with two components: (1) a stochastic component which is stationary over short epochs (quasi-stationary) and (2) transient components (spikes, sharp-waves, and HFO events, for example) that arise sporadically. The transient components, HFOs in this study, are considered to be superimposed on the stationary stochastic component referred to as the “background activity”.

In this study, the background IEEG of one patient is used to model an auto-regressive (AR) model. The resulting AR model is subsequently used to generate the simulated background EEG for the simulation study. HFO events are generated using short bursts of sinusoidal waveforms. The following paragraphs provide details about the simulated data generation.

4.1.1 Background EEG Simulation

The simulation of EEG signals with an AR model was first suggested in the early 70’ by several researchers [76, 77]. The applicability of AR models to the EEG has been verified experimentally as well as theoretically. In this work, we apply an AR model to generate the background activity.

In general, EEG signals are characterized by their power spectral density estimations since they are stochastic signals. Therefore, simulated EEG is generated such that its power spectrum matches the power spectrum of the background human EEG activity.

In AR modeling of signals, each sample of a single-channel EEG measurement is defined to be linearly related with respect to a number of its previous samples. Time-varying AR modeling for non-stationary signals is obtained by the equation

$$\sum_{k=1}^{P} a_k(n)x(n-k) = v(n) \tag{4.1}$$

where a_k are the auto-regression coefficients, $x(n)$ is the series under investigation (real background EEG), and $v(n)$ is the noise which is assumed to be Gaussian white noise.

AR coefficients $a_{1}, a_2, \dots, a_P$ are estimated using the Yule-Walker equation expressed in the compact matrix form by the equation

$$\boldsymbol{w} = \boldsymbol{R}^{-1}\,\boldsymbol{r} \tag{4.2}$$

where $w_k = -a_k$, $\boldsymbol{r}$ is the auto-correlation vector, $\boldsymbol{R}$ is the correlation matrix which is defined by the following equations:

$$\boldsymbol{R} = \begin{bmatrix} r(0) & r(1) & \dots & r(P-1) \\ r^*(1) & r(0) & \dots & r(P-2) \\ \vdots & \vdots & \ddots & \vdots \\ r^*(P-1) & r^*(P-2) & \dots & r(0) \end{bmatrix} \tag{4.3}$$

$$\boldsymbol{r}(-\boldsymbol{k}) = \boldsymbol{r}^*(\boldsymbol{k}) \tag{4.4}$$

In this study, the simulated background EEG is generated using the real IEEG data of one of the patients in our database. Specifically, 10 seconds of the background IEEG from one recording is selected to simulate the background data. Visual inspection ensured that the background EEG is selected such that it does not contain high frequency oscillations, seizure activities, and artifacts. An 8th order AR model [78, 79] is fit to the selected segment to subsequently generate the simulated background EEG.

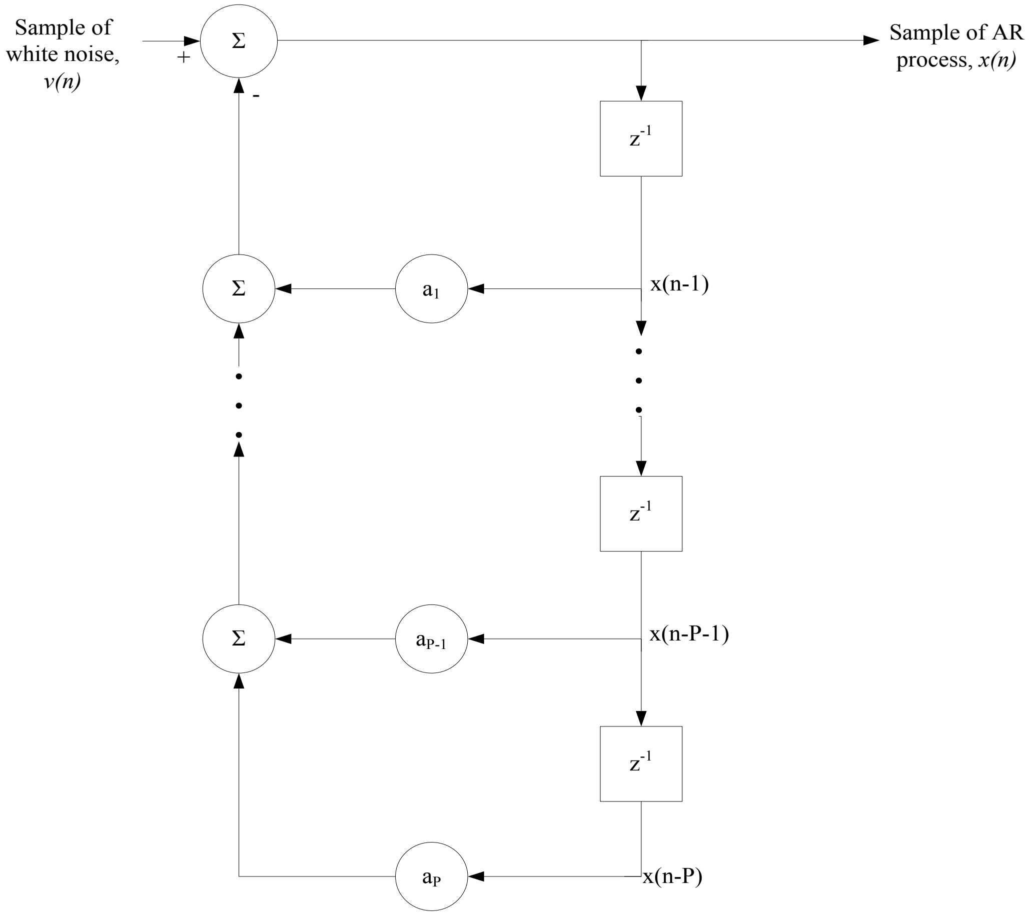

Figure 4.1 AR process generator

Resulting AR model is driven by a zero-mean additive white Gaussian noise (AWGN) as shown in Figure 4.1 to produce the output AR process $x(n)$ of ten minutes duration.

Figure 4.2 shows an example of a 2 second real and simulated background EEGs in the time domain.

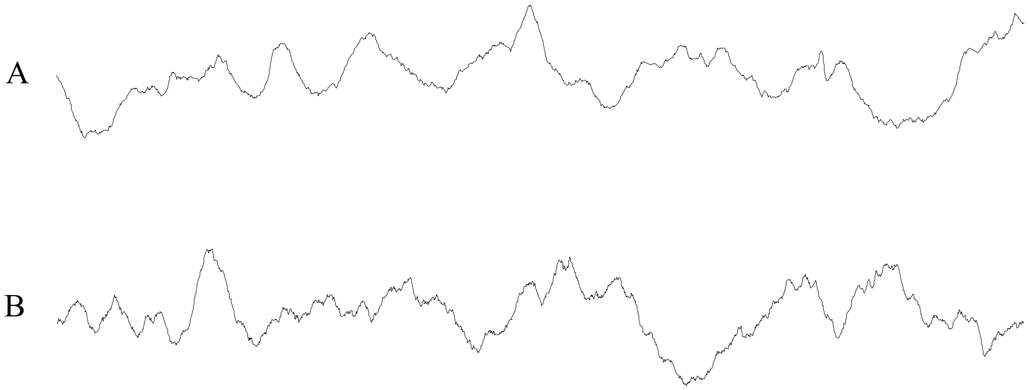

Figure 4.2 Example of real background EEG and simulated background EEG. **(A)** Real data background. **(B)** Simulated background EEG.

Figure 4.3 illustrates the power spectral density of the real and simulated signals, shown in Figure 4.2. As described earlier, simulated EEG signal should track the spectral density of the real EEG signal. It can be seen that the frequency contents of simulated data (Figure 4.3B) are almost the same as those of the real data (Figure 4.3A).

4.1.2 HFO Events Simulation

As discussed earlier, high frequency oscillations are classified into two categories: ripples (100-250 Hz) and fast ripples (250-500 Hz). They are narrow-band transients with predominant frequencies between 100 and 500 Hz and lasting in the order of milliseconds. We assume that the time-varying HFO events can be approximated by short bursts of sine waves with center frequencies in the range of 100 and 500 Hz that satisfy the properties of physiological HFOs.

To simulate the HFO events, we use linear chirp sine-waves in which the frequency increases linearly. Several signals with varying instantaneous frequencies between 100 and 500 Hz are generated. Depending on the type of events, ripples or fast ripples, segments of these signals with different lengths are selected to model the HFO events. Additionally, since the physiological HFO events have a spindle-like shape, the selected segments are multiplied by *"Hann windows*" to form spindle-shape of the events.

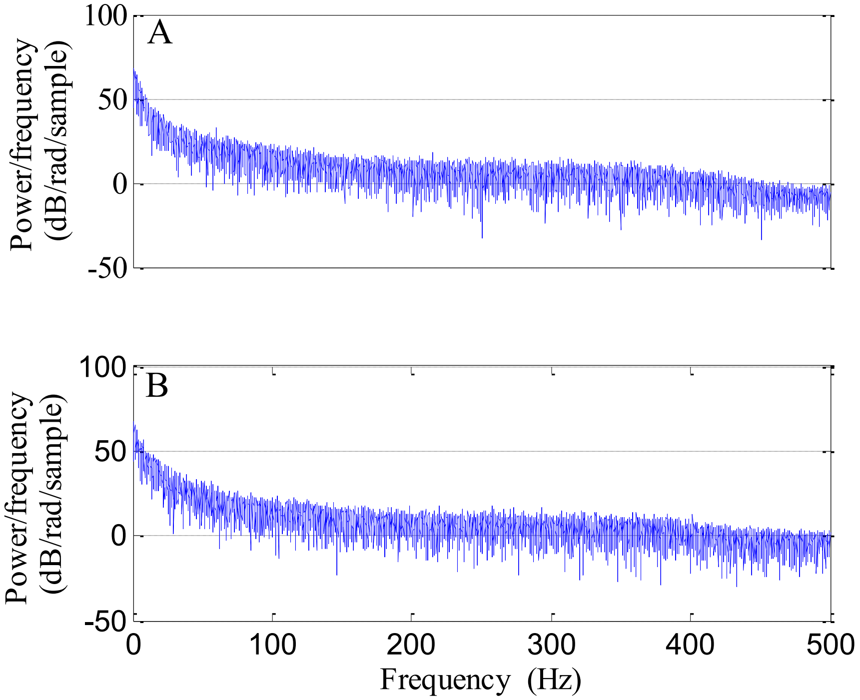

Figure 4.3 Power spectral density (PSD). **(A)** PSD of real data. **(B)** PSD of simulated data.

Regardless of the frequency and duration of ripples and fast ripples, the process of generating these two types of HFO events is almost identical. Therefore, in the following paragraphs, we first describe the basic process of generating HFO events. Later, we will present the different parameters used to simulate ripples and fast ripples separately.

Simulation of HFOs

HFO events can be modeled by short bursts of sine waves. However, the properties of simulated events such as frequency, duration, and shape should be as similar as possible to those of physiological HFOs.

To generate signals with frequencies in the HFO range, we use linear chirp signals. As mentioned earlier, in linear chirp signals, the instantaneous frequency varies linearly with time. That is, the frequency increases with time. Instantaneous frequency of a linear chirp signal is expressed by following equation.

$$w(n) = w_i + \alpha n \tag{4.5}$$

where n is discrete instances of time, w is the instantaneous frequency, w_i is the initial frequency, and α is the rate of frequency increase or chirp rate that controls the rate of change of the instantaneous frequency of the sinusoid. In this study α is set to 20.

Using the time varying Equation for $w(n)$ defined by (4.5), we generate the linear chirp signal $x(n)$

$$x(n) = \sin(2\pi(w(n))n + \varphi) \tag{4.6}$$

where φ is the initial random phase between $[0\ 2\pi]$.

In Equation (4.6), we generate samples of a sinusoid with instantaneous frequency (w) that is linearly swept. For example, if the initial frequency w_i is set to 126 Hz, in accordance with Equation (4.5), the frequency of $x(n)$ starts at 126 Hz at time $n = 0$ and it reaches to the value of 146 Hz (126 Hz + αn_1) at $n = n_1$, where n_1 is the last sample of the signal ($n_1 = 1\ sec$, in this work with a sampling rate of 1000 Hz).

Figure 4.4 illustrates an example of the frequency content of a generated signal. As can be seen in the time-frequency plot of Figure 4.4, the instantaneous frequency does not remain constant but increases to a maximum frequency at the end of the signal.

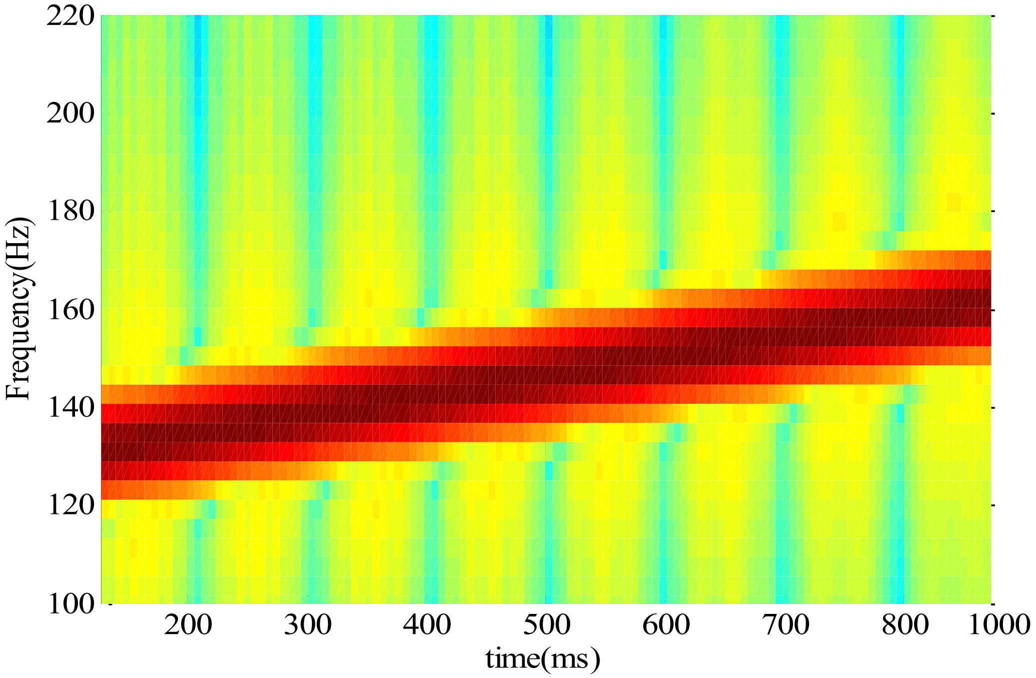

Figure 4.4 An example of a spectrogram of an $x(n)$. Note the linear change of frequency across the length of $x(n)$. The initial frequency for this signal is selected to be 126.81 Hz at $n = 0$ and is increased to 146.81 Hz at $n = 1$s.

We apply the above strategy to generate different signals $x(n)$ of one second duration with w_i in the range of 100 and 500 Hz. Therefore, if we select different segments of each $x(n)$, we obtain short-duration sine wave signals $x_{event}(n)$ with unique frequency.

$$x_{event}(n) = x(n) \qquad n_0 \leq n \leq n_0 + L \tag{4.7}$$

where n_0 is the instantaneous time of x_{event} and L is the duration of x_{event} . Depending on the type of HFO events, ripples or fast ripples, ten $x_{event}(n)$ with varying duration L (to be described later) are selected from each $x(n)$.

Figure 4.5 illustrates some examples of $x_{event}(n)$. As can be seen, the frequency content and length of each $x_{event}(n)$ are different.

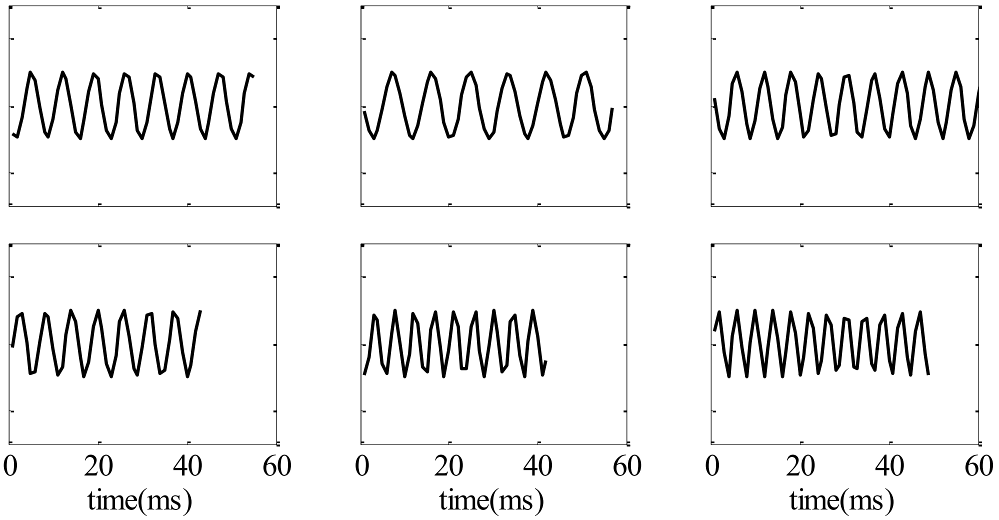

Figure 4.5 Some examples of simulated events with different frequencies and durations.

So far, we have generated HFO events as constant amplitude frequency modulated sinusoid bursts, as shown in Figure 4.5; however, in practice the HFO events have the shape of spindles. That is, the amplitudes taper at the start and end times of the events.

To create the smooth bell-shaped (spindle-shaped) events, we use the *"Hann window"*[80]. The "*Hann window"* has the shape of one cycle of a cosine wave and its coefficients are computed by the following equation:

$$W(n) = 0.5\left(1 - \cos\left(2\pi\frac{n}{L-1}\right)\right) \qquad 0 \leq n \leq L-1 \tag{4.8}$$

where L is the length of *"Hann window"* corresponding to the length of HFO event generated in Equation (4.7).

Multiplying *"Hann window"* coefficients with any signal forces the start and end times of the signal to be zero. Hence, to create the smooth bell-shaped (spindle-shaped) HFO events, we multiply each $x_{event}(n)$ by a *"Hann window"* of the same length as the $x_{event}(n)$.

$$e(n) = W(n) \times x_{event}(n) \qquad 0 \le n \le L \tag{4.9}$$

Figure 4.6 shows some examples of simulated events, $e(n)$. It can be observed that the HFO amplitudes diminish gradually at its start-time (when the event starts) and end-time (when the event finishes).

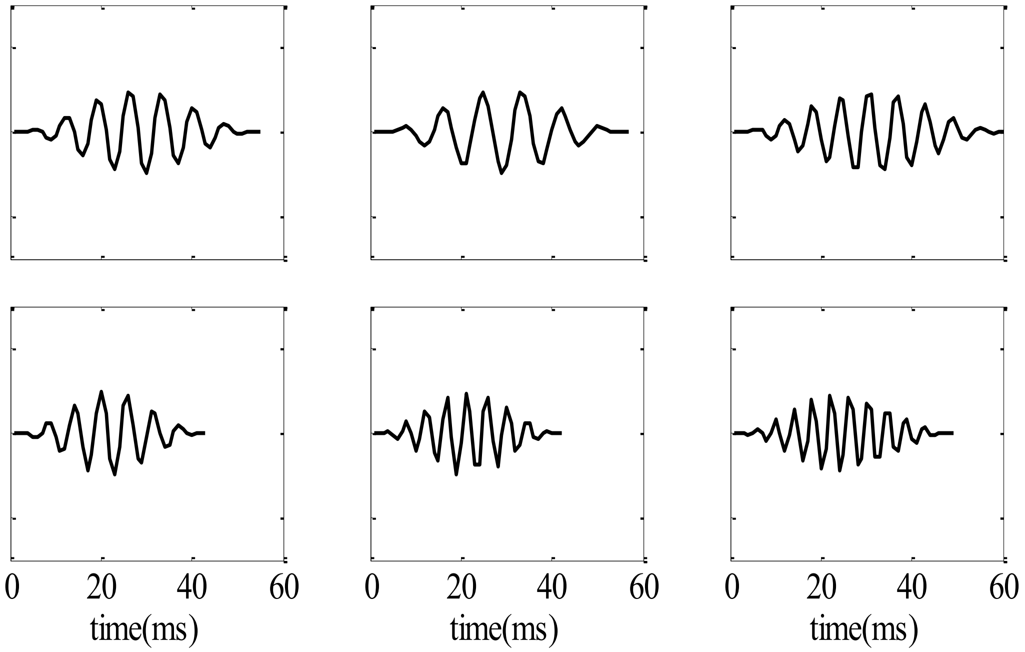

Figure 4.6 Some examples of ripples after being multiplied with Hann-windows. These examples are the same as were shown in Figure 4.5 .

We apply the above strategy to generate both ripple and fast ripple HFO events. The final simulated EEG with HFOs is generated by superimposing these simulated events on the simulated background EEG described earlier. Note that the simulated background signal has been generated from the wide-band IEEG with frequency ranging between 0 and 500 Hz, whereas the HFO events have been simulated in the high frequency range (250-500 Hz). Hence, to combine the simulated background signal and the HFO events, we must first apply a high-pass filter to the background signal. As described in Chapter 3, we apply high-pass filter with cut-off frequency of 100 Hz to reject the low frequency contents of the signal.

To superimpose the events on the EEG background signal, we define the SNR as the ratio between the energy of the HFO events to the energy of the high-pass filtered background EEG.

$$SNR_i = 10 \times log_{10} \frac{E_{event(i)}}{E_{Bg}} \tag{4.10}$$

In Equation (4.10), E_{event} and E_{Bg} are defined by

$$E_{event} = \frac{\sum_{i=1}^{L} |e(i)|^2}{L} \tag{4.11}$$

where $e(i)$ is the HFO signal and L is the length of events, and

$$E_{Bg} = \frac{\sum_{i=1}^{N} |y(i)|^2}{N} \tag{4.12}$$

where y is the high-pass filtered background EEG signal of length N samples. In this study, the length of the simulated EEG (Background and HFO events) is set to 600000 samples corresponding to 10 minutes at 1000 Hz sampling rate, while L, depending on the type of event, is randomly selected within the range of 25-60 ms.

In order to obtain a better understanding of the different SNR for a realistic data generation, *a priori* knowledge about the HFOs energy is required. In practice, the actual energy contribution of HFO events to the total EEG activity (background) is not well understood. Therefore, to ascertain the energy characteristics of the HFO events, we randomly select some visually detected HFO events (ripples and fast ripples) in the real IEEG from all patients and compared the normalized energies in accordance with Equations (4.11) and (4.12). The background activity epochs (500 ms) in real IEEG were visually selected from the samples surrounding the corresponding events in which sharp activities, spikes, artifacts and HFO events were not present. Figure 4.7 shows some examples of the HFO events with various SNR that have been selected from real data. Figure 4.8 illustrates the SNR levels for 52 distinct HFO events from 5 different patients.

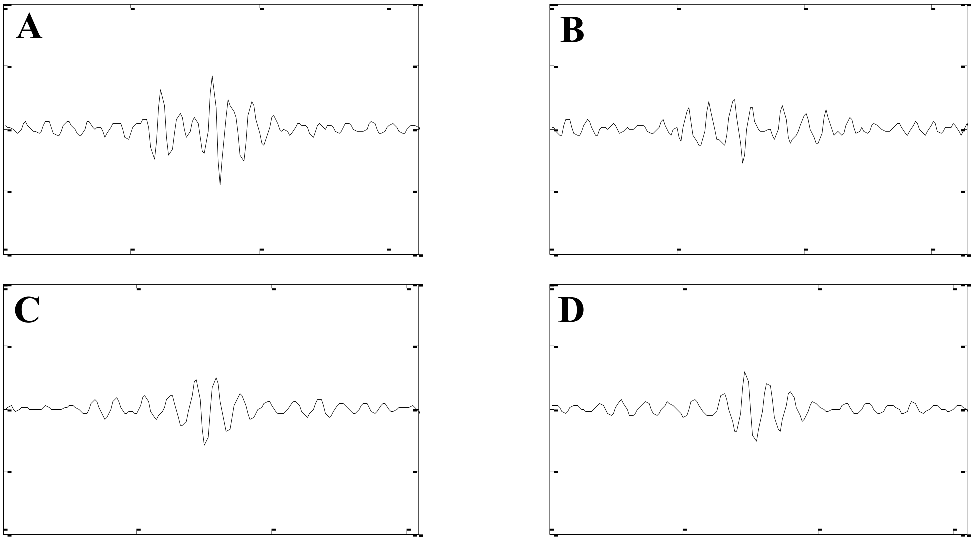

Figure 4.7 Some examples of HFO events in the real data selected from two patients. **(A)** 15 dB **(B)** 11 dB, **(C, D)** 20 dB.

As seen from Figure 4.8, in the real IEEG, the majority values of SNR lie in the range of 10 and 20 dB. With this in mind, we consider different signal-to-noise ratios (SNR) for superimposing the simulated HFO events on the simulated background signal. Specifically, we consider 3 distinct SNR levels 10, 15, and 20 dB.

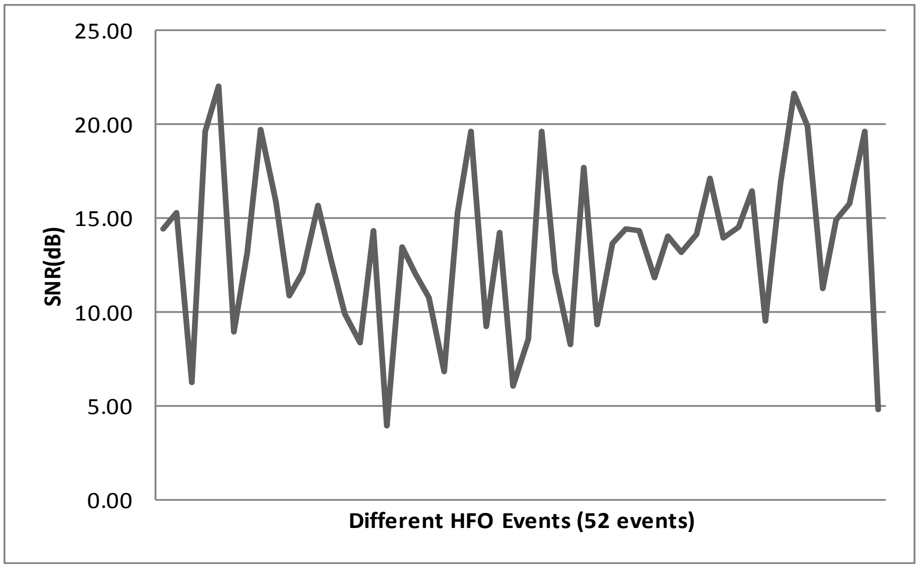

Figure 4.8 Different SNR levels obtained from 52 randomly selected HFO events of real IEEG from 5 different patients.

4.1.3 EEG Data Simulation

In practice, both ripples and fast ripples are located on the EEG background, and the existing automatic HFO detectors have been developed for EEG signals in which both types of events are found. To our knowledge, there has not been any study reporting IEEG signals with only ripples or only fast ripples. We, therefore, consider some of the possible situations in which the events can be superimposed on the background. We use four different cases to generate the simulated signals:

Case I: EEG signal with Ripples

Case II: EEG signal with fast ripples

Case III: EEG signal with a mixture of ripples and fast ripples

Case IV: EEG signal with ripples, fast ripples, and high energy transient interferences.

Following paragraphs provide detailed information for each of the above cases.

Case I – EEG Signal with Ripples

Ripple frequency varies between 100 and 250 Hz with the duration of a few milliseconds. We use these to simulate HFOs in the range of ripples. To simulate ripples, the initial frequency w_i in Equation (4.5) is randomly selected in the range of 100 and 250 Hz. The duration of each ripple (L) in Equation (4.7) varies randomly between 40 and 60 ms. We apply Equation (4.9) to create 500 ripples with different frequencies (w) and durations (L).

The simulated ripples are superimposed on the simulated background EEG with 3 different SNR levels. Either the energy of the simulated ripples or the background can be adjusted so that the desirable SNR level is reached. For a fixed SNR level, all ripples located on the background signal have identical energy compared to that of the background. Therefore, by scaling down the background EEG signal and then superimposing the simulated ripples on the signal, the required SNR level is attained. Overall, three different signals, each of 10-minute duration but distinct SNR levels are generated (Table 4.1). Locations of the simulated ripples are randomly selected on the 10 minute background signal with a minimum inter-event interval of 200 ms so that no two events overlap with each other. Table 4.1 shows the properties of three signals with 500 ripples that are simulated with 3 SNR levels.

Table 4.1 Ten minutes signals with 500 randomly located ripples with 3 SNR levels

Case I				
SNR (dB)	**Frequency range (Hz)**	**Number of events**	**Duration (ms)**	**Simulated signal length (min)**
10 dB	100 - 250	500	25-40	10 min
15 dB	100 - 250	500	25-40	10 min
20 dB	100 - 250	500	25-40	10 min

Figure 4.9 shows examples of simulated signals with ripples for the three SNR levels (10 dB (Figure 4.9A), 15 dB (Figure 4.9B), and 20 dB (Figure 4.9C)). As can be observed, the background signals are scaled down so that the desired SNR levels are obtained.

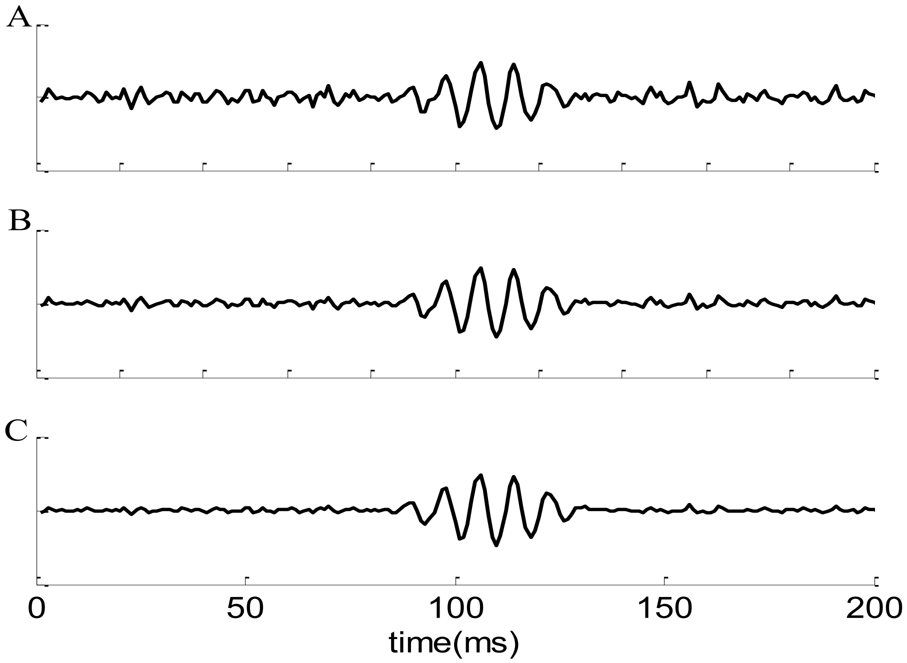

Figure 4.9 Background and ripples with different SNR levels. **(A)** SNR = 10 dB, **(B)** SNR = 15 dB, **(C)** SNR = 20 dB. Note that background signal is scaled down to obtain different SNR levels.

Case II – EEG Signal with Fast ripples

In contrast to the ripples, fast ripple frequency ranges between 250 and 500 Hz. Similar to ripples, fast ripples have a duration in the order of milliseconds; however, they are shorter than ripples. Due to these differences, we modified the initial frequency and the length of the HFO events used in Case I. Consequently, the initial frequency w_i in Equation (4.5) is randomly selected in the range of 250 and 500 Hz. The duration of each fast ripple (L) in Equation (4.7) randomly changes between 25 and 40 ms. Applying Equation (4.9), 600 fast ripples with different frequencies (w) and durations (L) are generated.

As described for Case I, the simulated background is scaled down so that different SNR levels are obtained. Therefore, three different signals, each of 10-minute duration, with different SNR levels are generated for Case II. Similar to the case of ripples, locations of the simulated fast ripples are randomly selected in 10 minute background signal within minimum inter-event intervals of 200 ms so that no two events overlap with each other. Table 4.2 lists the properties of the simulated signals with various SNR for Case II.

Table 4.2 Ten minute signals with 600 randomly located fast ripple with 3 SNR levels

Case II				
SNR (dB)	**Frequency range (Hz)**	**Number of events**	**Duration (ms)**	**Simulated signal length (min)**
10 dB	250 - 500	600	40-60	10 min
15 dB	250 - 500	600	40-60	10 min
20 dB	250 - 500	600	40-60	10 min

Figure 4.10 shows an example of a simulated signal including background and fast ripple with different SNR levels (A, B, C). As described earlier, the background signal amplitude is adjusted so that the desirable SNR is achieved.

Case III – EEG Signal with Mixture of Ripples and Fast ripples

For the previous two cases, we have described how the simulated EEG signals including the background and HFO events with different SNR were generated. It was assumed that all HFO events in the EEG have the same SNR and are classified into one of ripples or fast ripples across the length of signal. In reality, however, this is not the case. The HFO events do not have identical SNR levels, and both ripples and fast ripples can be found in the same IEEG signal. To imitate a more real-world EEG signal, we combine ripples and fast ripples with different SNR levels and superimpose them on the background signal. Applying Equations (4.5) to (4.9), a total number of 180 ripples and 180 fast ripples are generated. The parameters for the generation of these events are the same as the ones described for Case I and Case II.

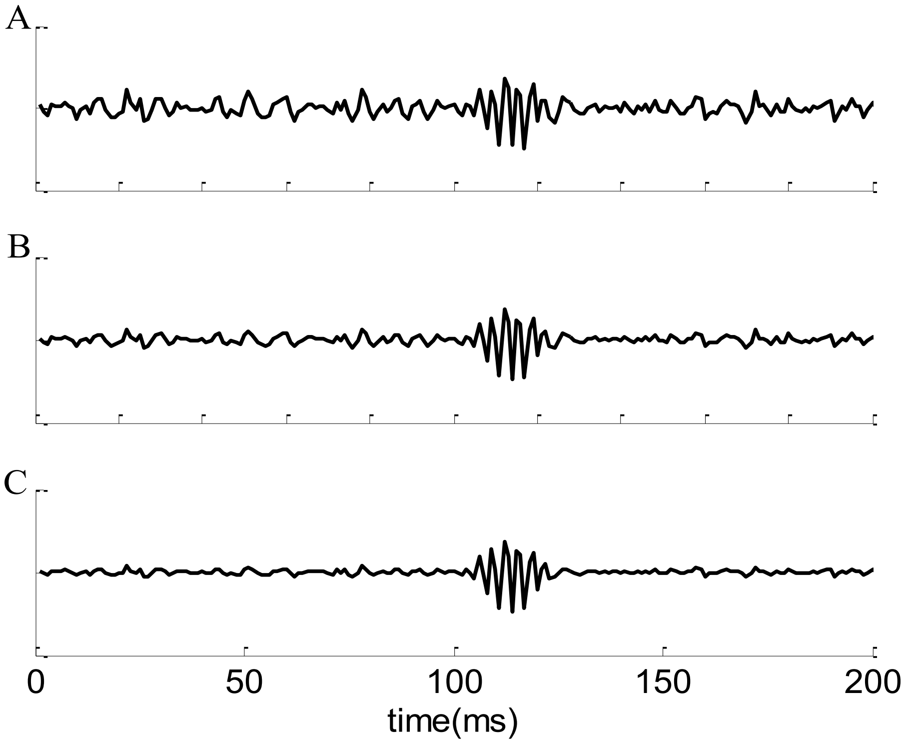

Figure 4.10 Background and fast ripples with different SNR levels. **(A)** SNR = 10 dB, **(B)** SNR = 15 dB, **(C)** SNR = 20 dB. Note that background signal is scaled down to obtain different SNR levels.

Initial frequency w_i and duration L are randomly selected based on the type of the event. That is, if the simulated event is a ripple, w_i is selected between 100 and 250 Hz and L randomly varied between 40 and 60 ms, whereas if the simulated event is a fast ripple, w_i and L are selected in the range of 250 and 500 Hz, and 25 and 40 ms, respectively. Table 4.3 summarizes the simulated signal for Case III.

Unlike the previous cases, simulated HFO events are not superimposed on the background signal for a constant SNR. In this case, the SNR level changes from one event to another. We do not adjust the background signal to obtain a fixed SNR. To consider different SNRs for each event; we instead adjust the amplitude of each event individually.

Table 4.3 Ten minute signal with 360 randomly located ripples and fast ripples

Case III				
SNR (dB)	**Frequency range (Hz)**	**Number of events**	**Duration (ms)**	**Simulated signal length (min)**
10 - 20 dB	100-250	180	25-40	10 min
10 - 20 dB	250-500	180	40-60	

As in Case I and II, locations of the simulated events are randomly selected between 1 and 10 minutes of a constant amplitude background with minimum inter-event intervals of 200 ms.

Figure 4.11 illustrates an example of two simulated events, a ripple and a fast ripple, with different SNR superimposed on the constant energy simulated background signal. In this case, instead of scaling down the background signal, events are scaled up or down to achieve the desired SNR.

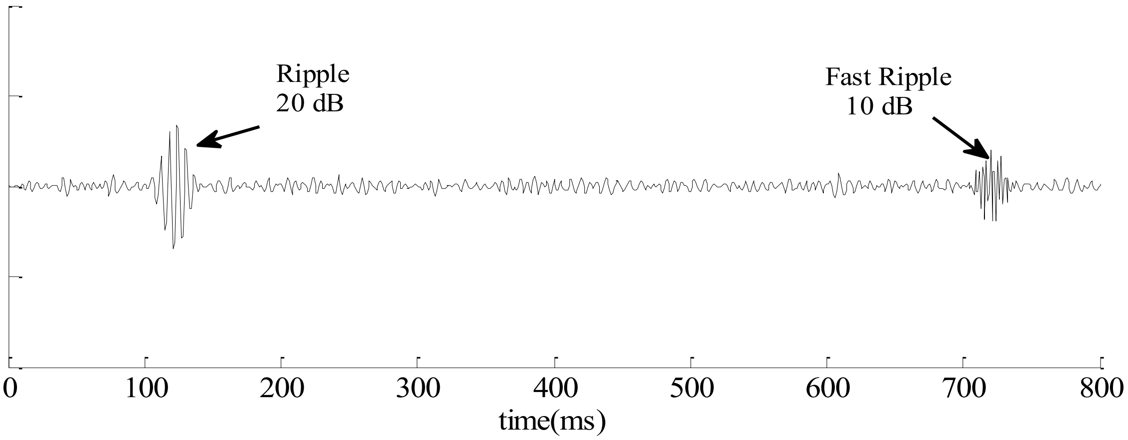

Figure 4.11 A simulated ripple (20 dB) and a simulated fast ripple (10 dB) are located in the same background.

Case IV – Combined ripples and Fast ripples with high energy interferences

Thus far, we have simulated EEG signals for ideal Cases I, II, and III, where there are no interferences from other types of transient events such as spikes, sharp-waves, noise or other strong HFO signals. In practice, however, it is not uncommon that high energy interferences, noises or artifacts co-exist with HFO events in the EEG signal. The presence of high-energy HFO interferences in the neighbourhood of HFOs or in the background can significantly affect the performance of the detectors. The presence of noise or strong events would increase the thresholds for automatic HFO detectors resulting in poor performance. Thus, in Case IV, high-energy interferences are combined with more realistic HFO events (SNR: 10-20 dB) that were discussed in Case III. Our goal is to evaluate the performance of automatic HFO detectors under more realistic situations.

To simulate this type of data, we first generate the data exactly as in Case III, that is, ripples and fast ripples with SNR levels between 10 and 20 dB are added to the background signal. To this signal, we also add two additional high energy interferences (one ripple and one fast ripple, only one of each). The SNR of these two interferences are selected to be much higher than that of the existing HFO events and is set to 40 dB. The aim is to see the impact of the interferences on the performance of the detectors.

Table 4.4 shows the quantity, duration and frequency ranges of events including ripples, fast ripples and high-energy events that are used to simulate EEG signal for Case IV.

Figure 4.12 shows an example of a small section of the simulated IEEG. As can be seen from the figure, a high amplitude interference with an SNR of 40 dB, and an HFO event with an SNR between 10-20 dB are combined with the background signal.

Table 4.4 Ten minute signal with 360 randomly located realistic HFOs and two high energy HFOs

Case IV				
SNR (dB)	**Frequency range (Hz)**	**Number of events**	**Duration (ms)**	**Simulated signal length (min)**
10,15,20 dB	100 - 250	180	25-40	10 min
10,15,20 dB	250 - 500	180	40-60	
40 dB	100 - 500	2	25-60	

4.2 Performance Comparison of HFO detectors

In the previous section, we have simulated four cases of EEG signal (background & HFOs). We now compare the performance of all the HFO detectors using these simulated data.

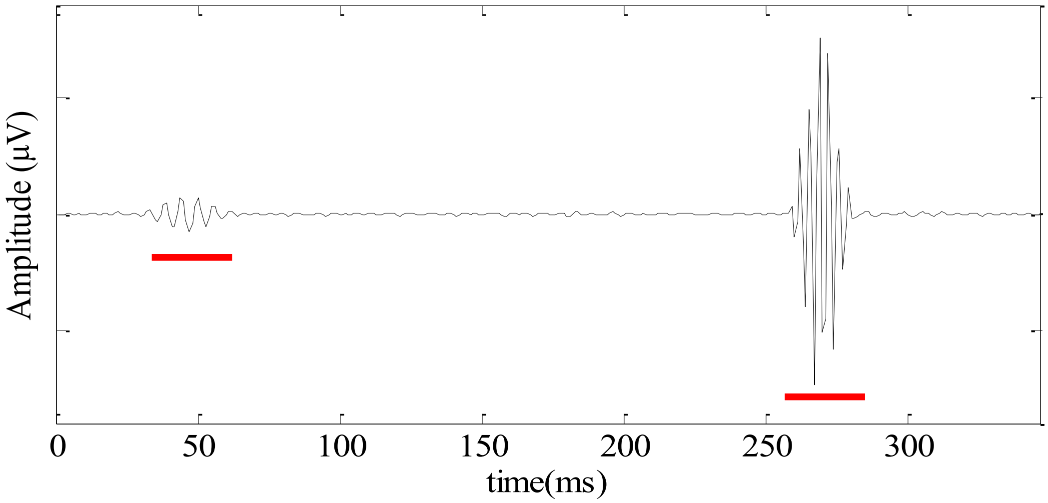

Figure 4.12 A section of the simulated EEG signal with an HFO event in the presence of very high energy interference. The interference has a SNR value of 40 dB. Events are highlighted by red line.

4.2.1 Performance Metrics

Sensitivity and specificity are two metrics that are mainly used to quantify the performance of HFO detectors. These metrics are often used when the detection of an event is compared against another set of events which serve as the Gold standard. For a simulated signal, the gold standard is clear, as the location of the simulated events are exactly known.

Sensitivity of a detector is defined as the percentage of the true HFO events (Gold standard) that are detected by the algorithm and is computed as the ratio of the detected true positive (TP) events to the total number of events:

$$Sensitivity = 100 \times \frac{N_{TP}}{N_{TP} + N_{FN}} \tag{4.13}$$

where N_{TP} is the number of true positive events, N_{FN} is the number of false negative (FN) events. An automatic detected event is identified as TP, if it overlaps with the simulated HFO events located in the background data. On the other hand, FN events are those events that have been identified in the gold standard, but an automatic detector fails to detect them (Figure 4.13). Note that the combination of TP and FN events is equivalent to the total number of events in the data in accordance with the gold standard.

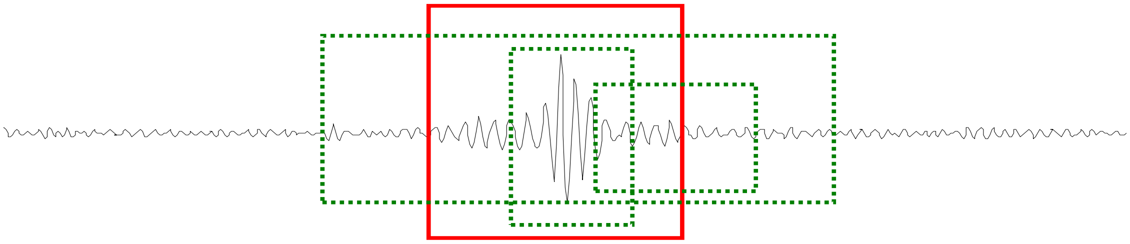

Figure 4.13 Examples of TP detections. Red box shows an HFO gold standard event. Dashed green boxes indicate different possibilities for an event to be detected as TP.

Specificity of a detector is determined as the percentage of detected HFO events that are

TP and is mathematically expressed as follows:

$$Specificity = 100 \times \frac{N_{TP}}{N_{TP} + N_{FP}} \tag{4.14}$$

where N_{TP} is the number of true positive events and N_{FP} is number of false positive events. FP is the automatically detected event that corresponds to the background (where no event exists). That is, if an event is detected by an automatic detector in background signals, it is defined as an FP event. In this study, a detected event by an automatic detector must intersect with a gold standard event for at least one sample to be defined as TP.

Receiver operating characteristic (ROC) is another metric that is often used to evaluate the performance of a detector as a function of the detection threshold or some algorithm parameter. There are two ROC graphical representations that are used. In the first case, sensitivity is plotted against false positive detection rate (FPR) which is defined as (1-Specificity), with varying thresholds (Figure 4.14A), while in the other case both sensitivity and specificity are plotted for various detection thresholds (Figure 4.14B). In the latter, each point of the curve represents a sensitivity/ specificity pair corresponding to a threshold. As can be seen from Figure 4.14, sensitivity is inversely proportional to the detection threshold, while specificity is directly proportional to the threshold value. That is, by increasing the detection threshold, the detector sensitivity decreases, whereas its specificity increases.

In the present work, the second version of ROC analysis (Figure 4.14B) is applied for the three newly proposed HFO detectors based on the sharpness to find the threshold that gives the optimum results. We define the "optimum" threshold as the point at which sensitivity and specificity curves cross each other. This point represents equal sensitivity and specificity – a balance in the two metrics. Based on the ROC analysis, Table 4.5 lists the optimum threshold values evaluated for all the simulated signals for Cases I-IV.

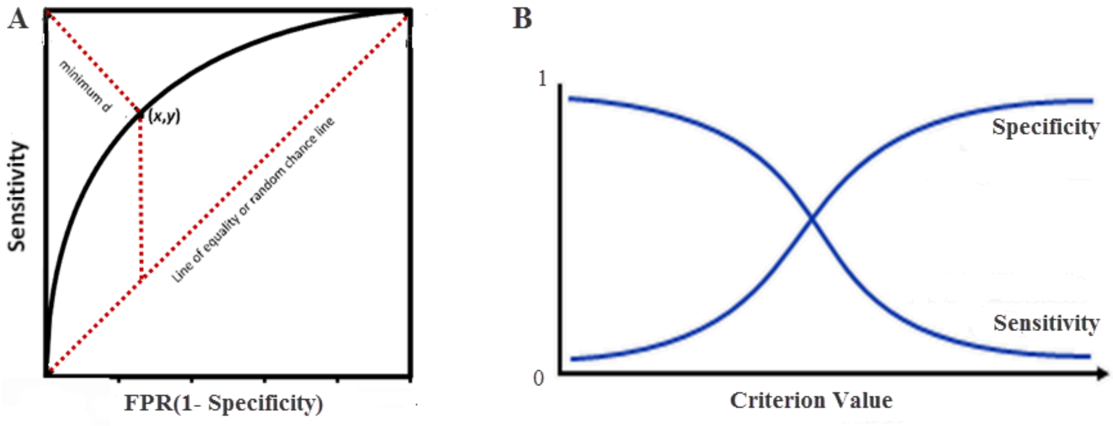

Figure 4.14 ROC curves. (A) Sensitivity is plotted in a function of false positive rate. (B) Sensitivity and Specificity are plotted as a function of threshold.

Table 4.5 Optimum threshold selected for simulated signals.

Simulated Signal	**SNR levels**	**Threshold (%)**		
		Slope Detector	**Slope_dynamic Detector**	**Slope_Causal Detector**
Case I	10 dB	88.5	88.5	94.5
	15 dB	96	97	88
	20 dB	96	97.5	85
Case II	10 dB	96	98	98
	15 dB	95.5	96.5	93.5
	20 dB	95.5	94	85.5
Case III	10,15,20 dB	96	97.5	96.5
Case IV	10,15,20,40	97	97.5	97

4.2.2 Results

As mentioned previously, in Cases I and II, ripples and fast ripples are combined with background data at three different SNRs, respectively. In Case III, a mixture of HFO events, both ripples and fast ripples, at three different SNR levels are added to the simulated background. Finally in Case IV, a signal with a mixture of ripples and fast ripples in the presence of high amplitude interferences are generated.

We evaluate the performance of the HFO detectors described in Chapter 3 using these simulated signals. The following paragraphs present the simulation results.

4.2.2.1 Case I – EEG Signal with Ripples

Table 4.6 lists the performance of each of the detectors in terms of the sensitivity and specificity for simulated ripple signals at all three different SNR levels. Figure 4.15 illustrates the average sensitivity and specificity for all the detectors across all SNR levels. The RMS and STLL detectors result in a sensitivity of 98.07% and 99.73%, and a specificity of 100% and 99.93%, respectively. The STLL detector is the only detector that results in a specificity of less than 100% for SNR level of 10 dB. This is due to a detected false positive event. MS1 and MS2 detectors report the best performance amongst all the detectors with sensitivity and specificity of 100% each for all SNR levels. Proposed detectors that are based on the sharpness of half-wave of signals, Slope, Iterative-Slope and Slope_Causal, result in almost identical sensitivities, 99.40%, 99.40% and 99.67% respectively. They are higher than the RMS detector, albeit less than those of MS1 and MS2 detectors. The specificities of these detectors are 100% for all SNR levels.

It can be seen that increasing the SNR levels of the events leads to better performance for all the detectors. That is, the number of TP detected by all HFO detectors increase once the SNR levels of the events are increased.

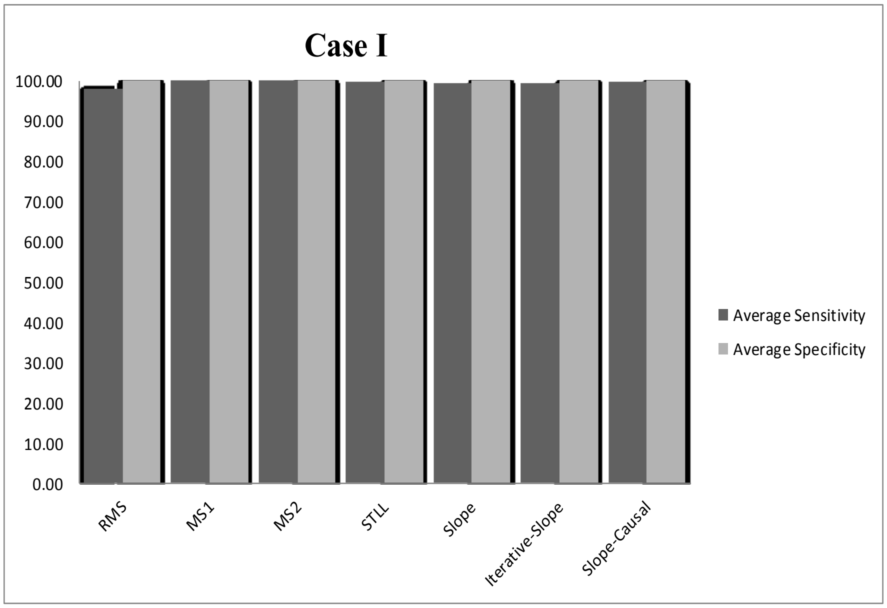

Figure 4.15 Comparison of detectors performances. Average sensitivity and specificity of all detectors for Case I with respect to SNR levels.

Figure 4.16A illustrates one TP (detected event) and one FN ripple at SNR of 15 dB by RMS method. Figure 4.16B shows the RMS energies of these two events. It can be seen that the energy the FN event is not high enough to satisfy the detection threshold (δ_{RMS}) that was selected from the full length of the signal, and subsequently it cannot be detected by the RMS detector, whereas the energy of the TP event exceeded the detection threshold and was detected by this detector. Although the energy of the FN ripple in this signal is high, the probable reason for it not being detected may be due to the short length that was randomly selected for this ripple. It is seen that the TP event has a longer duration and its energy is subsequently greater than the energy of the FN event.

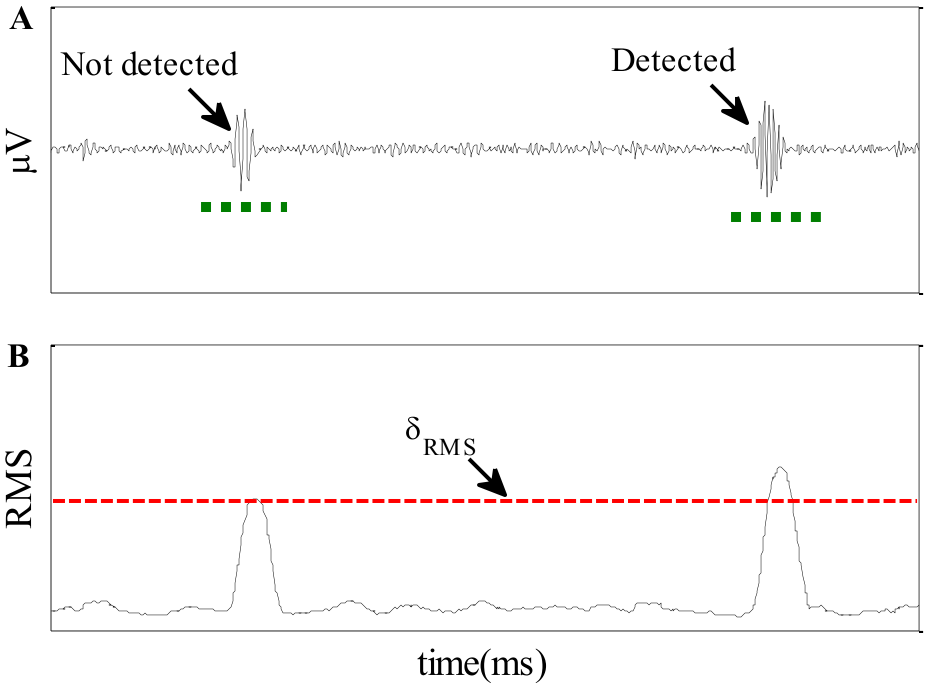

Figure 4.16 Some examples of FN events by RMS detector. **(A)** Simulated events for Case I with 15 dB SNR. **(B)** Root mean square energy of events. Threshold for the signal is indicated with dashed red lines.

Figure 4.17A shows some examples of simulated events with SNR 10 dB not being detected by any of the sharpness detectors. Figure 4.17B illustrates the absolute values of the slopes of HWs for the events. The reason for this failure is the number of sharpness of half-waves. As can be seen, in these events, the numbers of SHWs greater than the threshold are less than 8 (minimum detection criterion) therefore are not detected as events.

Figure 4.18 illustrates an example of ripple at SNR 10 dB that could not be detected by the STLL detector. Energy of this event exceeded the threshold (red line) but the duration of the STLL energy, shown between dashed blue lines, does not satisfy the minimum length of 12 ms (set for this detector) and therefore this event cannot be detected by the STLL method.

Table 4.6 Sensitivity and Specificity for all detectors for simulated EEG background and ripples with different SNR levels. Average Sensitivity and Specificity of each detector are shown at the bottom of table.TP = true positive, FP = false positive

Total	**500**	**Case I**						
SNR	**Methods**	**RMS**	**MS1**	**MS2**	**STLL**	**Slope**	**Iterative-Slope**	**Slope-Causal**
10 dB	**TP**	473	500	500	497	491	491	495
	FP	0	0	0	1	0	0	0
	Sensitivity (%)	94.60	100.00	100.00	99.40	98.20	98.20	99.00
	Specificity (%)	100.00	100.00	100.00	99.80	100.00	100.00	100.00
15 dB	**TP**	498	500	500	499	500	500	500
	FP	0	0	0	0	0	0	0
	Sensitivity (%)	99.60	100.00	100.00	99.80	100.00	100.00	100.00
	Specificity (%)	100.00	100.00	100.00	100.00	100.00	100.00	100.00
20 dB	**TP**	500	500	500	500	500	500	500
	FP	0	0	0	0	0	0	0
	Sensitivity (%)	100.00	100.00	100.00	100.00	100.00	100.00	100.00
	Specificity (%)	100.00	100.00	100.00	100.00	100.00	100.00	100.00
Average Sensitivity		98.07	100.00	100.00	99.73	99.40	99.40	99.67
Average Specificity		100.00	100.00	100.00	99.93	100.00	100.00	100.00

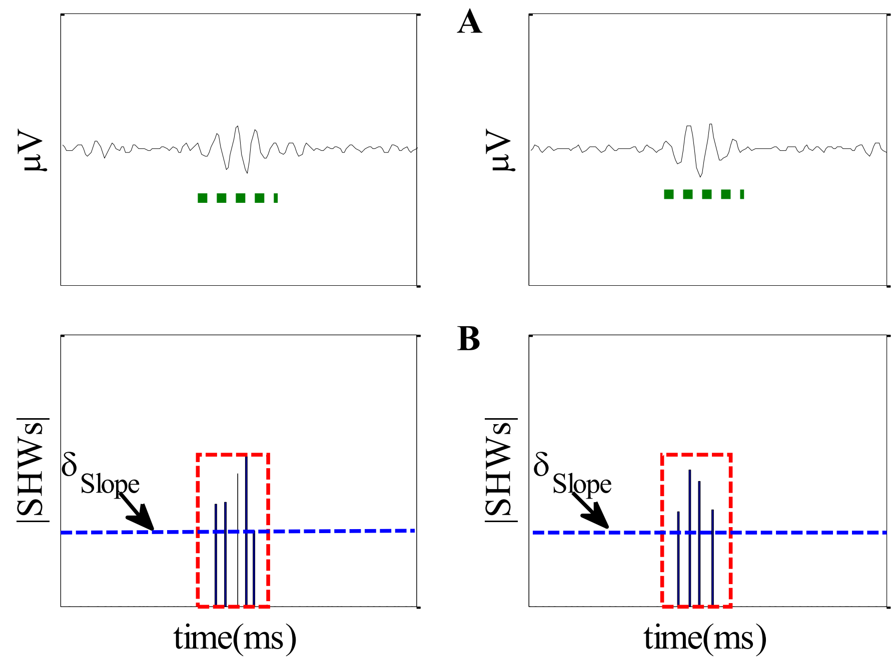

Figure 4.17 Examples FN detection by Sharpness based methods. **(A)** Simulated events for Case I with 15 dB SNR, dashed green lines indicate simulated event. **(B)** Sharpness of half-waves of signals. Solid blue lines indicate the detection threshold, dashed red line indicate the SHWs greater than δ_{Slope}.

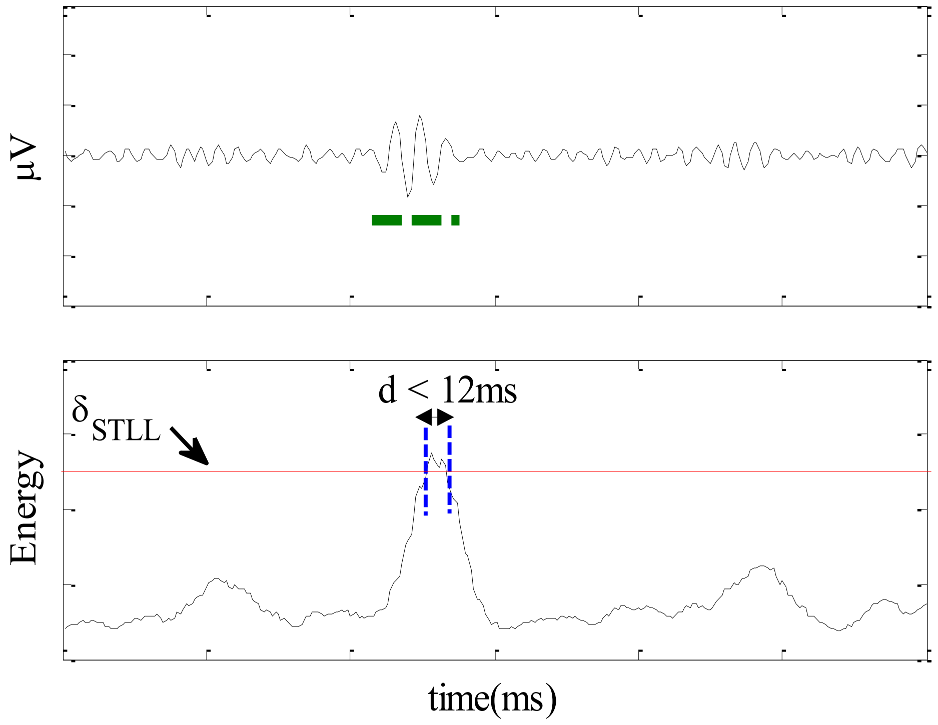

Figure 4.18 An example of FN ripple at SNR level of 10 dB STLL detector. **(Top)** EEG signal with ripple, dashed green line indicates the simulated ripple **(Bottom)** STLL energy of signal. Red line indicates the detection threshold, and dashed blue lines indicate the length of energy greater than threshold.

4.2.2.2 Case II – EEG Signal with Fast Ripples

Table 4.7 lists the performance of each detector in terms of sensitivity and specificity for simulated fast ripples at different SNR levels. Figure 4.19 shows the average sensitivity and specificity for all detectors across all SNR levels. The performances of RMS and STLL detectors improve as the SNR levels of fast ripples increases; however, sensitivity of the RMS detector never reaches 100%. Modified versions of RMS, MS1 and MS2, and sharpness-based detectors report perfect sensitivity and specificity (100%) for all simulated fast ripples.

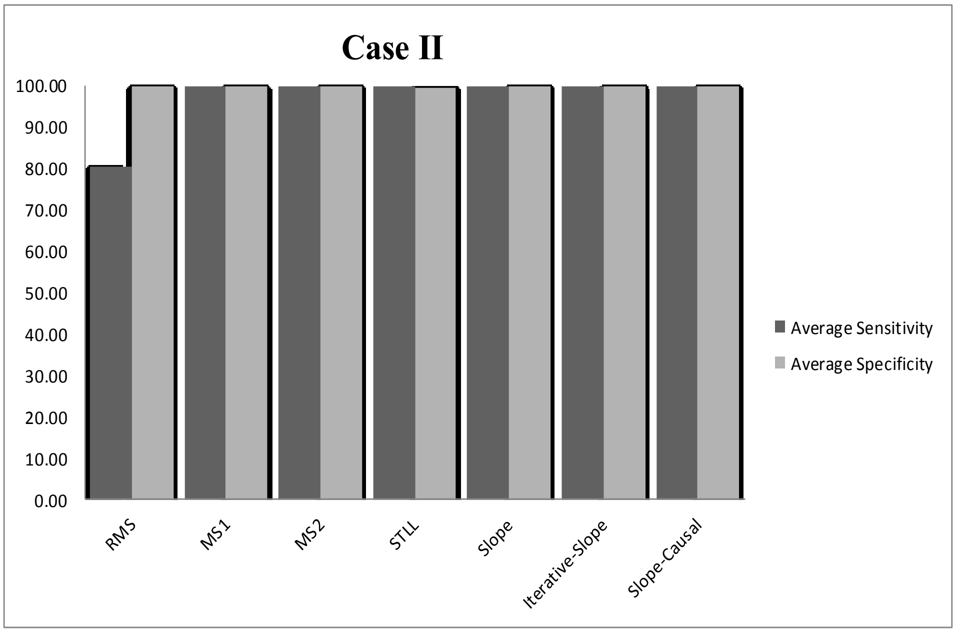

Figure 4.19 Comparison of detectors performances. Average sensitivity and specificity of all detectors for Case II with respect to SNR levels.

RMS detector does not report a good sensitivity resulting in sensitivity of 80.39% and specificity of 100%. The probable reason for poor sensitivity of this detector might be the short length selected for the simulated fast ripples. The energy of these events may not satisfy the detection criteria for the RMS detector. STLL detector reports sensitivity and specificity of 99.89% and 99.93%, respectively. MS1, MS2, and the proposed detectors including Slope, Iterative-Slope, and Slope-Causal show perfect performance in terms of sensitivity and specificity for all SNR levels.

Some examples of FN simulated events are shown in Figure 4.20. Figure 4.20A shows two examples of simulated fast ripples generated at SNR 20 dB. The RMS values of these signals are illustrated in Figure 4.20B. It is seen that these events are real events and a reliable detector should be able to discriminate between these events and the background signal. However, similar to that in Case I, the energy of these events is not that high to cross the detection threshold, and as a result, RMS detector fails to detect them.

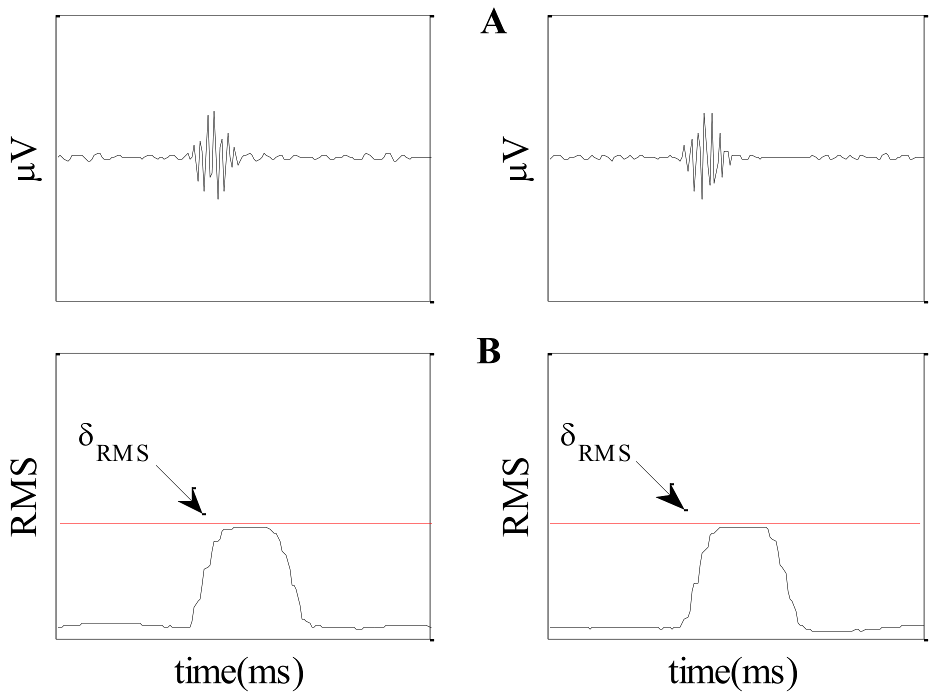

Figure 4.20 Some examples of FN events by RMS detector. **(A)** Simulated events for Case II with 20 dB SNR. **(B)** Root mean square energy of events. Threshold for the signal is indicated with dashed red lines.

4.2.2.3 Case III - EEG Signal with Mixture of Ripples and Fast ripples

The results for all the detectors for Case III for various SNR levels are given in Table 4.8. Figure 4.21 illustrates the sensitivity and specificity for all the detectors. It is seen from this table that the proposed methods, Slope, Iterative-Slope, and Slope-Causal detectors exhibit the best performance in sensitivity and specificity (100%).

Unlike the results obtained for Cases I and II, MS1 and MS2 detectors do not function well. MS1 results in a sensitivity of 78.61% while MS2 performs a little bit better resulting in a sensitivity of 85%; however, the specificity of both of the detectors is still 100% meaning that no false positive events are detected. The sensitivity of STLL detector is 100% but the number of false positive detections increased yielding lower specificity. On the other hand, RMS detector has a drastic degradation in terms of sensitivity compared to the results for Cases I and II (57.50% vs. 98.07% for ripples and 80.28% for fast ripples). The probable reason for this is the presence of different types of events with varying SNR levels. Since the detection threshold for this method is selected from the complete signal, the presence of strong energy HFO events increase the threshold resulting in missing lower energy events. The specificity of this detector still remains 100%. That is, all the detected events are actual events. In MS1 and MS2, shorter epoch of the signal is used to select the detection threshold. This may be the reason why these methods result in better performance compared to that of the RMS detector. In MS2, as pointed out earlier, a sliding window is applied for segmenting the signal and the data in each epoch is updated every 10 seconds. That is, once the new data arrives, a new threshold is computed for the epoch. In this case, there may exist some HFO events in one-minute epoch that the detector fails to detect, but they can be detected with the new threshold. This may be a likely reason for better performance of MS2 compared to that of the MS1 detector.

Table 4.7 Sensitivity and Specificity for all detectors for simulated EEG background and fast ripples with different SNR levels. Average Sensitivity and Specificity of each detector are shown at the bottom of table.TP = true positive, FP = false positive

Total	**600**	**Case II**						
SNR	**Methods**	**RMS**	**MS1**	**MS2**	**STLL**	**Slope**	**Iterative-Slope**	**Slope-Causal**
10 dB	**TP**	408	600	600	600	600	600	600
	FP	0	0	0	5	0	0	0
	Sensitivity (%)	68.00	100.00	100.00	100.00	100.00	100.00	100.00
	Specificity (%)	100.00	100.00	100.00	99.17	100.00	100.00	100.00
15 dB	**TP**	508	600	600	599	600	600	600
	FP	0	0	0	0	0	0	0
	Sensitivity (%)	84.67	100.00	100.00	99.83	100.00	100.00	100.00
	Specificity (%)	100.00	100.00	100.00	100.00	100.00	100.00	100.00
20 dB	**TP**	531	600	600	599	600	600	600
	FP	0	0	0	0	0	0	0
	Sensitivity (%)	88.50	100.00	100.00	99.83	100.00	100.00	100.00
	Specificity (%)	100.00	100.00	100.00	100.00	100.00	100.00	100.00
Average Sensitivity		**80.39**	**100.00**	**100.00**	**99.89**	**100.00**	**100.00**	**100.00**
Average Specificity		**100.00**	**100.00**	**100.00**	**99.72**	**100.00**	**100.00**	**100.00**

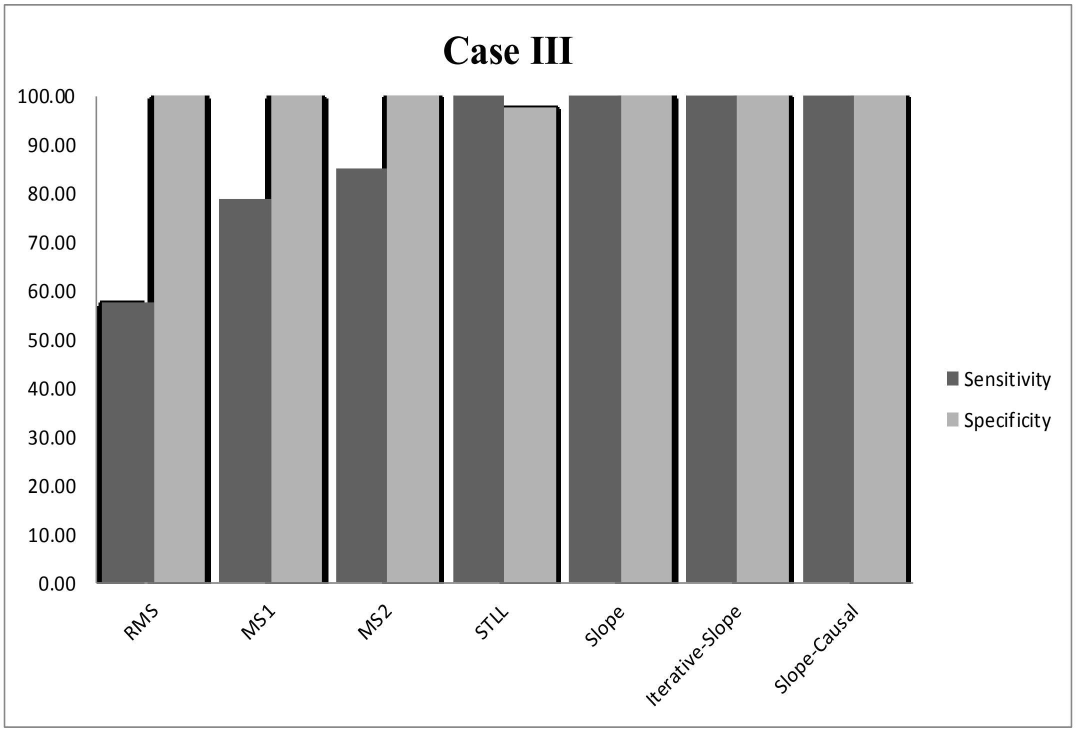

Figure 4.21 Comparison of detectors performances for Case III.

As seen from Table 4.8, there exists some false positive detection in the STLL detector. One example of FP detected event is shown in Figure 4.22. In this figure, two events (one TP and one FP event) located beside each other are illustrated. As can be seen, the energy of the real event is much higher than the energy of the FP detected event; however, the latter has an energy greater than the threshold for a sufficient amount of time and subsequently is detected by the STLL detector. By increasing the detection threshold, FP events may be successfully removed; nevertheless, as a trade-off between sensitivity and specificity, the number of TP events and consequently the sensitivity of this method would be reduced.

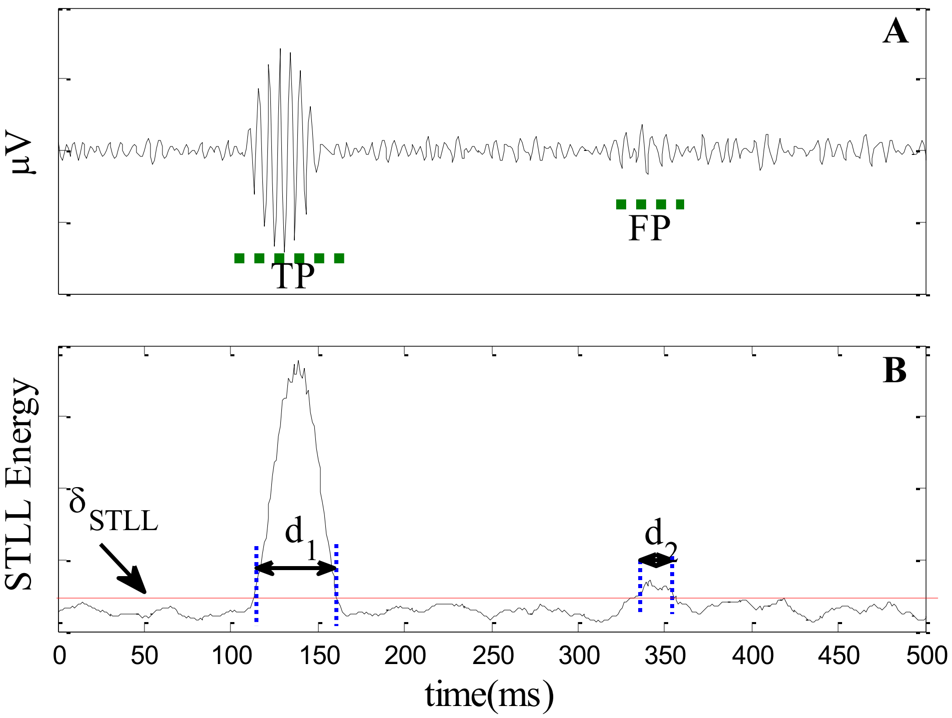

Figure 4.22 Examples of TP and FP detected events by STLL detector. (Top) EEG signal, dashed green lines indicate TP and FP events. (Bottom) STLL energy of the signal. Solid red line indicates the detection threshold, blue dashed lines indicates the boundaries of the detected events. d_1 and d_2 correspond to the duration of the detected events.

4.2.2.4 Case IV – Combined ripples and fast ripples with high energy interferences

The results for all the detectors for Case IV are given in Table 4.9. Figure 4.23 illustrates the sensitivity and specificity for all the detectors. As in Case III, it is observed from this table that the proposed methods, Slope, Iterative-Slope, and Slope-Causal detectors have the best performance in terms of sensitivity and specificity (100%), while MS1 and MS2 detectors do not perform that well. Compared to the results for Case III, the performance of RMS, MS1, and MS2 detectors is worsened. The performance of MS1 and MS2, however, does not degrade as much as that of the RMS detector. MS1 results in a sensitivity of 73.76% while MS2 results in a sensitivity of 81.22%.

Table 4.8 Sensitivity and Specificity for all detectors for Case III. TP = true positive, FP = false positive.

Total	**360**	**Case III**						
SNR	**Methods**	**RMS**	**MS1**	**MS2**	**STLL**	**Slope**	**Iterative-Slope**	**Slope-Causal**
10-15-20 dB	**TP**	207	283	306	360	360	360	360
	FP	0	0	0	9	0	0	0
Sensitivity		**57.50**	**78.61**	**85.00**	**100.00**	**100.00**	**100.00**	**100.00**
Specificity		**100.00**	**100.00**	**100.00**	**97.56**	**100.00**	**100.00**	**100.00**

Table 4.9 Sensitivity and Specificity for all detectors for Case IV. TP = true positive, FP = false positive

Total	**362**	**Case IV**						
SNR	**Methods**	**RMS**	**MS1**	**MS2**	**STLL**	**Slope**	**Iterative-Slope**	**Slope-Causal**
10-15-20, 40dB	**TP**	165	267	294	362	362	362	362
	FP	0	0	0	9	0	0	0
Sensitivity		**45.58**	**73.76**	**81.22**	**100.00**	**100.00**	**100.00**	**100.00**
Specificity		**100.00**	**100.00**	**100.00**	**97.57**	**100.00**	**100.00**	**100.00**

Similar to Case III, the RMS detector has the worst performance in terms of sensitivity (45.58%), but the specificity of this detector still remains at 100%. The sensitivity of STLL detector remains at 100%, but reported lower specificity.

In Case IV, RMS, MS1, and MS2 detectors failed to detect a large number of true events. Large number of FN events in the results of the root mean square energy-based detectors, including RMS, MS1, and MS2, suggests that the presence of varying energy HFO events or high-energy interference significantly affect the performance of these HFO detectors. That is, due to the high detection threshold selected from such signals (i.e. Case IV), a large amount of real events are missed by these detectors.

Two examples of FN events are shown in Figure 4.24A. Figure 4.24A shows the events in time domain, whereas Figure 4.24B illustrates the root mean square energy of the events. It is seen that these real events have energies much higher than that of their surrounding background signals. However, since in signals such as in Cases III and IV, the simulated signals contain HFO events of different SNR levels the detection thresholds selected from the full length of signal is high. Consequently, the energy of events with low SNRs does not cross the threshold value and hence such events are not detected.

4.3 Discussion

The goal of this study was to compare the performances of automatic HFO detectors with simulated signals under different conditions. As discussed in the previous chapters, one of the most fundamental problems in studying HFOs is the lack of a Gold Standard definition for HFOs. EEGers are not always unanimous about what constitutes an HFO event, which makes the HFO interpretation highly subjective.

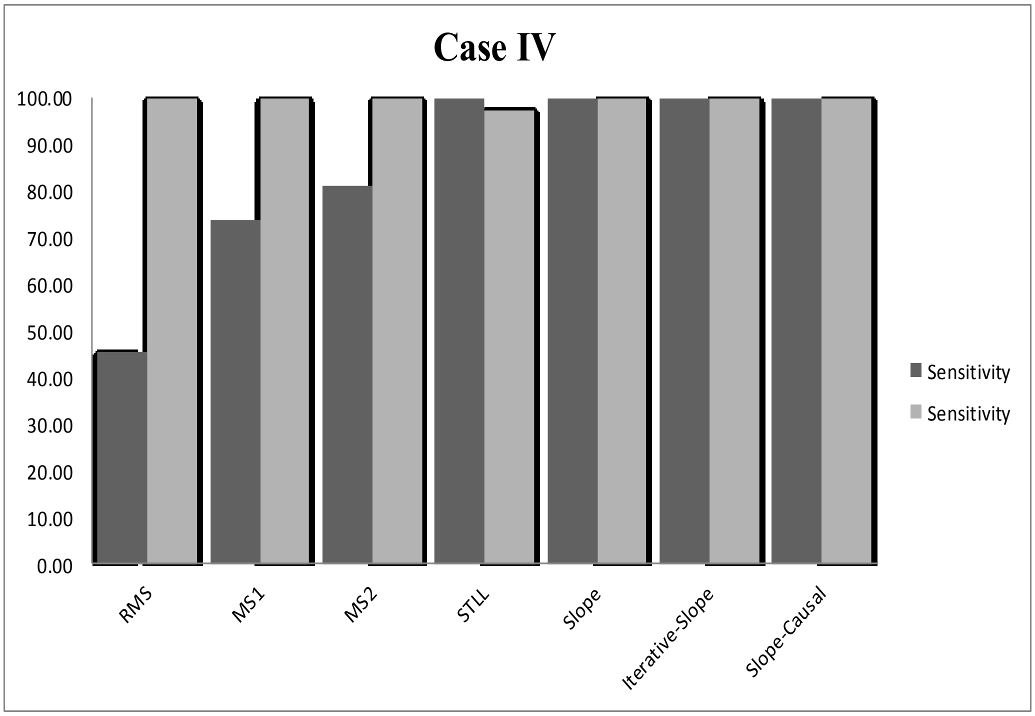

Figure 4.23 Comparison of detectors performance for simulated signal in Case IV

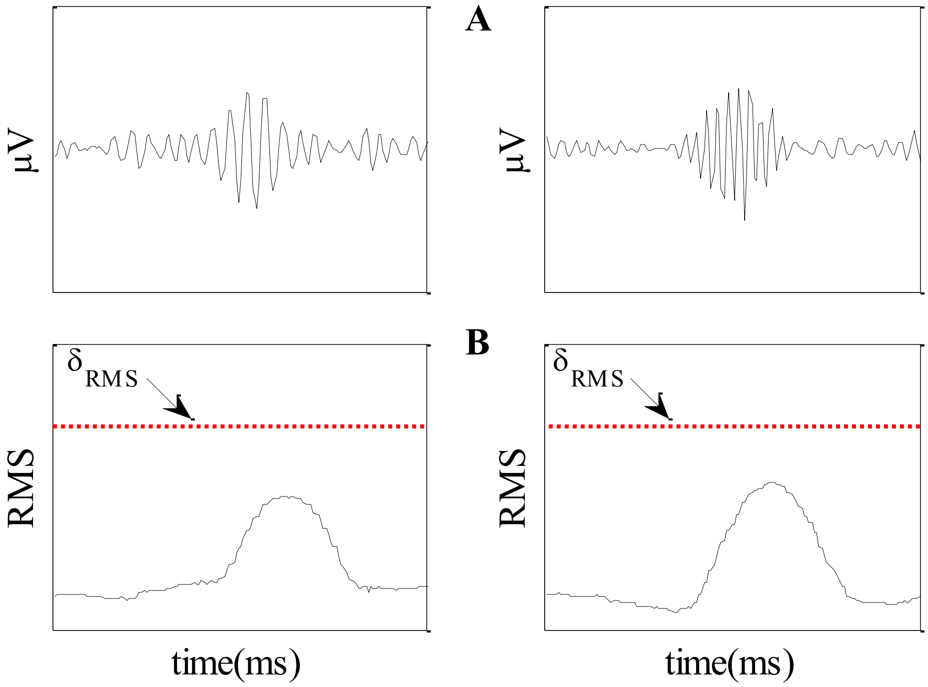

Figure 4.24 Two simulated events generated for Case IV that could not be detected by RMS, MS1, and MS2 detectors. **(A)** Simulated signals **(B)** RMS energy of signal. Detection threshold is shown in dashed red lines.

Since the HFO events in simulated data are known to be present at specific latencies, it is possible to objectively study the performance and achieve a better understanding of the automatic HFO detectors compared to real data analysis.

Four kinds of simulated signals, Cases I-IV, were generated and processed by all the detectors presented in Chapter 3. TP, FP and FN were determined to compute the sensitivity and specificity of the automatic HFO detectors. We presented a comparison of the performance of HFO detectors based on the energy of the EEG signal (RMS, MS1, MS2, STLL) as well as on the sharpness of half-waves of the EEG signals (Slope, Iterative-Slope, and Slope-Causal detectors). The main difference between these two types of detectors is highlighted in Cases III and IV, where the simulated EEG consists of HFO events at various SNRs mimicking the real-world scenario. In Cases I and II, where the HFO events are of similar SNR levels, all the detectors exhibited almost identical performance, while for the signals in Cases III and IV, the results obtained from the sharpness detectors are remarkably better. For instance, in Case IV, not only are the high amplitude interference events detected by these detectors, but also all the HFO events with low energy. Overall, in perfect conditions, the energy detectors perform well, but in more realistic Cases (i.e., III, IV), they do not work well, and the sharpness-based detectors perform better.

RMS method functions well for HFO events in Case I especially when the events are of high amplitude (SNR ≥ 15 dB); however, the performance of this detector deteriorates in Cases II, III, and IV. Clearly the proper choice of a threshold is the most important factor for an automatic detector. In this detector, the threshold is obtained from the entire length of the signal including background and HFO events. In signals with rare HFO events or with HFO events at identical SNR levels, considering the entire EEG signal for calculating the detection threshold does not make an important difference. However, the presence of a large number of HFO events, particularly at different SNRs across the entire length of the signals, increases the threshold value. So it is not surprising that the worst performance for this detector was reported for Case IV, where two strong interferences are present. Accordingly, due to the high value of detection threshold, no FP events are detected in the simulated signals; however, it is at the price of losing a large amount of TP events (See Figure 4.24).

MS1 and MS2 detectors, modified versions of the RMS detector, have identical performance in Cases I and II. In contrast to the RMS detector which uses the complete length of the data to compute the threshold, the detection thresholds, for the *MS1* and *MS2* methods, are computed in a per-epoch fashion which dynamically varies for each epoch. That is, although the presence of noise or any other artifacts may still increase the threshold in a given epoch, it will not affect the complete recording. This is the reason why the performance of these detectors is remarkably better than that of the RMS detectors. On the other hand, the performance of the MS1 and MS2 detectors for Cases III and IV are not as promising. The results get worse in Case IV when two high amplitude interferences are added to the simulated EEG. For these two Cases, the events at different SNR levels are present in the signal. Presence of high energy HFO events or any kind of interferences, artifacts and noise affect the threshold of the corresponding epochs which subsequently leads to FN events. However, similar to the RMS detector, the number of false positive events is still zero.

Among the energy-based detectors including RMS, MS1, MS2, and STLL, the STLL resulted in perfect sensitivity for Cases III and IV, but with some false positive detection reducing the specificity of the detector. Overall, the STLL detector performs well in almost all the simulated signals in term of sensitivity; however, due to the presence of FP events, the specificity of this method never reaches 100%.

As described in Chapter 3, the energy of each epoch is computed based on the distances between consequtive samples, and any sharp activies such as spikes or sharp waves increase the energy of the corresponding epochs. It is seen from Figure 4.22, small fluctuations in the signal would trigger the detector leading to FP detections. One might say that these FP events have smaller amplitudes compared to the FN events shown in Figure 4.18, but we should note that the threshold for this method is chosen for each epoch separaetly, and these segments have smaller threshold values.

All the proposed methods based on the sharpness of have-waves such as Slope, Iterative-Slope, and Slope-Causal detectors have a good performance for all cases, and the results are not dependent on the type or energy of the events. Their inherent detection characteristics are not influenced by the high-energy events or any interference. However, in Case I with ripples at SNR 10 dB, none of these methods could achieve 100% sensitivity. Figure 4.17 shows two examples of HFO events with SNR 10 dB, which the sharpness-based detectors failed to detect. The likely reason for the FN detections in Case I is the small number of oscillations in the simulated ripples. As described earlier, the number of oscillations plays an important role in the detection of HFO events in sharpness-based detectors. Therefore, if an event does not contain enough number of slopes of half-waves with the values greater than detection threshold, it is not detected by sharpness of half-waves based detectors. Nevertheless, the sensitivity could be increased by reducing the threshold value, but due to the trade-off between the sensitivity and specificity, there would be a reduction in the specificity.

In practice, however, the HFO events mostly fall under Cases III and IV in which the ripples and fast ripples with different SNR levels co-exist. The sensitivity and specificity of these detectors are 100 %. That is, the proposed methods detected all the simulated HFO events in these two Cases, with no false detections. Overall, as shown in Table 4.8 and Table 4.9, the proposed methods based on the sharpness of half-waves of signals perform better than the energy-based methods in terms of both sensitivity and specificity, with a significant improvement over the RMS method.

4.4 Summary

In this chapter, we have simulated different EEG signals with HFO events. We have considered almost all the possible conditions under which the HFO events are combined with the background signal. Methods presented in Chapter 3 including energy-based detectors and sharpness-based detectors have been tested with the simulated signals and the results have been presented. The RMS detector resulted in poor performance in terms of sensitivity in Cases II, III and IV, and this is due to the high detection threshold, computed from the full length of signal. This was more obvious in Case IV, where the signal was contaminated by two instants of strong interference. Compared to RMS method, MS1 and MS2 detectors showed better performance in terms of the sensitivity. These detectors functioned very well for signals in Cases I and II; however, their performance was not as promising for Cases III and IV. Overall, the performance of the RMS, MS1 and MS2 detectors degraded as the energy of the simulated HFO events changed from an event to the next event (Cases III and IV). The other energy-based detector, STLL, showed good sensitivity for signals in Cases III and IV, however with some false positive detection which degraded the specificity of this detector.

The results of the proposed methods (based on the sharpness of half-waves) have shown a significant improvement in the detection performance (both sensitivity and specificity) compared to the energy-based detectors, particularly compared to that of the RMS detector. Regardless of the energy of simulated events, the proposed methods functioned very well in all the cases. Their inherent detection characteristics are not influenced by the high energy events resulting in an excellent performance in terms of both the sensitivity and the specificity.

Chapter 5 . Performance of the Detectors Using Real Data

In Chapter 4, computer generated data was used to compare the performance of the automatic HFO algorithms. In this chapter, we will use real patient database to study the performance. This chapter is divided into three sections. Section 5.1 presents the real data description. Section 5.2 provides the results of applying the algorithms described in Chapter 3 on the real data of epileptic patients and Section 0 presents the clinical implications of HFO events for all patients.

5.1 Data Description

Data from six epileptic patients was selected for this study; however, two were excluded due to the reason of very low amplitude, or continuous artifacts. The IEEG was acquired by recording at a sampling rate of 1000 Hz. Depending on the reason for the recording (type and location of seizure), patients had different number of electrodes ranging from 50 to 100. For each patient, six bipolar channels, with a duration of 10 minutes, were generated as our database for the analysis in Section 5.2. Table 5.1 describes the patient database and the specification of the recording.

5.1.1 Data Conversion

In this study, review of the IEEG signals and visual HFO detection are performed using the Stellate Harmonie software (version 6.2e, Stellate Systems Inc., Montreal, Canada). This software, as a clinical software, allows easy and rapid review of multichannel recordings. On the other hand, the data processing, and algorithm development was carried out in MATLAB (R 2008b, Mathwork Inc., USA). To analyse the recorded data in MATLAB, the data in the Stellate Harmonie must be converted for compatibility with MATLAB environment. To handle this problem, the Stellate's MATLAB interface toolbox (mSigFileInterface) is used and signal files in the Stellate Harmonie Software were imported into MATLAB environment.

Table 5.1 Demographic electrophysiological data for 4 patients undergoing implantation studies. Abbreviation : A = Anterior, P = Posterior, T = Temporal, F = Frontal, M = Mesial , O = Occipital, R = right, L = Left, LL = Left Lateral, SF = Sub Frontal, D = Depth

Patient ID	Number of electrodes	Implanted Electrode Locations	Seizure Propagation Locations
BB1	6	Depth(2) : AD,PD Epidural(4) : FP, AT,MT,PT	AT, PT
CC2	8	Depth(6) : RA,RP, LA,LM,LP Epidural (2) : RL, LL	LLT, MT,PT
FF2	5	Depth(2) : AD, PD Epidural(3) : AT,MT,PT	AT,MT
II1	4	Epidural(4) : FP, TO, PT,SF	Neocortex, PT,TO

5.1.2 Electrodes and Localization

Sixty minutes of IEEG recording from each of four patients with medically intractable epilepsy undergoing continuous long-term EEG monitoring are analyzed. Each patient underwent implantation of two types of electrodes: intracranial clinical depth micro-electrodes and subdural electrodes (strips & grids). Each electrode is named with its type and location. Electrodes located in the left and right hemispheres were labeled with ‘L’ and ‘R’, respectively and multi-contacts depth electrodes were labeled with letter ‘D’ with deepest contact labeled as 1. For example, depth electrode group located in the right anterior part of the brain was labeled ‘RAD’ while the one placed in the left anterior part was labeled ‘LAD’.

Figure 5.1 shows the electrode implantation for one of the patients. As can be seen, two types of electrodes were used in this patient: two depth electrodes labeled ‘AD’ and ‘PD’, and four subdural electrodes labeled ‘AT’, ‘FP’, ‘PT’, and ‘MT’ (for Anterior-Temporal, Frontal-Parietal, Posterior-Temporal, and Mesial-Temporal, respectively).

5.1.3 Visual HFO Detection

As discussed in the previous chapters, to evaluate the performance of an automatic HFO detector, the detected events must be compared with a *Gold-Standard* that often corresponds to manually scored events by the human experts. In this study, the visual marking of HFO events in the IEEG was performed using an approach similar to the method introduced by Jirsch *et al* [24].

To detect an HFO event visually, the EEG display on the computer screen is split vertically into two sections. High pass filter with a cut-off frequency of 100 Hz is applied to the left section and a 250 Hz high pass filter to the right section. The time resolution is maximized to 1 sec/page in each section. An event is marked if there are at least 4 consecutive oscillations of sinusoid-like waves in left and right screens that are discernible from the background. The detected events were marked by their onset (the instant HFO event starts) and offset (the instant HFO event ends).

Applying the above strategy, the *"Gold Standard"* HFO events, were marked by an experienced EEG reviewer. That is, we assume that all HFO events marked by the reviewer are real HFO events. Overall, a total of 869 HFO events in four patients were identified. Table 5.2 lists the number of visually scored HFO events across the selected 6 bipolar cannels for each patient.

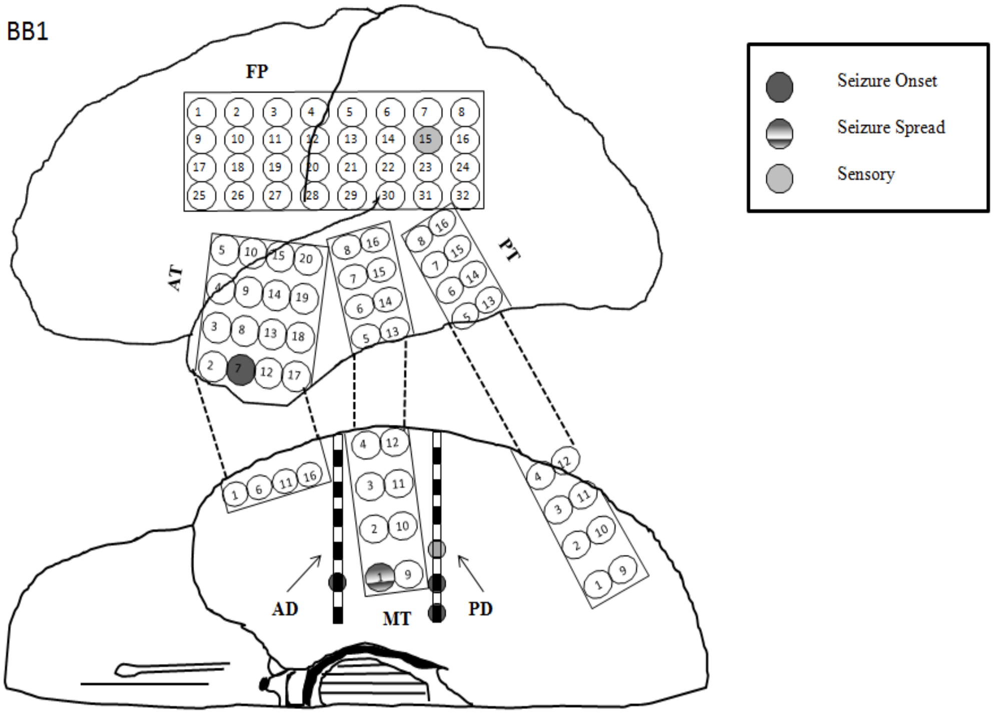

Figure 5.1 Electrode implantation on the brain of one the patients. Both types of electrodes, depth and subdural, were used in the patient.

5.2 Performance Evaluation

In all, twenty-four channels of EEG recordings with duration of 10 minutes (per channel) from 4 different patients were analyzed for the presence of HFO activity. The performance of automatic HFO detectors was compared against visually-scored HFO events. The detection thresholds for the proposed sharpness based methods were selected to be those used in Case IV from Chapter 4, which represents the most realistic scenario. Prior to performance evaluation of the automatic HFO detectors, all the detected events located within 40 ms of each other were clustered as a single HFO event. The choice of 40 ms corresponds to the 4 cycles of the smallest frequency content of the events (100 Hz).

Table 5.2 Number of the HFO events marked by the reviewer.

	Patient ID	**# HFO events**
1	BB1	320
2	CC2	110
3	FF2	91
4	II1	348
Total		**869**

An automatic detected event was defined to be a true positive (TP) if there was any overlap with the *Gold Standard* event; otherwise, it was considered to be a false positive (FP) detection. On the other hand, the manually-scored events that were not marked by the automatic HFO detectors were considered to be false negative (FN) or missed events. The performance of the detectors was evaluated using the same techniques as was done for the simulated data described in Chapter 4. That is, we used the sensitivity and specificity metrics. Following paragraphs present the performance results of the automatic HFO detectors using real data.

5.2.1 Results

The automatic detection results of all the algorithms for each patient are shown in Table 5.3. The bottom row of this table lists the average performance of each automatic HFO detector in terms of sensitivity and specificity for all the four patients. Figure 5.2 presents the average of sensitivity and specificity of the detectors across all patients.

Unlike the results for the simulated data, none of the automatic HFO detectors reported perfect performances in terms of sensitivity and specificity. MS2 detector reported the highest sensitivity for the real data (80.02%) followed by STLL (80.15%), MS1 (74.12%), Iterative-Slope (58.06%), Slope (56.54%), Slope-Causal (54.70%), and RMS (29.80%).

In terms of specificity, it is seen that the specificity of the three proposed methods based on the sharpness of the signals and the RMS detectors report the highest performance among all detectors. Slope-Causal, Slope, Iterative-Slope, and RMS detectors with specificity of 48.15%, 44.32%, 44.17%, and 40.53% result in a significantly improved performance over the STLL, MS1, and MS2 detectors with specificity of 14.57%, 22.39%, and 18.58%, respectively.

5.2.2 Discussion

The purpose of this section is to evaluate the performance of the automatic HFO detectors in terms of sensitivity and specificity with real data. We have given the results of the automatic HFO detectors for twenty-four channels from four patients in the previous sub-section.

Table 5.3 Detection results of the automatic HFO detectors for 4 patients. PID = patient ID, SN = Sensitivity, SP = Specificity

PID	Length (min)	RMS		MS1		MS2		STLL		Slope		Slope_dynamic		Slope_causal	
		SN (%)	SP (%)	SN (%)	SP (%)	SN (%)	SP (%)	SN (%)	SP (%)	SN (%)	SP (%)	SN (%)	SP (%)	SN (%)	SP (%)
BB1	60	14.46	58.02	72.31	47.76	77.54	37.84	85.23	12.94	46.15	73.17	46.46	72.60	46.77	76.38
CC2	60	68.18	40.32	74.55	12.75	90.91	11.96	100.00	5.16	77.27	54.84	75.45	54.61	74.55	53.59
FF2	60	16.48	25.00	85.71	10.16	93.41	7.76	89.01	3.77	56.04	19.77	65.93	20.91	58.24	32.72
II1	60	19.83	38.76	52.30	50.00	60.92	20.27	68.97	11.49	45.98	29.52	43.68	28.57	38.51	29.91
TOTAL		29.74	40.53	71.22	30.17	80.69	19.46	85.80	8.34	56.36	44.32	57.88	44.17	54.52	48.15

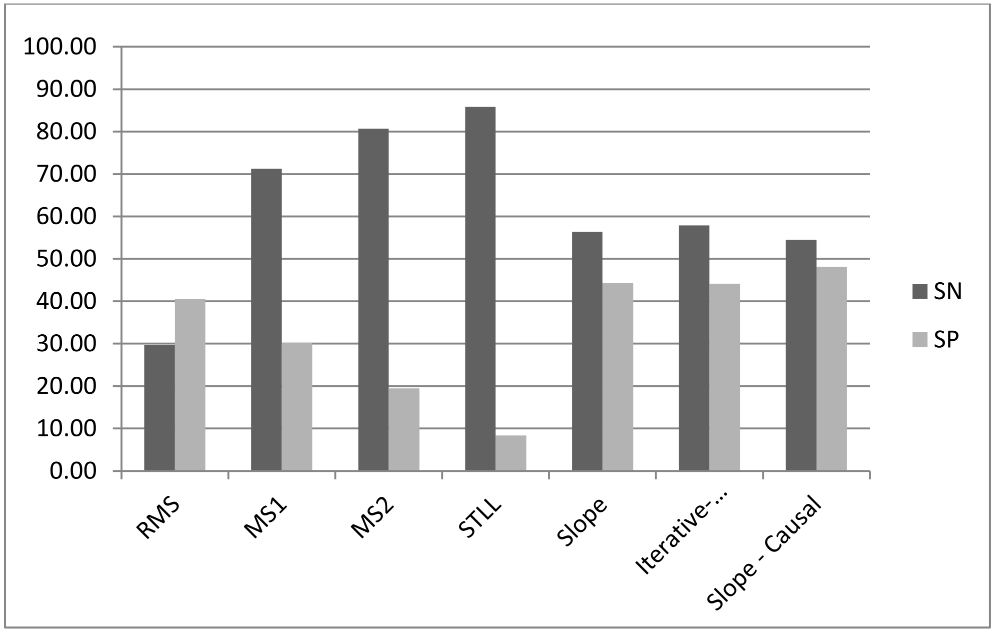

Figure 5.2 Comparison of sensitivity and specificity of the automatic detectors.

The RMS detector reported the highest specificity and lowest sensitivity amongst all the energy-based detectors. The main reason for this is due to the high threshold calculated using the full length of the signal. The presence of any type of transient interference such as high-energy HFOs, artifacts, or noises, tends to increase the threshold. The higher threshold leads to less number of detections (lower sensitivity) and consequently, the number of FP events would also be remarkably fewer resulting in a higher specificity. This was particularly obvious in patient BB1.

As seen from Table 5.3, RMS detector reported the worst sensitivity for patients BB1 and FF2. Investigation of the detections revealed that some sections of the recording for these patients were contaminated with artifacts, noises and high-energy interferences. These noisy segments affected the threshold and consequently, the performance of the RMS detector. Therefore, in order to evaluate the performance of the RMS detector under normal conditions for these two patients, we decided to remove the contaminated segments from the IEEG data and re-evaluate the performances of all the automatic HFO detectors. These contaminated segments were visually identified by the reviewer and excluded from processing. The resulting performance metrics obtained from all the detectors are shown in Table 5.4. For comparative assessment, we also included the results of patients CC2 and II1. Figure 5.3 shows the averages of the sensitivity and specificity of all the detectors. It can be seen that by removing the noisy segments from IEEG of patients BB1 and FF2, the performance of the RMS detector improved significantly, as anticipated. The reason is that after excluding noise and high-energy interferences, the detection threshold was reduced leading to an increased number of detections and accordingly a better performance.

As expected, compared to MS1, MS2 resulted in a larger number of detections (hence, better sensitivity, but poorer specificity). The reason is that in MS2, the detection threshold is updated every 10 seconds, while in MS1 it is updated every one minute. That is, the presence of high-energy events or interferences in a small segment of an epoch increases the threshold for the corresponding epoch, consequently leading to a lesser number of detections, whereas in MS2, the impact of these events is removed by the sliding window applied in this method resulting in a larger number of detections, thus leading to a higher sensitivity and lower specificity. In the future, the performance of these detectors may be improved by selecting more appropriate thresholds or by applying post-processing steps such as counting the number of peaks or ripples in the detected events.

The STLL detector reported a very good sensitivity among all the HFO detectors; however it performed very poorly in terms of the specificity. In this detector, the energy of the signal is obtained by Equation (3.5). This type of energy is highly sensitive to the changes in the IEEG amplitude, and the energy of the signal increases with any spurious fluctuation. This results in numerous TP and FP detections increasing the sensitivity while reducing the specificity of the detector. After excluding noisy segments in patients BB1 and FF2, the performance of the STLL detector also improved in both the aspects (namely, sensitivity and specificity); nevertheless, the specificity of this detector is still far inferior to all the other detectors. That is, by removing the noisy sections, this detector did not report a significant reduction in the number of FP events. Selecting a more appropriate threshold may enhance the performance of this detector, but in this study we followed the same approach applied in the original work [55].

Table 5.4 Detection results of the automatic HFO detectors for 4 patients after removing artifacts and high energy interferences PID = patient ID, SN = Sensitivity, SP = Specificity

PID	**Length (min)**	**RMS**		**MS1**		**MS2**		**STLL**		**Slope**		**Slope_dynamic**		**Slope_causal**	
		SN (%)	**SP (%)**	**SN (%)**	**SP (%)**	**SN (%)**	**SP (%)**	**SN (%)**	**SP (%)**	**SN (%)**	**SP (%)**	**SN (%)**	**SP (%)**	**SN (%)**	**SP (%)**
BB1	44.04	31.35	91.35	74.26	51.14	74.92	46.14	86.47	14.67	50.83	78.97	50.83	79.38	49.83	80.32
CC2	60	68.18	40.32	74.55	12.75	90.91	11.96	100.00	5.16	83.64	56.79	77.27	52.15	79.09	53.05
FF2	58.02	73.63	42.41	92.31	10.53	93.41	7.99	95.60	4.00	69.23	26.81	73.63	28.63	69.23	30.88
II1	60	19.83	38.76	52.30	21.29	60.92	20.27	68.97	11.49	45.98	29.52	43.68	28.57	38.51	29.91
TOTAL		48.25	53.21	73.35	23.93	80.04	21.59	87.76	8.83	62.42	48.02	61.35	47.18	59.17	48.54

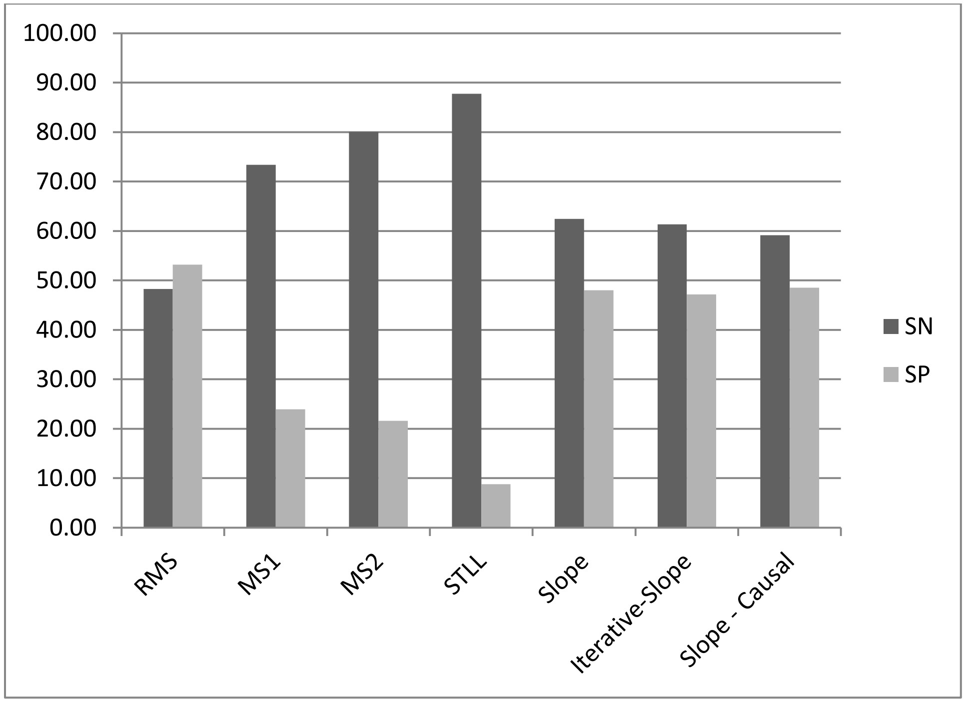

Figure 5.3 Comparison of sensitivity and specificity of the automatic detectors for signals after removing artifacts.

Overall, one of the main drawbacks of the above energy-based detectors is that they are very sensitive to any sharp transient. Based on the definition of the root mean square and short-time line length, the energy of the signal is directly proportional to the amplitude of the signal. That is, as the amplitude increases, the energy of the signal increases. Spikes and sharp-waves have larger amplitudes compared to the background activity. Consequently, the sharp activity is easily detected by these detectors and marked as HFO events. This increases the number of FP events yielding poor performance in terms of specificity. For such detectors, if human verification is required, reviewers must spend huge amounts of time to review the detected events and reject a large number of FP detections, making this process as tedious as the visual detection method.

Figure 5.4 illustrates some examples of false positive and true positive events from patient BB1 by energy-based detectors. As seen from this figure, sharp activities are easily detected by the energy–based detectors.

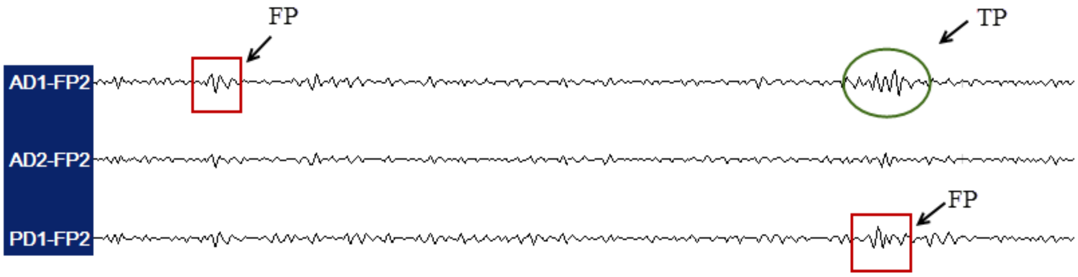

Figure 5.4 Some examples of TP and FP detections by energy-based detectors in patient BB1.

In contrast to the energy-based detectors, the proposed detectors based on the sharpness of the signals reported almost identical sensitivity and specificity for signals regardless of the presence of artifacts and high-energy interferences. That is, the performance of these proposed systems did not deteriorate because of the presence of high-energy interferences or artifacts. This is particularly evident in Patient BB1 and FF2.

All the sharpness-based detectors performed almost identically, and epoch length did not make any significant impact on the performance of these detectors. Nevertheless, the Iterative-Slope reported a slightly better performance, and this is due to the iterative approach applied for this detector.

There are several probable reasons for the proposed detectors to result in false detections. First reason is the presence of periodic low-energy high-frequency events in real IEEG signals. As described in Chapter 3, unlike energy-based detectors, the sharpness-based detectors focus on both the duration and the amplitude characteristics of the signal. Consequently, sharpness-based detectors detect not only high-amplitude events but also fast low-energy activities that are discernible from the background signal by their rhythm. However, it is worth emphasizing that such short-amplitude activities were not identified by the reviewer as HFO events leading to FP being reported by sharpness-based detectors. Figure 5.5 shows some examples of the low-energy rhythmic activity detected by the sharpness-based detectors. Due to the lack of knowledge and common agreement about what exactly constitutes an HFO event, it is likely that these rhythmic short-amplitude events may be, in fact, real HFO activities. If this hypothesis proves to be accurate with a larger dataset, it is fair to claim that sharpness-based detectors remarkably outperform the energy-based detectors.

The second reason is due to the approach that was applied for half-wave decomposition. In this study, half-waves have been defined as segments of signals located between two adjacent extrema regardless of their lengths. The presence of very fast low amplitude signals on some of the sharp activities such as spikes and sharp-waves or mixed frequency activities results in FP detections. Some examples of these events are shown in Figure 5.5. Although the half-waves of these events are sharp, their amplitude was not high enough to be scored as real HFO events by the reviewer.

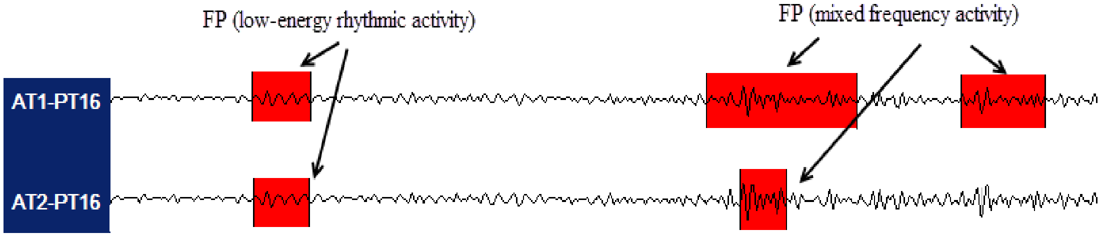

Figure 5.5 Some FP detection by Sharpness-based detectors (low energy fast activities and mixed frequency activities) from patient FF2.

On the other hand, several reasons can account for not having perfect sensitivity for the sharpness-based detectors. First probable reason is the detection threshold used for these detectors. Investigation of false negative detections revealed that, although some of the visually scored events were discernible from the background signals, they did not have enough sharpness to exceed the threshold, and hence were not detected as HFO events by the proposed detectors. Some of the examples of these events are shown in Figure 5.6. As can be seen, these events are relatively discernible from the background but due to their smooth slopes, sharpness-based detectors did not detect them as real HFO events. Further investigations are required to verify whether these events are real HFO events or not. If the former is true, setting a more appropriate threshold may improve the performance of these detectors.

Another likely reason is due to the "*Gold Standard*" events marked by the reviewer. Although attempts were made to maintain consistency in scoring HFOs, the visual inspection is a tiresome process which cannot be free of subjectivity. It is probable that some of the sharp activities (having less than 4 oscillations) have been scored as real HFOs. However, the sharpness-based detectors rejected these events and did not detect them as HFOs. This resulted in fewer number of matches to the manual detections.

Some examples of these events are shown in Figure 5.7. It is seen that these manually-scored events do not have 4 oscillations as defined for the real HFO, but have been marked by the reviewer. For most of the HFO detection methods, sharp activities and physiological high frequency artifacts such as electromyograph (EMG) are the main reasons causing false detections.

For the sharpness-based methods, although these activities may be detected as HFO events, they are less likely to cause deterioration in the performance of the detectors. Therefore, compared to the energy-based detectors, the sharpness-based methods lower the false detection rate. Moreover, the comparison between the energy-based and sharpness-based detectors showed a superior accuracy of the latter detectors in the sense that sensitivity and specificity were balanced over all data sets indicating the robustness of these detectors.

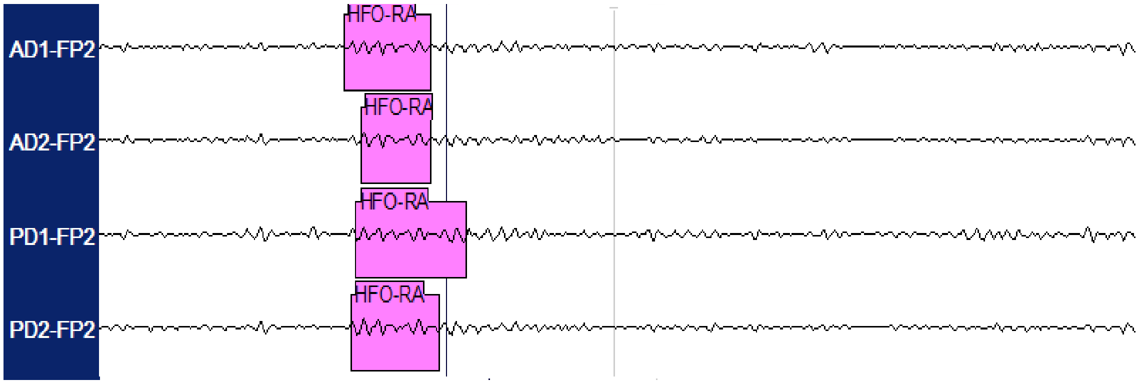

Figure 5.6 Some examples of visually scored events from patient BB, shown in pink, that were failed to detect by sharpness-based detectors.

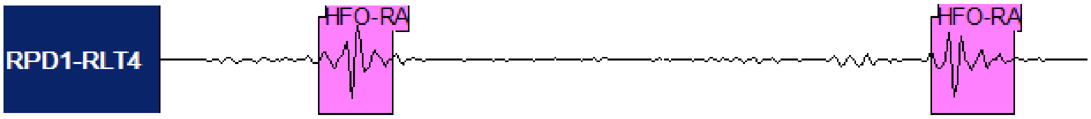

Figure 5.7 Two examples of visually scored events with less than 4 oscillations that were not detected by sharpness-based detectors.

5.3 Clinical implication of HFOs in Epilepsy

Thus far, we have compared the performance of seven automatic HFO detectors on 24 channels from four patients with the visually-scored events by a reviewer.

Literature has reported a possible relationship between HFOs and Seizure Onset Zone (SOZ) as well as between HFOs and Seizure Spread Zone (SSZ). In this study, SOZ and SSZ for all the patients were defined by the clinicians in their routine practice. In patients BB1 and FF2 the onset was unilateral temporal; in patient CC2, the onset was bilateral temporal; and in patient II1, the onset was unilateral neocortical. In three of the four patients, depending on the type and location of the epilepsy, the relevant brain tissue has been surgically resected based on the normal clinical assessment. The idea, here, is to see if the frequency of occurrence of the HFO events has any relationship to epilepsy and if they point to the same areas that were identified in clinical assessments.

In this section, the results of the detectors are not compared with the visually-scored events, but rather we study the clinical implication of the HFO events. In addition, the IEEG signals of the patients did not undergo the pre-evaluation step to exclude the noisy segments, such as high energy interference and artifacts. Therefore, it was absolutely crucial to select a robust automatic HFO detector that was capable of performing with the minimum failure rate under all conditions. That is, the selected detector should maintain the balance between sensitivity and specificity while keeping the former high, regardless of the presence of any artifacts or interference.

The energy-based detectors have good sensitivity, however, with extremely poor specificity. On the other hand, the sharpness-based detectors exhibited almost similar performance in all the patients regardless of the type of signals. Hence, we decided to choose one of the proposed sharpness-based methods for this study. Since the *Iterative-Slope* method exhibited the best performance among the other sharpness-based detectors, it was selected to study the clinical implication of the HFO events. In total, two hundred and eighty six IEEG channels from four patients were analyzed for the presence of HFO activity. The analysis was performed in referential montage. In this study, we treated the ripple and fast ripple events separately.

5.3.1 HFO analysis

To individually detect ripples and fast ripples in the IEEG signals, we need two different filters. A band pass filter with cut-off frequencies F_{cL} = 100 Hz and F_{cH} = 250 Hz for ripples and a high pass filter with a cut-off frequency F_c = 250 Hz for fast ripples. *Iterative-Slope* detector was applied to the filtered data for all the channels for each of the four patients. Table 5.5 lists the number of the recording sites as well as the numbers of detected ripples and fast ripples per patient. From 286 recording sites, a total number 13060 ripples and 5447 fast ripples were automatically detected by the *Iterative-Slope* detector. The number of HFO events, ripples and fast ripples, were mapped to the respective electrode positions. Figure 5.8 to 5.16 show the spatial distribution of the automatic detected ripples and fast ripples for patients BB1, CC2, FF2, and II1, respectively. The color bar beside each figure indicates the range of the number of detected HFO events for each patient. That is, the channel labels colored by red have the greatest amount of HFO activity compared to those with blue color. Note that the spatial distribution mapping was scaled by the minimum and maximum number of HFO events in each patient.

Table 5.5 Total number of recording sites and detected HFO events for each patient.

	Patient ID	Number of Channels	Number of detected Ripples	Number of detected Fast ripples
1	BB1	96	3436	1003
2	CC2	50	1714	674
3	FF2	60	2820	1906
4	II1	80	5090	1864
Total		**286**	**13060**	**5447**

Patient BB1

In patient BB1 with temporal lobe epilepsy, both types of electrodes (depth and grids) were implanted on left side of the brain. After mapping the detected events on the recording sites of this patient, we discovered that the highest ripple and fast ripple activity were observed in the electrode PT1 (posterior temporal lobe) located in the normal tissue and there appeared to be no correlation between HFO activity and SOZ or SSZ. Reviewing individual detections of PT1 revealed that most of the detected events had extremely large amplitudes (~ 4500 μV), which were unusual. The likely reason for this may be the presence of artifacts which can be either physiological such as EMG or ECG or non-physiological. Since in this study we have scaled the color bar based on the minimum and maximum number of detected events per patient, the large number of detected HFO events in one channel dominate the results of the other channels.

Therefore, to obtain a better topographic distribution of both types of events for the patient BB1, we excluded the HFOs of this particular channel and rescaled the data for the remaining channels. The topographic distributions of ripples and fast ripples for patient BB1 are shown in Figure 5.8 and 5.9, respectively. As expected, a large number of HFO activity (ripples and fast ripples) are observed in the deepest parts of the depth electrodes in hippocampal structures such as AD1-2, and PD1-2 that were located in seizure onset zone indicating a good correlation between the HFO activity and seizure-generating tissue.

(a) <u>Ripples</u>

High rate of ripples are found in the normal regions, particularly in the Posterior Temporal structures and somatosensory cortex structures such as FP23. Based on the previous studies (discussed in Chapter 1), it is indeed possible to record ripples from neocortex structures of the human brain; therefore, findings of ripples in somatosensory cortex do not conflict with the previous studies. On the other hand, our finding is also in accordance with the recent study [81] in a sense that normal ripples are likely to be found in occipital lobe structures of human's brain.

(b) <u>Fast ripples</u>

Consistent with the previous studies, fast ripples appear to be more localized than ripples and the rate of its occurrence is well correlated with the SOZ. There are some electrodes located in the normal tissue (somatosensory structure) with a large number of fast ripples such as FP7, 14, 15, and 23. The fast ripples in these regions could be either pathological or normal. Similar to ripples, fast ripples may be present in the somatosensory cortex under normal condition and these tissue are located in this region.

In this patient, the SOZ and SSZ regions and some of the Anterior-Temporal structures of the brain have been resected as shown in dashed red boxes of Figure 5.8 and 5.9. The regions with a high rate of HFO activity in somatosensory cortex remained intact. These decisions were made based on the routine clinical assessment that does not include the HFO analysis. Post-surgery follow-up showed that this patient is seizure free and does not suffer from epilepsy any longer. That is, the regions with high rate of FR in somatosensory cortex are not pathological.

Patient CC2

In patient CC2, electrodes were implanted bilaterally: five depth electrode groups (RAD, RPD, LAD, LMD, LPD), two small grid electrode groups were located in the right and left of the temporal lobe structures (RLT and LLT) and one grid electrode (RPT) was located in the right posterior temporal lobe.

(a) Ripples

Figure 5.10 shows the topographic distribution of ripples for patient CC2. In contrast to patient BB1, in this patient, ripple activity correlates well with the SOZ regions. The ripples were more concentrated on the electrodes located in SOZ in the RPT and LLT strips, especially those contacts corresponding to SOZ areas. This supports a good agreement between SOZ and ripple activity.

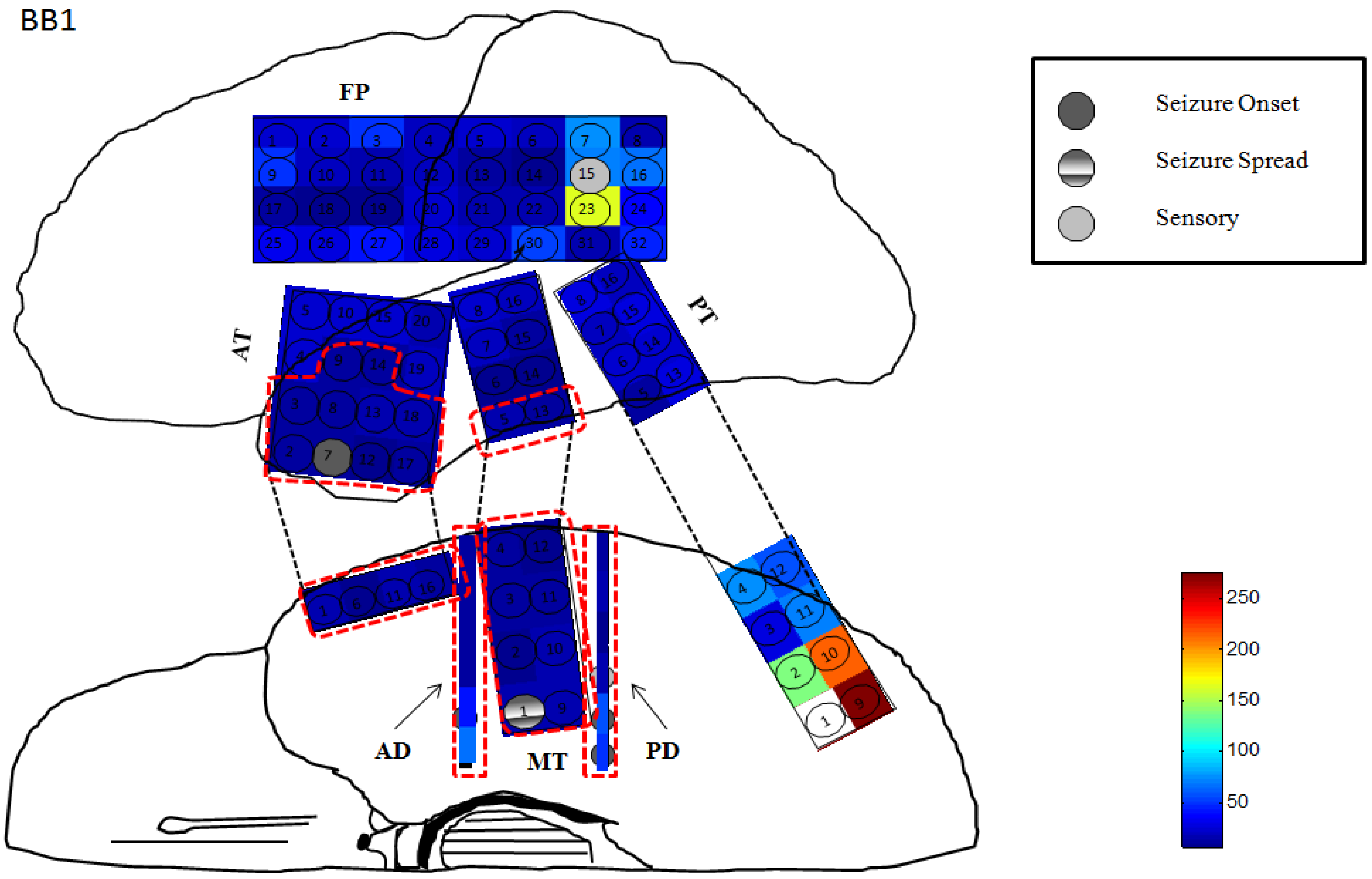

Figure 5.8 Topographic distribution of spontaneous ripples recorded at the electrode positions for patient BB1. The color bar indicates the number of detected ripples. Dashed red box indicates the resected area by surgeons. Electrodes abbreviations: AT=Anterior Temporal, MT= Mesial Temporal, PT= Posterior Temporal, FP = Frontal/Parietal, AD= Anterior Depth, PD=Posterior Depth

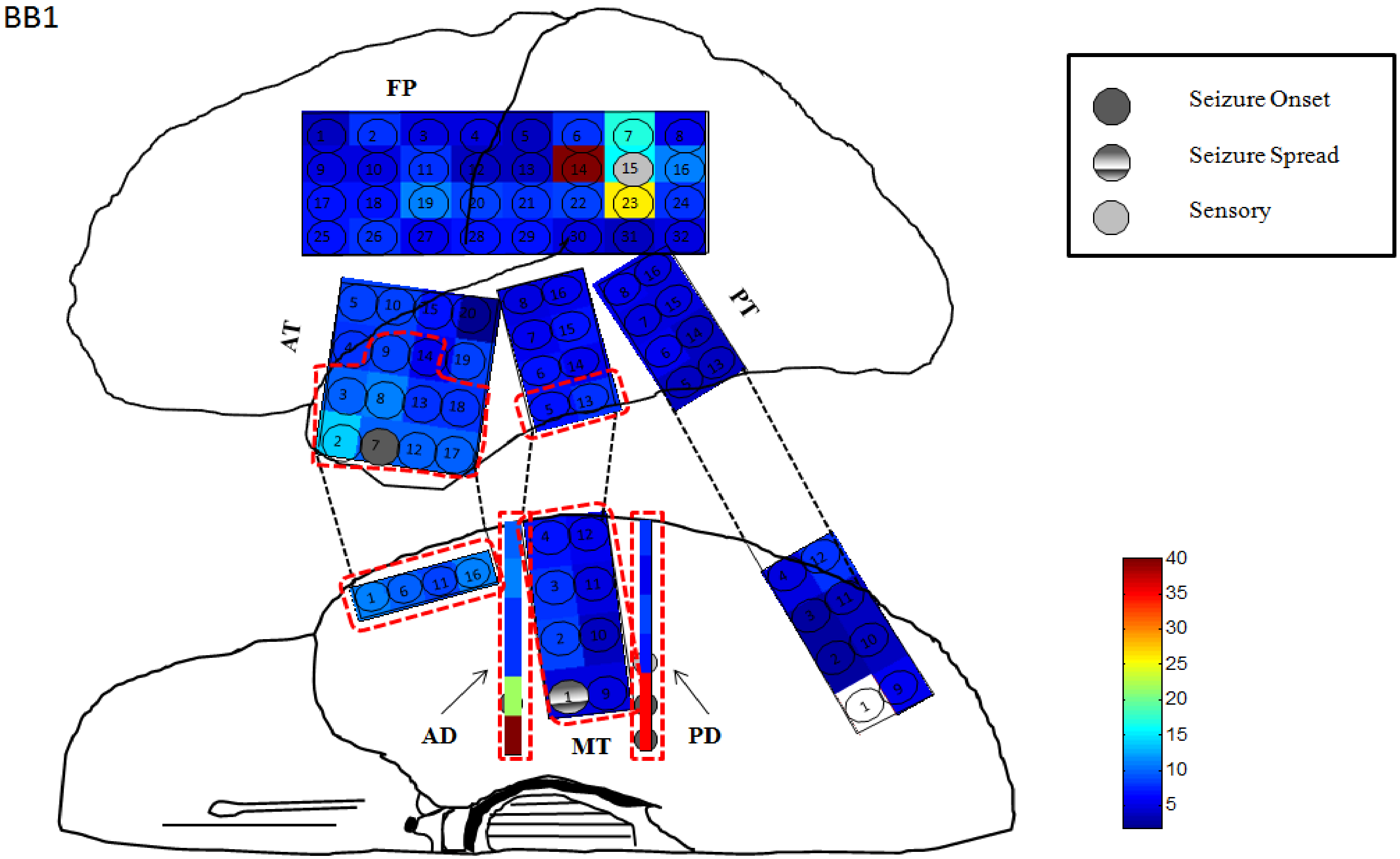

Figure 5.9 Topographic distribution of spontaneous fast ripples recorded at the electrode positions for patient BB1. The color bar indicates the number of detected fast ripples. Dashed red box indicates the resected area by surgeons. Electrodes abbreviations: AT=Anterior Temporal, MT= Mesial Temporal, PT= Posterior Temporal, FP = Frontal/Parietal, AD= Anterior Depth, PD=Posterior Depth

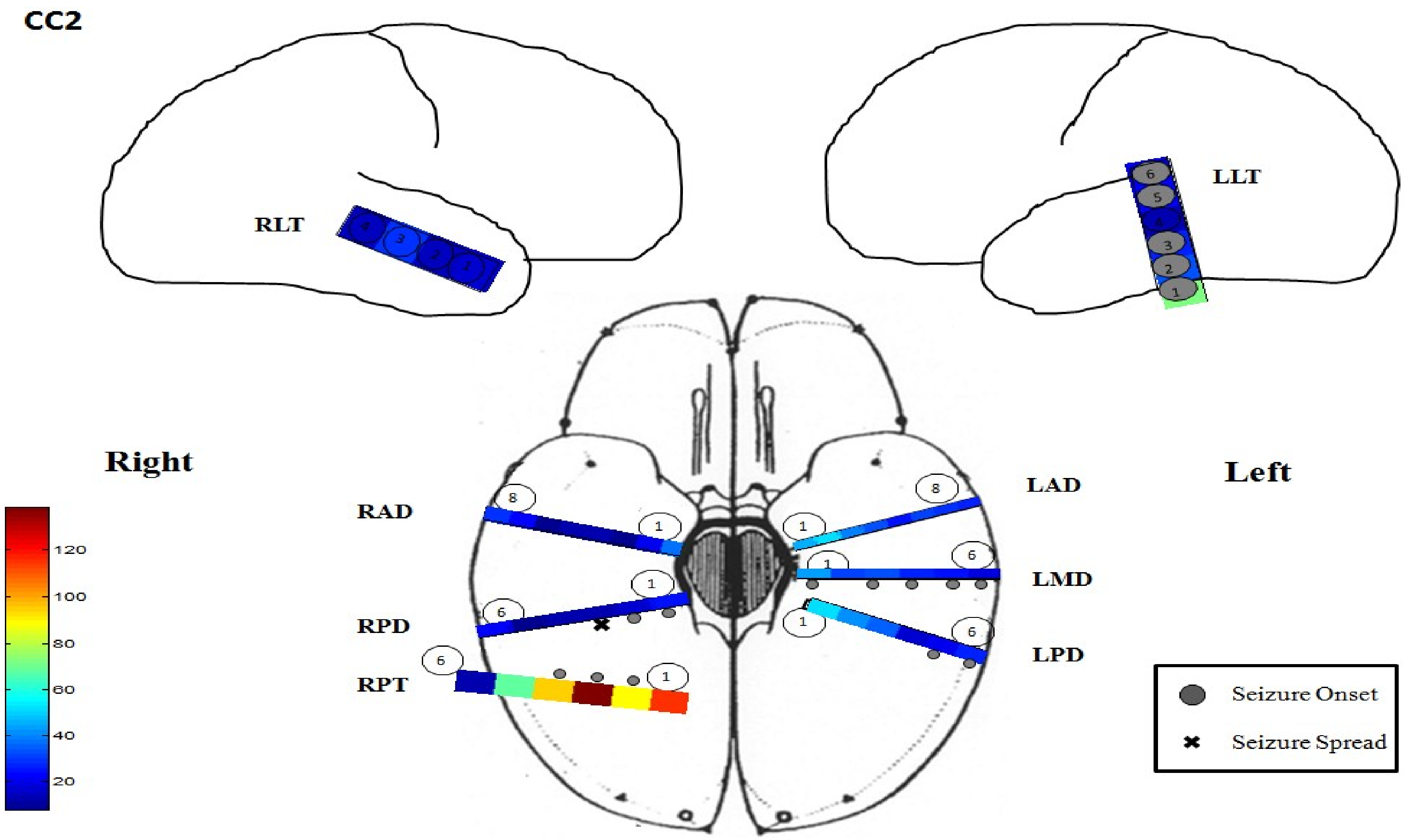

Figure 5.10 Topographic distribution of spontaneous ripples recorded at the electrodes positions for patient CC2. The color bar indicates the number of the detected ripples. **Electrode Abbreviations**: RLT=Right lateral Temporal, LLT= Left Lateral Temporal, RPT= Right Posterior Temporal, LAD = Left Anterior Depth, RAD= Right Anterior Depth, RPD=Right Posterior Depth, LMD = Left Mesial Depth, LPD = Left Posterior Depth

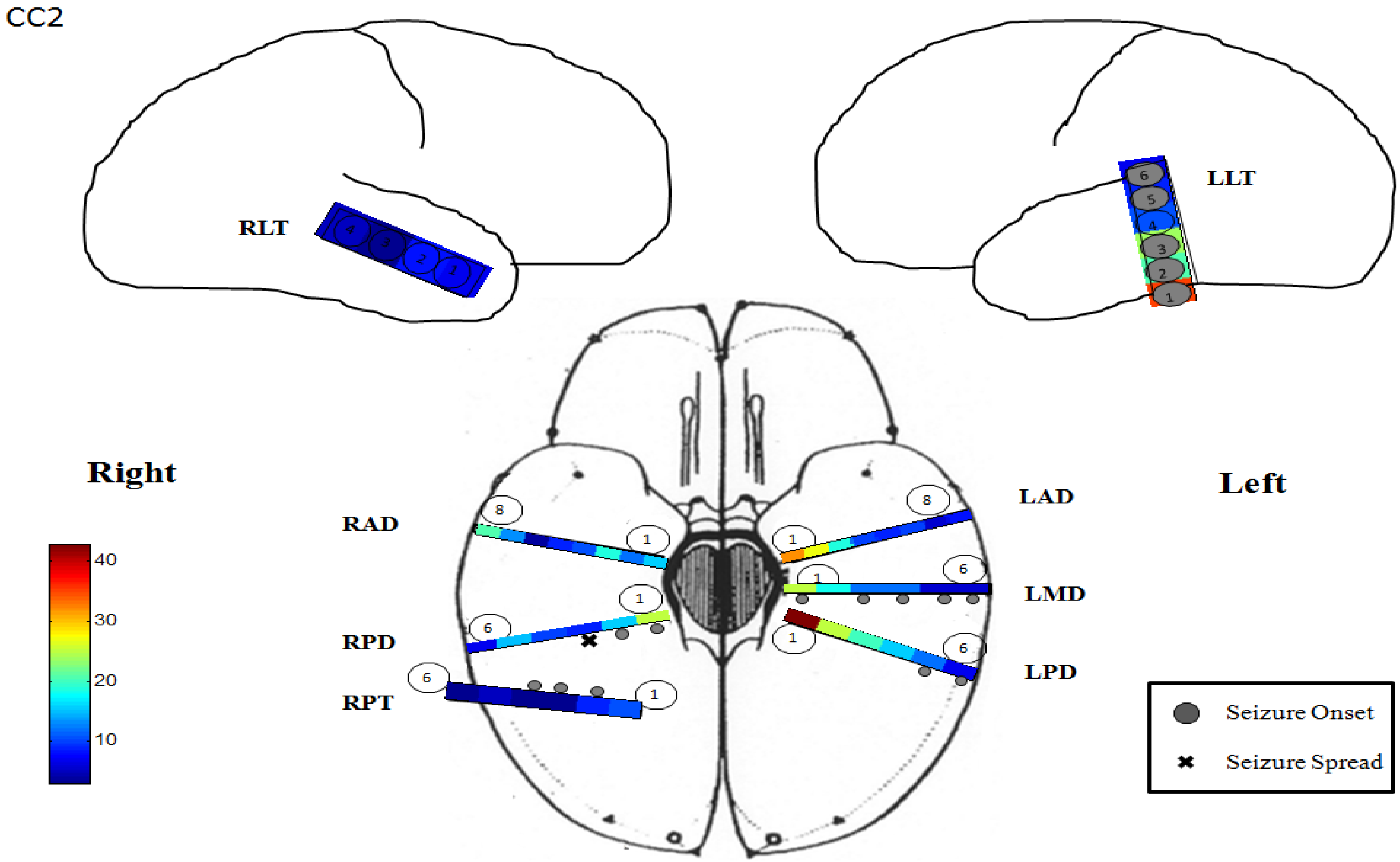

Figure 5.11 Topographic distribution of spontaneous fast ripples recorded at the electrodes positions for patient CC2. The color bar indicates the number of the detected fast ripples. **Electrode Abbreviations**: RLT=Right lateral Temporal, LLT= Left Lateral Temporal, RPT= Right Posterior Temporal, LAD = Left Anterior Depth, RAD= Right Anterior Depth, RPD=Right Posterior Depth, LMD = Left Mesial Depth, LPD = Left Posterior Depth.

(b) Fast ripple

As seen from Figure 5.11, similar to our findings for patient BB1, fast ripples appear to be more localized than ripples in the SOZ indicating a good correlation between the rate of occurrence of fast ripples and the SOZ. This is more prominent in LLT, LMD, and RPD electrodes. Both sides of the hippocampal regions demonstrated a higher number of fast ripples indicating epileptic tissue, particularly the deeper contacts (1-3), which is consistent with bilateral seizures. However, the rate of occurrence of fast ripples in the depth electrodes located in the hippocampal structure, such as LAD1-3, LPD1-4 and RAD1-3, is also high. This may support the idea that these structures are capable of generating seizures.

Normal clinical assessment revealed that this patient had bilateral seizure onset zone, left and right hippocampal structures. Due to the fact that this patient suffers from bilateral epilepsy, he/she did not undergo the surgical procedure. The surgery for this particular patient may result in other functional deficit to justify the benefits of being seizure-free.

Patient FF2

Just as in BB1, patient FF2 was implanted unilaterally in the left side of the temporal lobe. Grids and depth electrodes were applied to record the IEEG signal. After mapping the number of fast ripples to the recording site of this patient, we surprisingly found that the largest number of fast ripples for this patient corresponded to MT16 electrode located in the normal tissue. Reviewing the detected fast ripples in this particular channel revealed that this channel was highly contaminated with artifacts, possibly non-physiological such as power line harmonics. Therefore, to obtain a better topographic distribution of the fast ripples for this patient, we excluded the detected fast ripples of this channel and rescaled the data for the remaining channels. Spatial distribution of the automatic detected ripples and fast ripples are illustrated in Figure 5.12 and 5.13.

(a) **Ripple**

The results show that the ripples are discretely localized through all temporal lobe structures, especially in the anterior and mesial temporal regions (Figure 5.12). A good correlation is observed between the SOZ and the rate of occurrence of the ripples. The presence of ripple activity in the normal tissue such as mesial temporal structure (MT) are consistent with the previous researches [24], in the sense that ripples are likely to be found in the epileptogenic and non-epileptogenic temporal lobe. Depth electrodes in the hippocampal region, particularly the first two contacts, show the larger number of ripples compared to subdural electrodes.

(b) **Fast ripple**

Seizure generating tissue such as anterior and mesial temporal structure showed a high rate of fast ripples activities. Nevertheless, a high rate was also observed in the depth electrodes corresponding to hippocampal regions and MT5 electrode located in the normal tissues. Brain tissue located in the hippocampal structures, near or inside the SOZ such as AD, PD, AT1-15, MT1-5, and MT9-12, were all resected. However, some tissue with large number of fast ripples in posterior temporal lobe remained intact.

Based on the previous studies, fast ripples have never been recorded in the hippocampal and parahippocampal structures of the normal brain [3, 25, 26, 28, 48]. Our findings support the idea that the regions with high rate of fast ripples may be capable of generating seizures. The surgery outcome for this patient is not known to us and post-surgery follow-up is required to see whether the patient remained seizure free. If the patient was not completely seizure free, it is possible that the HFO analysis can provide additional information about the seizure generation.

Patient II1

Topographic distribution of ripples and fast ripples for patient II1 is shown in Figure 5.15 and Figure 5.16. In this patient, there were only subdural electrodes (Grids and strips) implanted in the right side of the brain and no depth electrodes were applied to record the IEEG signals. In contrast to other patients with temporal lobe epilepsy, the seizure onset zones for patient II1 were solely localized in the neocortex structure indicating neocortical epilepsy. Neocortical epilepsy differs from other kinds of epilepsy because it can be poorly localized and there is no clearly defined area from which seizures originate. In this patient, however, the seizure onset areas have been marked in the parietal lobe of the patient (solid gray circles in Figure 5.15 and 5.16).

(a) Ripple

Based on the results of Figure 5.15, the correlation between ripple activity and SOZ or SSZ is not very good. Ripples are not limited to SOZ or SSZ electrodes but present in all brain regions (epileptogenic and non-epileptogenic tissues). As seen from Figure 5.15, electrodes in SOZ in the neocortical structure under the electrodes FP11-14, FP19-22, FP27-28 (gray circles) do not show a higher rate of ripple activity compared to those located in normal tissue or SSZ.

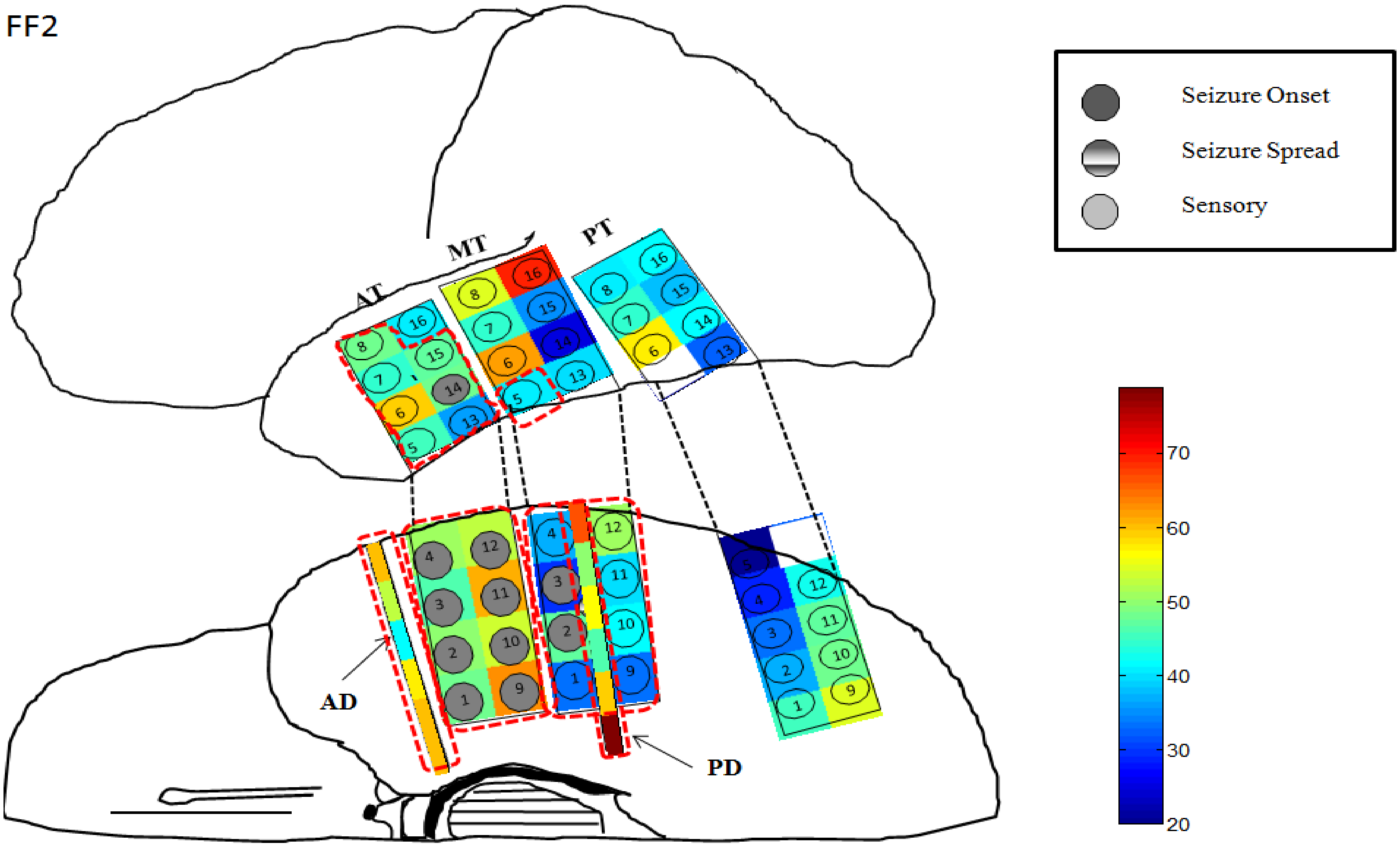

Figure 5.12 Topographic distribution of spontaneous ripples recorded at the electrodes positions for patient FF2. The color bar indicates the number of the detected ripples. Dashed red box indicates the resected area by surgeons. **Electrodes abbreviations**: AT=Anterior Temporal, MT= Mesial Temporal, PT= Posterior Temporal, AD= Anterior Depth, PD=Posterior Depth

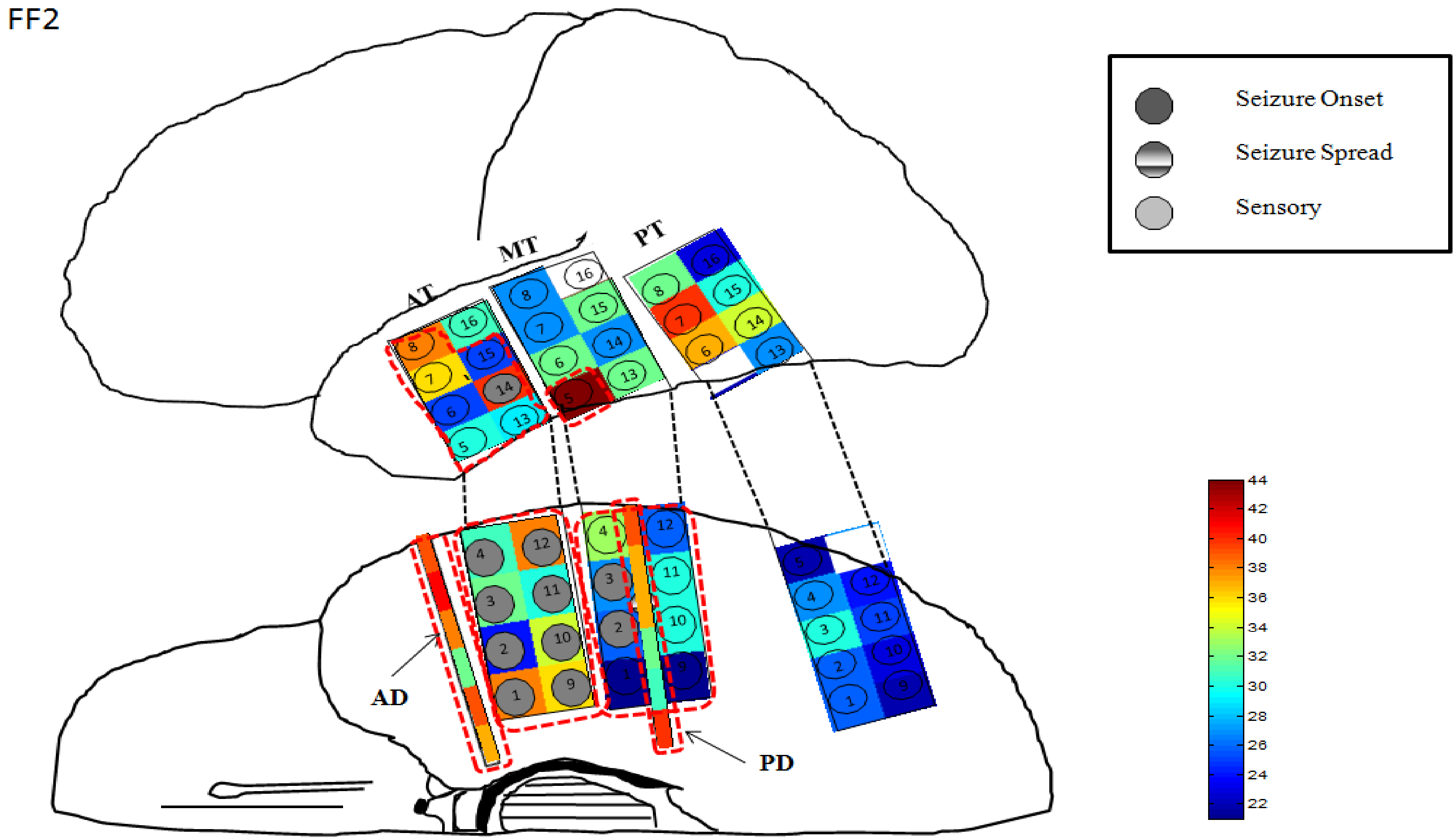

Figure 5.13 Topographic distribution of spontaneous fast ripples recorded at the electrodes positions for patient FF2 after excluding the detected fast ripples for electrode MT16. The color bar indicates the number of the detected fast ripple. Dashed red box indicates the resected area by surgeons. **Electrodes abbreviations**: AT=Anterior Temporal, MT= Mesial Temporal, PT= Posterior Temporal, AD= Anterior Depth, PD=Posterior Depth

(b) Fast ripple

On the other hand, based on our findings, there is a relatively good correlation between the SOZ, SSZ and rate of occurrence of fast ripples; however, fast ripples are not uniquely localized in these tissue and their high rate of is also seen in the normal tissue. After reviewing the detected events, we consider two possibilities for the disagreement between fast ripples and SOZ or SSZ.

First, we found that the IEEG signal of this patient was contaminated with power line harmonics in the range of 300 and 420 Hz and it is possible that the automatic detector detected these activities as fast ripples, thus accounting for a large number of false positive events. An example of false positive detected event from this patient is shown in Figure 5.14. The magnified window is used to demonstrate the automatic detected HFO event more precisely.

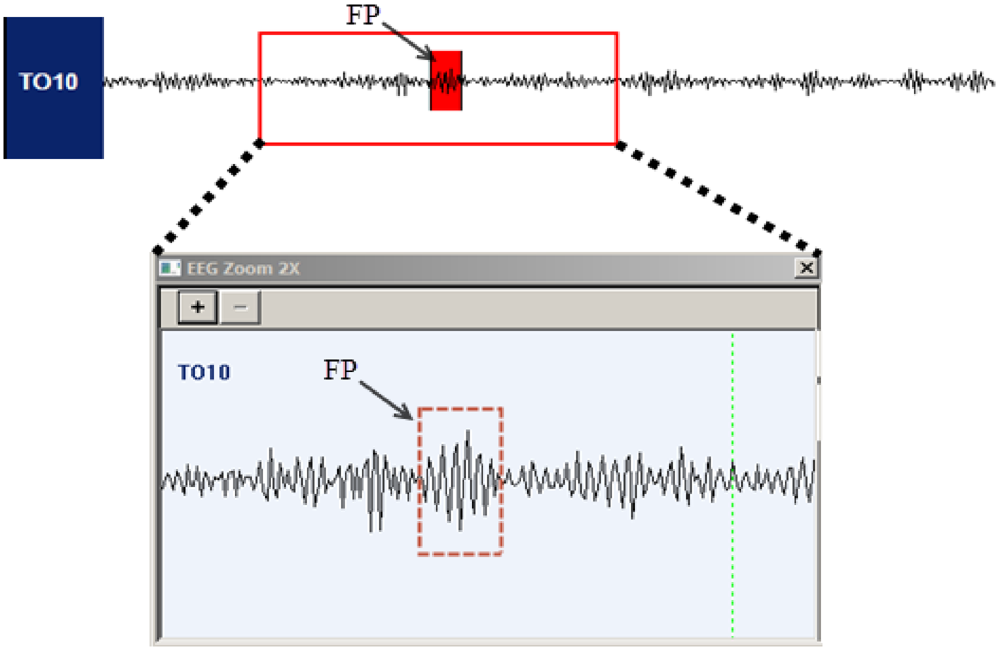

Figure 5.14 an example of False Positive event detected in patient II1. Magnifier was used to zoom and show the changes of the signal in the red box more precisely.

As can be seen, high frequency rhythmic activities are present across the segment in the figure. Generally, the presence of prolonged high frequency rhythmic activities in IEEG signal is not usual and may be an indication of the contamination by power line harmonics. Reviewing all events and omitting FP detections of all recording sites is far beyond the scope of this thesis, but can be considered as part of future work.

Second reason for having a high rate of FRs activity in the normal tissue especially in Sub-Frontal regions may be due to the type of the seizure. As stated earlier, in neocortical epileptic patients, the epilepsy is not well localized; hence, the seizure generating areas are not always defined clearly. Therefore, it is plausible that these tissues (Sub-Frontal) were capable of generating seizures but routine clinical assessments failed to detect them. If this proves to be accurate, then HFO (especially in the FR range) can be considered as a more robust assessment tool to be used for finding seizure generating tissues.

In this patient, the tissue under electrodes PT1-16, TO5-8, TO13-16, FP11-13, FP19-22, and FP27-30 have been resected by the surgeon. However, the normal tissue located in the sub-frontal region with a high rate of fast ripple activity remained intact. The post-surgery follow-up reported that this patient still suffers from epilepsy. Further analysis is required to verify whether sub-frontal tissue with a high rate of HFO activity is in correlation with the seizure or not.

Overall, based on the results obtained from the four patients, it seems that HFOs in the range of ripples and fast ripples can be identified in the epileptic patients with temporal lobe and neocortical epilepsy, using subdural and depth electrodes. Nevertheless, as expected, depth electrodes showed the highest rate of HFO activity, especially in the deepest contacts.

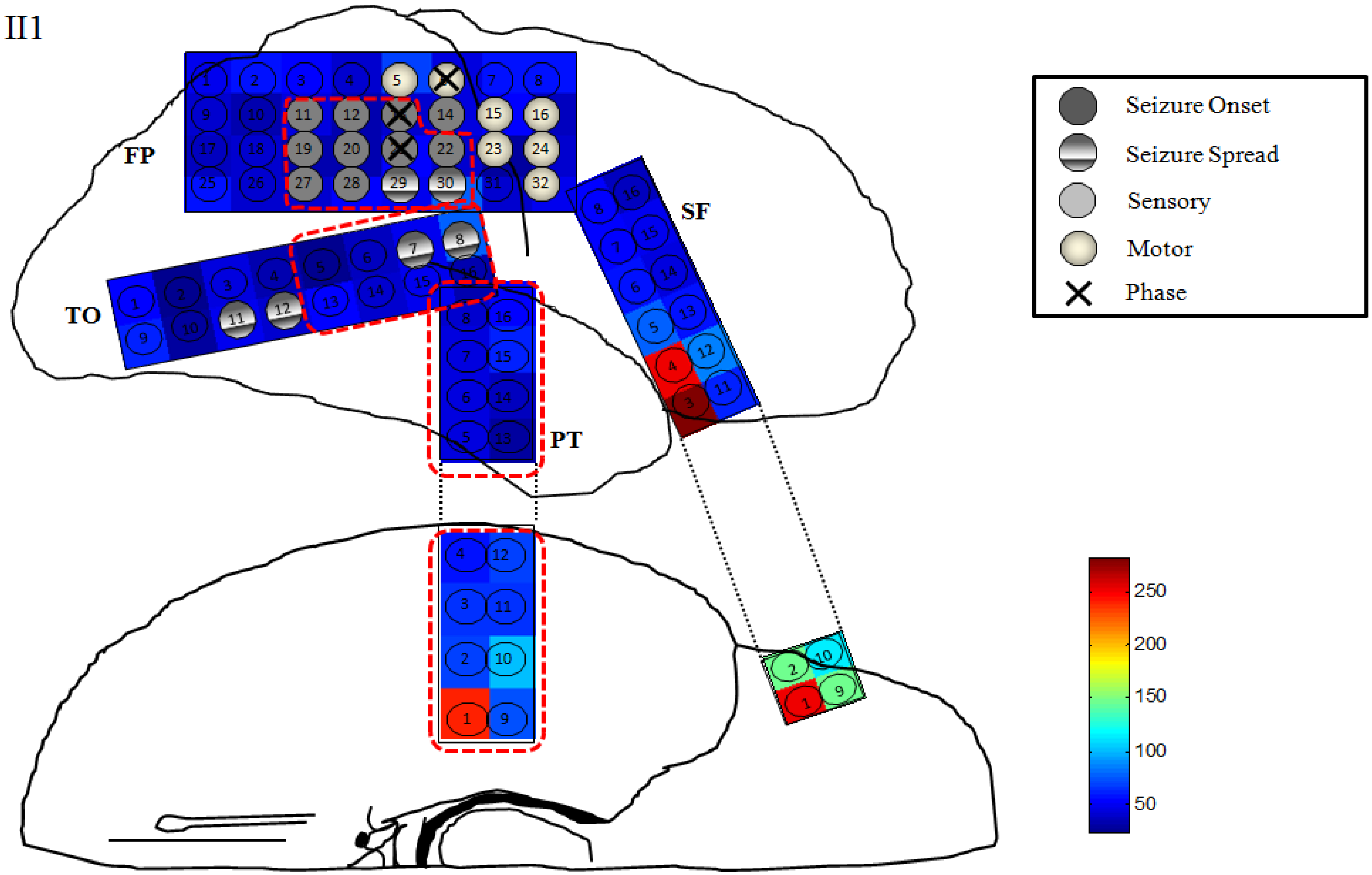

Figure 5.15 Topographic distribution of spontaneous ripples recorded at the electrodes positions for patient II1. The color bar indicates the number of detected ripples. Dashed red box indicates the resected area by surgeons. **Electrodes abbreviations**: TO= Temporal Occipital, PT= Posterior Temporal, FP = Frontal/Parietal, SF = Sub Frontal

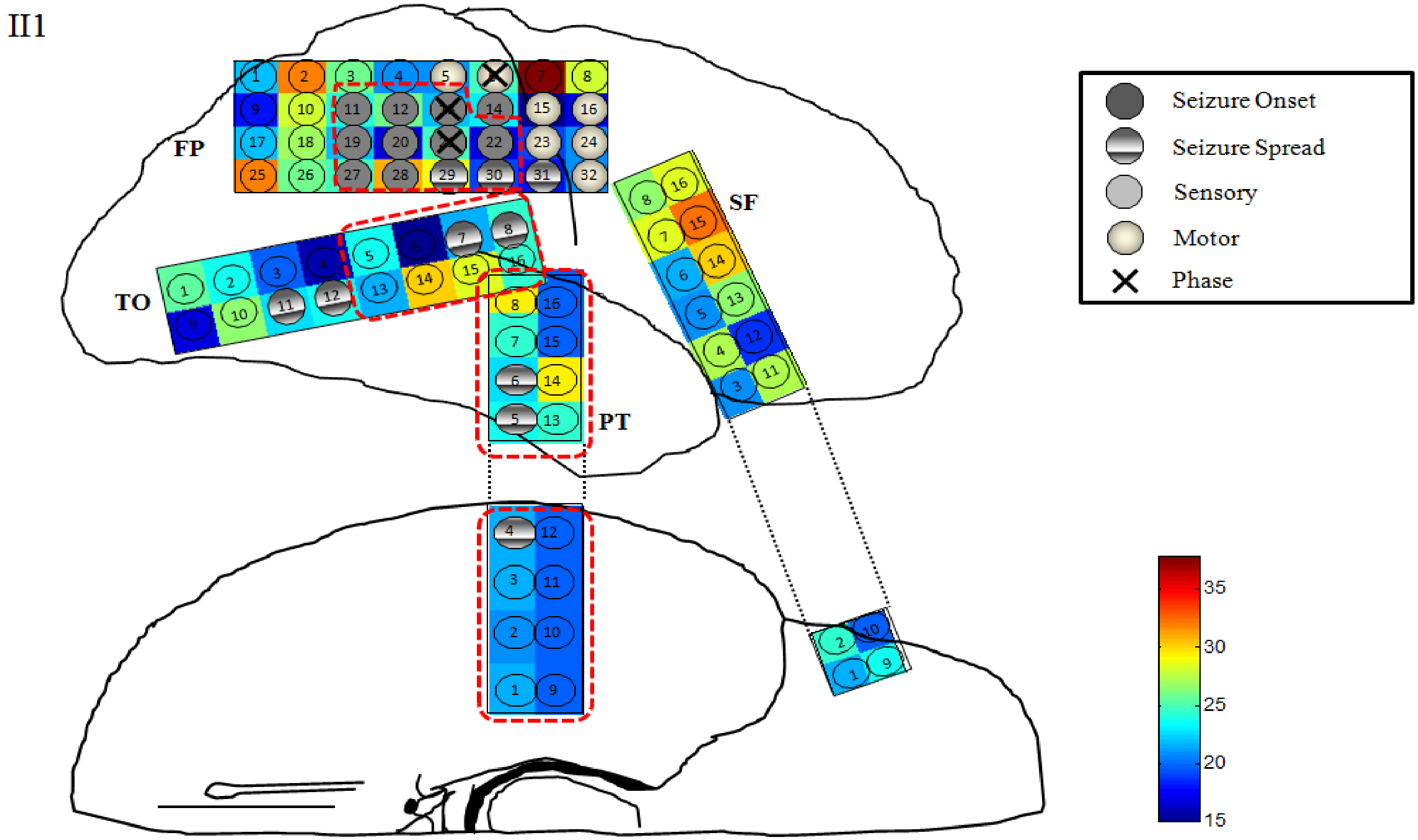

Figure 5.16 Topographic distribution of spontaneous fast ripples recorded at the electrodes positions for patient II1. The color bar indicates the number of detected fast ripple. The color bar indicates the color map for the detected events. Dashed red box indicates the resected area by surgeons. **Electrodes abbreviations**: TO= Temporal Occipital, PT= Posterior Temporal, FP = Frontal/Parietal, SF = Sub Frontal

In patient BB1 with unilateral temporal lobe epilepsy (right side), high rate of ripples were observed in the posterior temporal and somatosensory cortical structures. Results of this patient showed a very good correlation between the rate of occurrence of fast ripples and SOZ. A very good correlation of the rate of HFO activity in both sides of temporal lobe structures of patient CC2 supported the idea that this patient suffers from bilateral seizures.

Patient FF2 reported a high rate of ripples and fast ripples in almost all the recording sites (temporal lobe structures); however, the highest activities were seen in the SOZ and depth electrodes.

In contrast to the above patients, the rate of HFO occurrence in patient II1 with neocortical epilepsy did not correlate well with SOZ or SSZ. High rate of ripples and fast ripples were observed in the sub-frontal structure of the brain located on the normal tissue. As stated earlier, the reason might be due to the type of seizure or noise contamination such as power line harmonics.

In a nutshell, the assessment based on the HFO analysis appears to be consistent with the conclusion obtained with the routine practice (EEG, MRI, etc.). Consistent with the previous studies, our findings showed that ripples are spatially distributed in normal and pathological tissue of the epileptic patients, whereas the generation of fast ripples appear to be more localized than ripples and their rate of occurrence is more prominent at seizure generating tissues than normal tissue [36, 82-84] . In all patients, we observed a high rate of ripple activity in the lateral occipital recording sites located in the normal tissue, which is consistent with a recent study [85]. Moreover, this finding is in keeping with the previous studies in the sense that fast ripples may indeed be considered as biomarkers for epilepsy.

We have provided some anecdotal results of the correlation between HFO and epilepsy. Much work is still required to establish this in a scientific manner.

5.4 Summary

In the first section of this chapter, we subjected all the HFO detectors, described in Chapter 3, to real signals relating to 4 epileptic patients (24). The main goal was to evaluate the performance of the HFO detectors using real signals. Results showed that the RMS detector is highly dependent on the type of the signal and any high energy transient artifact affected the performance of this detector in a significant manner. On the other hand, the remaining energy-based detectors MS1, MS2, and STLL performed very well in terms of sensitivity; however, at the price of extremely low specificity. In contrast, the proposed sharpness-based detectors, *Slope*, *Iterative-Slope*, and *Slope-Causal*, were not sensitive to the artifacts, noise, or any high-energy transient interferences, and exhibited good performance in terms of both sensitivity and specificity.

In the final section, we subjected the Iterative-Slope detector to all the channels of four patients (a total of 286 channels) to evaluate the relationship between the rate of occurrence of HFO events and seizure generating tissues. The results showed that there is a good correlation between seizure generating tissues and rate of HFOs occurrence. This is consistent with the previous studies.

Chapter 6 . Conclusion and Suggestions for Future work

6.1 Conclusion

About thirty to forty percent of epileptic patients have medically intractable epilepsy and they continue to experience seizures even with the best available antiepileptic drugs. For these patients, surgical removal of epileptic brain tissue, when possible, is the most effective treatment. However, results obtained from surgery depend highly on the accurate identification of epileptic brain tissue and benefits of this treatment apply only to patients in whom seizures can be well localized in areas not responsible for critical functions.

EEG is one of the most common clinical diagnostic tests used to localize seizure-generating tissue in brain. Traditionally, to clinically analyze brain disorders, epileptologists were limited to EEG signals within the frequency range of 0.1-70 Hz. Advances in digital EEG recording techniques with higher sampling rate (≥ 1000 Hz) for invasive (IEEG) methods have allowed the identification of sporadic high frequency oscillations (HFOs) in the range of 100-500 Hz.

HFOs are mainly classified into two groups: ripples (100-250 Hz) and fast ripples (250-500 Hz). Researchers have experimentally demonstrated that HFOs mostly occur in tissue capable of generating spontaneous seizures. A strong correlation between resection of brain regions containing HFOs (especially in the fast ripples range) and positive post-surgical outcomes supports the idea that HFOs may be reliable biomarkers of epilepsy. HFOs can be identified visually; however, manually reviewing such short-duration events is a tedious process and subject to human interpretation. Development of automatic HFO detectors for objective and accurate identification of these events is extremely useful and crucial, particularly when long-term recording is considered.

In this thesis, three new HFO detection systems, namely, *Slope*, *Iterative-Slope*, and *Slope-Causal* have been proposed. These methods mainly focus on the "sharpness" feature of IEEG signals. In addition, two energy-based methods in the literature referred to as RMS [26] and STLL [55] were implemented. Moreover, in order to improve the performance of the existing RMS detector, two modified versions of this detector termed as the MS1 and MS2 have also been developed.

The performance of the above methods was tested on simulated signals as well as real-data signals of four epileptic patients. For the simulated signals, the sharpness-based detectors reported perfect performance (100% for both the sensitivity and specificity) and outperformed energy-based detectors. However, for the real data, this improvement was only observed in the specificity but not in the sensitivity. The complexity of the real data and inconsistency in the visual scored events (*Gold-Standard*) might be the main reasons for this drop.

Overall, the results indicated that the RMS detector heavily depended on the type of the signal and its performance easily deteriorated in the presence of artifacts, noise and any kind of high energy interferences. On the other hand, MS1, MS2, and STLL methods showed significant improvements in sensitivity; however, these detectors triggered often with any spurious fluctuation such as spikes and sharp-waves leading to poor specificity. In contrast to energy-based methods, the results obtained from the sharpness-based detectors depicted that the newly proposed sharpness-based detectors were relatively immune to transient changes in the signal and their performances did not deteriorate in the presence of noise or artifacts. The consistency of the results of the proposed sharpness-based detectors indicates that these detectors are robust and accurate regardless of the type of signals. Moreover, the energy-based algorithms generally failed to detect low energy rhythmic activities as HFO events; however, these types of events were successfully marked by the sharpness-based detectors.

With respect to computational complexity, the proposed MS1 and MS2 detectors require much fewer computations in identifying HFO events than the original RMS method [26]. Sharpness based detectors turned out to be yet even less complex than the MS1 and MS2 algorithms but they are more complex than the STLL detector [55].

Among the proposed systems, the performance of the Iterative-Slope detector was superior in both sensitivity and specificity. Consequently, this system was applied to all channels of the four patients (a total of 286 channels) in order to evaluate the spatial distribution of HFO events in each patient. In total, 13060 ripples and 5447 fast ripples were automatically detected on all of the channels. In patients with temporal lobe epilepsy (unilateral and bilateral) such as BB1, CC2, and FF2, HFO activities appeared to be more correlated with the SOZ, while this correlation was not that obvious in neocortical epileptic patient (II1). Generally, depth electrodes, particularly in the deepest contacts (corresponding to the hippocampal areas), showed higher rate of HFO activities compared to that in subdural electrodes, which is consistent with the previous studies.

Previous studies have shown that interictal HFOs (> 80 Hz) are also present in non-epileptic patients [36, 82-84] and the rate of occurrence of fast ripples in epileptic tissue is almost 3 times greater than that of normal tissue; however, this difference is not observed in the ripple range and its rate of occurrence is almost identical in epileptogenic and non-epileptogenic regions [84]. Consistent with these studies, our findings demonstrated that ripples were distributed in both normal and pathological tissue of epileptic patients, whereas fast ripples appeared to have a more restricted distribution and were localized in seizure-generating tissue. The viable correlation between seizure-generation zones and rate of HFO occurrences, specifically in fast ripple range, supports the idea that fast ripples may be considered as reliable biomarkers of epilepsy. On the other hand, our observations follow the recent study in the sense that spontaneous HFO events, especially in the ripple range, are present in the non-epileptogenic tissue corresponding to the occipital sites [85].

Based on the routine clinical assessments, some of the non-epileptic HFO generating tissues have been resected by surgeons, however, some remained intact. If the post-surgery follow-up proves that the patients still suffer from epilepsy, physician may consider HFO analysis to obtain additional information about seizure generating areas.

6.2 Future work

Following are some suggestions for the future work.

- Half-waves in the proposed methods were defined as the segments between two consecutive extrema of the IEEG signals in which the slope changes from one polarity to the opposite polarity regardless of their amplitudes. As stated earlier, the performance of the proposed detectors would deteriorate if low voltage sharp fluctuations are superimposed on the large amplitude activities such as spikes or sharp-waves. Developing an approach to define half-waves in a more robust way would increase the performance of this detector. One possible approach is to merge adjacent half-waves with slopes in the same directions of almost the same lengths when a small half-wave with opposite direction is located between them.

- Although the performance of the MS1 and MS2 detectors enhanced remarkably, the detection thresholds did not appear to be optimal. Future studies with larger dataset are required to define a more robust threshold in order to maintain a proper balance between sensitivity and specificity.
- The post-processing step such as peak counting may be applied to increase the performance of the energy-based detectors including MS1, MS2, and STLL.
- In the clinical aspect, more patients with exact clinical information (pre/post-surgery) are required for a proper evaluation of the clinical correlation between the automatic detected HFO events and seizure generating zones.
- HFO events need to be scored by multiple reviewers to develop a consensus scoring for a proper performance assessment.
- Evaluating false negatives (missed detections) as well as false positive detected events is required to discover as to how the performance of the proposed sharpness-based detectors can be improved.

Appendix

The calculation of the least square parameters in Equation 3.13

Consider a set of data given by:

$$y = \beta_0 + \beta_1 x + \epsilon \tag{1}$$

where y is the observed output, x is input, ϵ is a zero-mean additive noise sequence and β_0 and β_1 are model parameters. The objective is to estimate the parameters that provide the “best fit” to the data. The model prediction for the i^{th} data point is:

$$\hat{y}_i = \hat{\beta}_0 + \hat{\beta}_1 x_i \tag{2}$$

where $\hat{y}_i$ is the predicted output and $\hat{\beta}_0$, $\hat{\beta}_1$ are parameter estimations.

The error between the observed and predicted values can be written as

$$e_i = y_i - \hat{y}_i \tag{3}$$

A definition of “best-fit” is the parameter that minimizes the sum of the squared errors:

$$SSE = \sum_{i=1}^{n} (y_i - \hat{y}_i)^2 = \sum_{i=1}^{n} \left(y_i - \left(\hat{\beta}_0 - \hat{\beta}_1 x_i\right)\right)^2 \tag{4}$$

The minimum value of SSE happens when

$$\frac{\partial SSE}{\partial \widehat{\beta}_0} = 0 \quad \text{and} \quad \frac{\partial SSE}{\partial \widehat{\beta}_1} = 0 \tag{5}$$

Solving these equations give two equations that are known as least square equations.

$$-2\left(\sum_{i=1}^{n} y_i - n\hat{\beta}_0 + \hat{\beta}_1 \sum_{i=1}^{n} x_i\right) = 0 \tag{6}$$

$$-2\left(\sum_{i=1}^{n} x_i y_i - \hat{\beta}_0 \sum_{i=1}^{n} x_i + \hat{\beta}_1 \sum_{i=1}^{n} x_i^2\right) = 0 \tag{7}$$

By solving the least square equations, the parameters $\hat{\beta}_0$ and $\hat{\beta}_1$ are calculated by

$$\hat{\beta}_1 = \frac{\sum_{i=1}^{n}(x_i - E[x])(y_i - E[y])}{\sum_{i=1}^{n}(x_i - E[x])^2} \tag{8}$$

$$\hat{\beta}_0 = E[y] - \hat{\beta}_1 E[x] \tag{9}$$

References

[1] Jerome Engel,Jr.,M.D.,Ph.D., *Seizures and Epilepsy.* 1989.

[2] J. Jacobs, R. Staba, E. Asano, H. Otsubo, J. Wu, M. Zijlmans, I. Mohamed, P. Kahane, F. Dubeau, V. Navarro and J. Gotman, "High-frequency oscillations (HFOs) in clinical epilepsy," *Prog. Neurobiol.,* 2012.

[3] G. Buzsaki, Z. Horvath, R. Urioste, J. Hetke and K. Wise, "High-frequency network oscillation in the hippocampus," *Science,* vol. 256, pp. 1025, 1992.

[4] A. Bragin, C. L. Wilson, J. Almajano, I. Mody and J. Engel Jr, "High-frequency Oscillations after Status Epilepticus: Epileptogenesis and Seizure Genesis," *Epilepsia,* vol. 45, pp. 1017-1023, 2004.

[5] G. Worrell, "High-Frequency Oscillations Recorded on Scalp EEG," *Epilepsy Currents,* vol. 12, pp. 57, 2012.

[6] R. J. Staba, C. L. Wilson, A. Bragin, D. Jhung, I. Fried and J. Engel Jr, "High-frequency oscillations recorded in human medial temporal lobe during sleep," *Ann. Neurol.,* vol. 56, pp. 108-115, 2004.

[7] G. A. Worrell, L. Parish, S. D. Cranstoun, R. Jonas, G. Baltuch and B. Litt, "High-frequency oscillations and seizure generation in neocortical epilepsy," *Brain,* vol. 127, pp. 1496, 2004.

[8] J. Nolte PHD, *The Human Brain: An Introduction to its Function Anatomy 4th Ed.* 1998.

[9] R. d. Noback.Charles, *The Human Nervous System.* 1981.

[10] S. Sanei and J. A. Chambers, *EEG Signal Processing.* 2007.

[11] E. Niedermeyer and F. H. Lopes da Silva, *Electroencephalography: Basic Principles,Clinical Applications, and Related Fields.* 1999.

[12] R. Caton, "Interim report on investigation of the electric currents of the brain," *Br. Med. J.,* vol. 1, pp. 62, 1877.

[13] P. I. V. M. b. Yakovlev, "The founders of neurology,ed., W. haymaker," in Anonymous 1953, pp. 244-247-245-246-247.

[14] E. Niedermeyer, *The Epilepsies: Diagnosis and Management.* 1990.

[15] H. Berger, "Über das Elektrenkephalogramm des Menschen," *Eur. Arch. Psychiatry Clin. Neurosci.,* vol. 98, pp. 231-254, 1933.

[16] H. Berger, "Über das Elektrenkephalogramm des Menschen," *Eur. Arch. Psychiatry Clin. Neurosci.,* vol. 94, pp. 16-60, 1931.

[17] H. Berger, "Über das elektrenkephalogramm des menschen," *Eur. Arch. Psychiatry Clin. Neurosci.,* vol. 87, pp. 527-570, 1929.

[18] W. G. Walter, "Slow potential waves in the human brain associated with expectancy, attention and decision," *Eur. Arch. Psychiatry Clin. Neurosci.,* vol. 206, pp. 309-322, 1964.

[19] H. W. Shipton, "EEG analysis: A history and a prospectus," *Annu. Rev. Biophys. Bioeng.,* vol. 4, pp. 1-13, 1975.

[20] R. Cooper b., *EEG Technology 3rd Ed.* 1980.

[21] S. Lim, P. Pillay, H. Lüders and H. Boenigk, "Use of intracranial neurophysiology recording techniques in the evaluation for epilepsy surgery in children," *Singapore Med. J.,* vol. 33, pp. 131-138, 1992.

[22] H. Jasper, "Report of the committee on methods of clinical examination in electroencephalography." *Electroencephalogr. Clin. Neurophysiol.,* vol. 10, pp. 370-375, 1958.

[23] J. Jacobs, M. Zijlmans, R. Zelmann, C. É. Chatillon, J. Hall, A. Olivier, F. Dubeau and J. Gotman, "High-frequency electroencephalographic oscillations correlate with outcome of epilepsy surgery," *Ann. Neurol.,* vol. 67, pp. 209-220, 2010.

[24] J. Jirsch, E. Urrestarazu, P. LeVan, A. Olivier, F. Dubeau and J. Gotman, "High-frequency oscillations during human focal seizures," *Brain,* vol. 129, pp. 1593-1608, 2006.

[25] J. J. Chrobak and G. Buzsáki, "High-frequency oscillations in the output networks of the hippocampal–entorhinal axis of the freely behaving rat," *The Journal of Neuroscience,* vol. 16, pp. 3056-3066, 1996.

[26] R. J. Staba, C. L. Wilson, A. Bragin, I. Fried and J. Engel, "Quantitative analysis of high-frequency oscillations (80–500 Hz) recorded in human epileptic hippocampus and entorhinal cortex," *J. Neurophysiol.,* vol. 88, pp. 1743, 2002.

[27] A. Bragin, J. Engel Jr, C. L. Wilson, I. Fried and G. W. Mathern, "Hippocampal and entorhinal cortex high-frequency oscillations (100–500 Hz) in human epileptic brain and in kainic acid-treated rats with chronic seizures," *Epilepsia,* vol. 40, pp. 127-137, 1999.

[28] A. Bragin, J. Engel Jr, C. L. Wilson, I. Fried and G. Buzsáki, "High-frequency oscillations in human brain," *Hippocampus,* vol. 9, pp. 137-142, 1999.

[29] C. A. Schevon, A. Trevelyan, C. Schroeder, R. Goodman, G. McKhann Jr and R. Emerson, "Spatial characterization of interictal high frequency oscillations in epileptic neocortex," *Brain,* vol. 132, pp. 3047-3059, 2009.

[30] R. J. Staba, L. Frighetto, E. J. Behnke, G. W. Mathern, T. Fields, A. Bragin, J. Ogren, I. Fried, C. L. Wilson and J. Engel Jr, "Increased fast ripple to ripple ratios correlate with reduced hippocampal volumes and neuron loss in temporal lobe epilepsy patients," *Epilepsia,* vol. 48, pp. 2130-2138, 2007.

[31] T. Akiyama, H. Otsubo, A. Ochi, E. Z. Galicia, S. K. Weiss, E. J. Donner, J. T. Rutka and O. C. Snead III, "Topographic Movie of Ictal High-Frequency Oscillations on the Brain Surface Using Subdural EEG in Neocortical Epilepsy," *Epilepsia,* vol. 47, pp. 1953-1957, 2006.

[32] A. Ochi, H. Otsubo, E. J. Donner, I. Elliott, R. Iwata, T. Funaki, Y. Akizuki, T. Akiyama, K. Imai and J. T. Rutka, "Dynamic Changes of Ictal High-Frequency Oscillations in Neocortical Epilepsy: Using Multiple Band Frequency Analysis," *Epilepsia,* vol. 48, pp. 286-296, 2007.

[33] H. Imamura, R. Matsumoto, M. Inouchi, M. Matsuhashi, N. Mikuni, R. Takahashi and A. Ikeda, "Ictal wideband ECoG: Direct comparison between ictal slow shifts and high frequency oscillations," *Clinical Neurophysiology,* 2011.

[34] E. Urrestarazu, R. Chander, F. Dubeau and J. Gotman, "Interictal high-frequency oscillations (100–500 Hz) in the intracerebral EEG of epileptic patients," *Brain,* vol. 130, pp. 2354, 2007.

[35] E. Urrestarazu, J. D. Jirsch, P. LeVan and J. Hall, "High-Frequency Intracerebral EEG Activity (100–500 Hz) Following Interictal Spikes," *Epilepsia,* vol. 47, pp. 1465-1476, 2006.

[36] N. Axmacher, C. E. Elger and J. Fell, "Ripples in the medial temporal lobe are relevant for human memory consolidation," *Brain,* vol. 131, pp. 1806, 2008.

[37] J. Jacobs, P. LeVan, R. Chander, J. Hall, F. Dubeau and J. Gotman, "Interictal high-frequency oscillations (80–500 Hz) are an indicator of seizure onset areas independent of spikes in the human epileptic brain," *Epilepsia,* vol. 49, pp. 1893-1907, 2008.

[38] J. Jacobs, P. LeVan, C. É. Châtillon, A. Olivier, F. Dubeau and J. Gotman, "High frequency oscillations in intracranial EEGs mark epileptogenicity rather than lesion type," *Brain,* vol. 132, pp. 1022, 2009.

[39] J. Jacobs, M. Zijlmans, R. Zelmann, A. Olivier, J. Hall, J. Gotman and F. Dubeau, "Value of electrical stimulation and high frequency oscillations (80–500 Hz) in identifying epileptogenic areas during intracranial EEG recordings," *Epilepsia,* vol. 51, pp. 573-582, 2010.

[40] K. Kobayashi, J. Jacobs and J. Gotman, "Detection of changes of high-frequency activity by statistical time-frequency analysis in epileptic spikes," *Clinical Neurophysiology,* vol. 120, pp. 1070-1077, 2009.

[41] M. Zijlmans, J. Jacobs, R. Zelmann, F. Dubeau and J. Gotman, "High frequency oscillations and seizure frequency in patients with focal epilepsy," *Epilepsy Res.,* vol. 85, pp. 287-292, 2009.

[42] G. A. Worrell, A. B. Gardner, S. M. Stead, S. Hu, S. Goerss, G. J. Cascino, F. B. Meyer, R. Marsh and B. Litt, "High-frequency oscillations in human temporal lobe: simultaneous microwire and clinical macroelectrode recordings," *Brain,* vol. 131, pp. 928, 2008.

[43] P. N. Modur, S. Zhang and T. W. Vitaz, "Ictal High-Frequency Oscillations in Neocortical Epilepsy: Implications for Seizure Localization and Surgical Resection," *Epilepsia,* 2011.

[44] B. Crépon, V. Navarro, D. Hasboun, S. Clemenceau, J. Martinerie, M. Baulac, C. Adam and M. Le Van Quyen, "Mapping interictal oscillations greater than 200 Hz recorded with intracranial macroelectrodes in human epilepsy," *Brain,* vol. 133, pp. 33-45, 2010.

[45] H. Khosravani, N. Mehrotra, M. Rigby, W. J. Hader, C. R. Pinnegar, N. Pillay, S. Wiebe and P. Federico, "Spatial localization and time-dependant changes of electrographic high frequency oscillations in human temporal lobe epilepsy," *Epilepsia,* vol. 50, pp. 605-616, 2009.

[46] A. Bragin, G. Jandó, Z. Nádasdy, J. Hetke, K. Wise and G. Buzsaki, "Gamma (40-100 Hz) oscillation in the hippocampus of the behaving rat," *The Journal of Neuroscience,* vol. 15, pp. 47-60, 1995.

[47] T. Akiyama, B. McCoy, C. Y. Go, A. Ochi, I. M. Elliott, M. Akiyama, E. J. Donner, S. K. Weiss, O. C. Snead III and J. T. Rutka, "Focal resection of fast ripples on extraoperative intracranial EEG improves seizure outcome in pediatric epilepsy," *Epilepsia,* 2011.

[48] A. Ylinen, A. Bragin, Z. Nádasdy, G. Jandó, I. Szabo, A. Sik and G. Buzsaki, "Sharp

wave-associated high-frequency oscillation (200 Hz) in the intact hippocampus: network and intracellular mechanisms," *The Journal of Neuroscience,* vol. 15, pp. 30-46, 1995.

[49] A. A. Ponomarenko, T. M. Korotkova and H. L. Haas, "High frequency (200 Hz) oscillations and firing patterns in the basolateral amygdala and dorsal endopiriform nucleus of the behaving rat," *Behav. Brain Res.,* vol. 141, pp. 123-129, 2003.

[50] W. E. Skaggs, B. L. McNaughton, M. Permenter, M. Archibeque, J. Vogt, D. G. Amaral and C. A. Barnes, "EEG sharp waves and sparse ensemble unit activity in the macaque hippocampus," *J. Neurophysiol.,* vol. 98, pp. 898-910, 2007.

[51] A. Bragin, I. Mody, C. L. Wilson and J. Engel, "Local generation of fast ripples in epileptic brain," *The Journal of Neuroscience,* vol. 22, pp. 2012, 2002.

[52] G. Buzsaki, *Rhythms of the Brain.* Oxford University Press, 2006.

[53] J. Engel Jr, A. Bragin, R. Staba and I. Mody, "High-frequency oscillations: What is normal and what is not?" *Epilepsia,* vol. 50, pp. 598-604, 2009.

[54] D. S. Barth, "Submillisecond synchronization of fast electrical oscillations in neocortex," *The Journal of Neuroscience,* vol. 23, pp. 2502, 2003.

[55] A. B. Gardner, G. A. Worrell, E. Marsh, D. Dlugos and B. Litt, "Human and automated detection of high-frequency oscillations in clinical intracranial EEG recordings," *Clinical Neurophysiology,* vol. 118, pp. 1134-1143, 2007.

[56] R. D. Traub, M. A. Whittington, E. H. Buhl, F. E. N. LeBeau, A. Bibbig, S. Boyd, H. Cross and T. Baldeweg, "A possible role for gap junctions in generation of very fast EEG oscillations preceding the onset of, and perhaps initiating, seizures," *Epilepsia,* vol. 42, pp. 153-170, 2001.

[57] R. Köhling and K. Staley, "Network mechanisms for fast ripple activity in epileptic tissue," *Epilepsy Res.,* 2011.

[58] O. Smart, G. Worrell, G. Vachtsevanos and B. Litt, "Automatic detection of high frequency epileptiform oscillations from intracranial EEG recordings of patients with neocortical epilepsy," in *Technical, Professional and Student Development Workshop, 2005 IEEE Region 5 and IEEE Denver Section,* 2005, pp. 53-58.

[59] R. Chander. An algorithm to detect HFO. 2007.

[60] H. Firpi, O. Smart, G. Worrell, E. Marsh, D. Dlugos and B. Litt, "High-frequency oscillations detected in epileptic networks using swarmed neural-network features," *Ann. Biomed. Eng.,* vol. 35, pp. 1573-1584, 2007.

[61] R. Zelmann, F. Mari, J. Jacobs, M. Zijlmans, R. Chander and J. Gotman, "Automatic

detector of high frequency oscillations for human recordings with macroelectrodes," in *Engineering in Medicine and Biology Society (EMBC), 2010 Annual International Conference of the IEEE,* 2010, pp. 2329-2333.

[62] K. Kobayashi, H. Yoshinaga, Y. Toda, T. Inoue, M. Oka and Y. Ohtsuka, "High-frequency oscillations in idiopathic partial epilepsy of childhood," *Epilepsia,* 2011.

[63] A. S. Blum and S. B. Rutkove, *The Clinical Neurophysiology Primer.* Springer, 2006.

[64] N. Usui, K. Terada, K. Baba, K. Matsuda, F. Nakamura, K. Usui, T. Tottori, S. Umeoka, S. Fujitani and T. Mihara, "Very high frequency oscillations (over 1000 Hz) in human epilepsy," *Clinical Neurophysiology,* vol. 121, pp. 1825-1831, 2010.

[65] I. Khalilov, M. Le Van Quyen, H. Gozlan and Y. Ben-Ari, "Epileptogenic actions of GABA and fast oscillations in the developing hippocampus," *Neuron,* vol. 48, pp. 787-796, 2005.

[66] R. Zelmann, M. Zijlmans, J. Jacobs, C. E. Châtillon and J. Gotman, "Improving the identification of high frequency oscillations," *Clinical Neurophysiology,* vol. 120, pp. 1457-1464, 2009.

[67] M. Brázdil, J. Halámek, P. Jurák, P. Daniel, R. Kuba, J. Chrastina, Z. Novák and I. Rektor, "Interictal high-frequency oscillations indicate seizure onset zone in patients with focal cortical dysplasia," *Epilepsy Res.,* vol. 90, pp. 28-32, 2010.

[68] M. Fatourechi, A. Bashashati, R. K. Ward and G. E. Birch, "EMG and EOG artifacts in brain computer interface systems: A survey," *Clinical Neurophysiology,* vol. 118, pp. 480-494, 2007.

[69] Y. Xiao, Y. Takeshita and K. Shida, "Steady-state analysis of a plain gradient algorithm for a second-order adaptive IIR notch filter with constrained poles and zeros," *Circuits and Systems II: Analog and Digital Signal Processing, IEEE Transactions on,* vol. 48, pp. 733-740, 2001.

[70] J. Zhou and G. Li, "Plain gradient based direct frequency estimation using second-order constrained adaptive IIR notch filter," *Electron. Lett.,* vol. 40, pp. 351-352, 2004.

[71] J. R. Smith, "Automatic analysis and detection of EEG spikes. IEEE Trans.Biomed.Engng.," vol. 21, pp. 1-7, 1974.

[72] J. Gotman and P. Gloor, "Automatic recognition and quantification of interictal epileptic activity in the human scalp EEG," *Electroencephalogr. Clin. Neurophysiol.,* vol. 41, pp. 513-529, 1976.

[73] B. Saltzberg, R. Heath and R. Edwards, "EEG spike detection in schizophrenia

research," in *Dig. 7th Int. Conf. Medical and Biological Engineering,* 1967, pp. 1967.

[74] B. Saltzberg, L. S. Lustick and R. G. Heath, "Detection of focal depth spiking in the scalp EEG of monkeys," *Electroencephalogr. Clin. Neurophysiol.,* vol. 31, pp. 327-333, 1971.

[75] A. Hill and H. Townsend, "The automatic estimation of epileptic spike activity," *Int. J. Biomed. Comput.,* vol. 4, pp. 149-156, 1973.

[76] P. B. Fenwick, P. Mitchie, J. Dollimore and G. W. Fenton, "Application of the autoregressive model to E.E.G. analysis," *Agressologie,* vol. 10, pp. Suppl:553-64, Jun 16, 1969.

[77] L. H. Zetterberg, "Estimation of parameters for a linear difference equation with application to EEG analysis," *Math. Biosci.,* vol. 5, pp. 227-275, 1969.

[78] F. Vaz, P. G. de Oliveira and J. C. Principe, "A study on the best order for autoregressive EEG modelling," *Int. J. Biomed. Comput.,* vol. 20, pp. 41-50, 1987.

[79] L. Shi, Concordia University and Concordia University, *Model-Based Seizure Detection Method using Statistically Optimal Null Filters.* 2005.

[80] R. B. Blackman, J. W. Tukey, J. W. Tukey and J. W. Tukey, *The Measurement of Power Spectra: From the Point of View of Communications Engineering.* Dover Publications New York, 1959.

[81] S. Wang, I. Z. Wang, J. C. Bulacio, J. C. Mosher, J. Gonzalez-Martinez, A. V. Alexopoulos, I. M. Najm and N. K. So, "Ripple classification helps to localize the seizure-onset zone in neocortical epilepsy," *Epilepsia,* 2012.

[82] R. Csercsa, B. Dombovári, D. Fabó, L. Wittner, L. Erőss, L. Entz, A. Sólyom, G. Rásonyi, A. Szűcs and A. Kelemen, "Laminar analysis of slow wave activity in humans," *Brain,* vol. 133, pp. 2814-2829, 2010.

[83] M. Le Van Quyen, R. Staba, A. Bragin, C. Dickson, M. Valderrama, I. Fried and J. Engel, "Large-scale microelectrode recordings of high-frequency gamma oscillations in human cortex during sleep," *The Journal of Neuroscience,* vol. 30, pp. 7770-7782, 2010.

[84] J. A. Ogren, C. L. Wilson, A. Bragin, J. J. Lin, N. Salamon, R. A. Dutton, E. Luders, T. A. Fields, I. Fried and A. W. Toga, "Three-dimensional surface maps link local atrophy and fast ripples in human epileptic hippocampus," *Ann. Neurol.,* vol. 66, pp. 783-791, 2009.

[85] T. Nagasawa, C. Juhász, R. Rothermel, K. Hoechstetter, S. Sood and E. Asano, "Spontaneous and visually driven high-frequency oscillations in the occipital cortex: Intracranial recording in epileptic patients," *Hum. Brain Mapp.,* vol. 33, pp. 569-583,

2012.